Copies

AFWL-TR-68-13

Theoretical Notes
Note 118

AFWL-TR-
68-13

ENERGY DEPOSITION RATES AND RADIAL AND POLAR COMPTON CURRENTS FROM GAMMA-RAY AND NEUTRON SOURCES IN THE INTERMEDIATE ALTITUDE RANGE

M. O. Cohen
R. D. Schamberger

United Nuclear Corporation
Elmsford, New York

Contract F29601-67-C-0048

TECHNICAL REPORT NO. AFWL-TR-68-13

AIR FORCE WEAPONS LABORATORY
Air Force Systems Command
Kirtland Air Force Base
New Mexico

June 1968

ABSTRACT

The investigation reported herein was undertaken to determine primary and secondary gamma-ray energy deposition rates, and radial and polar Compton electron currents from specified monoenergetic neutron and gamma-ray sources at specific altitudes in the intermediate altitude range. The magnitude and time dependence of the gamma-ray energy deposition and Compton electron currents were determined, by Monte Carlo studies, at point detector locations surrounding each source position. The results at each detector location were analyzed to provide a general description of energy deposition and Compton currents from the considered sources. Energy deposition rates and radial currents from primary photon sources are fit to a two-exponential analytical expression. The variation of polar currents, from primary photon sources, with source altitude and energy and source-to-detector orientation and separation distance, is described. Also described are the energy deposition rates and radial and polar currents from secondary sources of gamma radiation. A detailed description is presented of a series of additional calculations, which, on the basis of the data obtained in this program, are recommended to supplement this study.

This page intentionally left blank.

CONTENTS

ILLUSTRATIONS

TABLES

This page intentionally left blank.

SECTION I

INTRODUCTION

The investigation reported herein has been undertaken to determine primary and secondary gamma-ray energy deposition rates, and radial and polar Compton electron currents from specified monoenergetic neutron and gamma-ray sources at specific altitudes in the intermediate altitude range.*

In this study, the primary photon sources considered were point isotropic 500-kev sources at 15,000 and 50,000 ft and a 5-Mev source at 15,000 ft. The primary neutron sources were point isotropic 14, 10, 7, and 5-Mev sources at 15,000 ft and a 14-Mev source at 50,000 ft. The secondary gamma rays considered were those generated by neutron interactions at energies above the inelastic scattering threshold in nitrogen.

The magnitude and time dependence of the resulting gamma-ray energy deposition and radial and polar Compton electron currents were determined, by Monte Carlo studies, at point detector locations surrounding each source position. The results at each detector location were analyzed to provide a general description of energy deposition and Compton currents from the considered sources.

*The intermediate altitude range is defined as the span of source elevations above ground for which both air-ground effects and radiation leakage from the top of the atmosphere are negligible.

In this report, energy deposition rates and radial currents from primary photon sources are fit to a two-exponential analytical expression. The variation of polar currents, from primary photon sources, with source altitude and energy and source-to-detector orientation and separation distance, is described. Also described are the energy deposition rates and radial and polar currents from secondary sources of gamma radiation.

In the final section of the report a description is given of a series of additional calculations, which, on the basis of the data obtained in this program, are recommended to supplement this study.

SECTION II

CALCULATIONAL METHODS

All neutron and gamma-ray calculations were performed with the United Nuclear CORSAIR code,* a FORTRAN Monte Carlo system. For the primary neutron problems, sources of secondary gamma radiation were generated from the neutron transport problems.

Time-dependent gamma-ray doses and fluxes were determined at specified point detector locations. Subsequently, the United Nuclear CORREDIT computer program was utilized to calculate the electron currents generated by gamma-ray Compton scattering in the atmosphere.

SPATIAL COORDINATE SYSTEM

Fig. 1 shows the basic source-detector geometry used in the Monte Carlo calculations.

A point isotropic source is located in a Cartesian coordinate system at 0, 0, Z_S, where Z_S is the source altitude, and a detector is located in Cartesian coordinates at X_d, Y_d, Z_d. The X and Y axes define a plane parallel to the ground. The atmospheric density varies only with altitude and thus the radiation transport exhibits axial symmetry about the Z-axis.

*CORSAIR is a direct descendent of the basic United Nuclear air transport system, AIRTRANS.[1] The only major difference in the two systems is that CORSAIR tracks correlated mirror histories as described in Section 2.2.

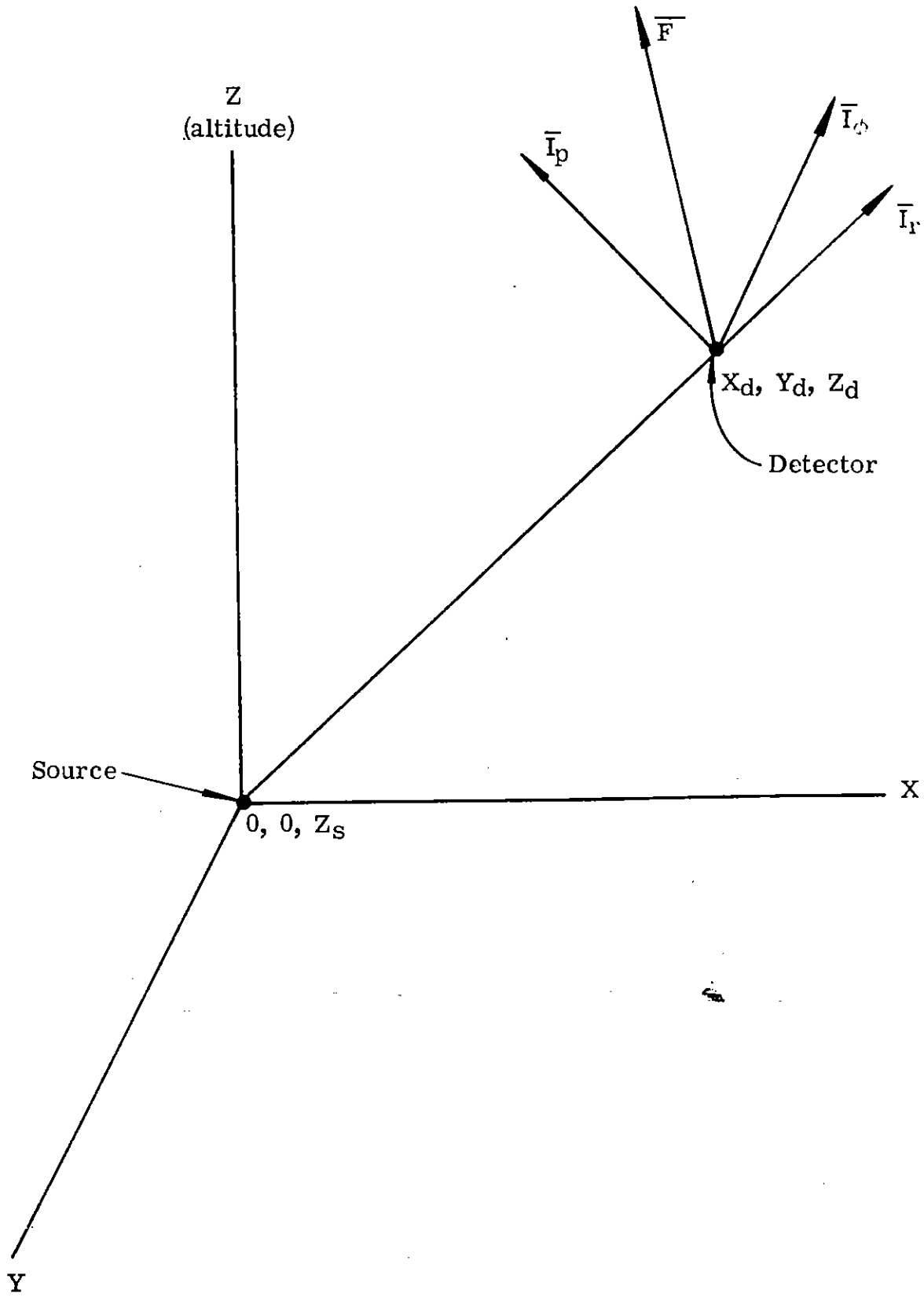

Fig. 1 — Basic Source-Detector Geometry Used in the Monte Carlo Calculations

Consider a vector score, $\bar{F}$, at the detector position. This score can be characterized by its projections along the Cartesian X, Y, and Z axes. This is not the most convenient coordinate system, however. A more convenient coordinate system is defined by three mutually orthogonal vectors $\bar{I}_r$, $\bar{I}_p$, and $\bar{I}_\phi$ where: $\bar{I}_r$ = the radial vector which is colinear to the source-detector axis; $\bar{I}_p$ = the polar vector, where $\bar{I}_r$ and $\bar{I}_p$ define a plane perpendicular to the ground; and $\bar{I}_\phi$ = the azimuthal vector, which is parallel to the ground.

It is apparent that in an atmosphere which varies only with height, the algebraic sum of all scores projected onto the azimuthal vector must vanish. (Hence, in the Monte Carlo calculations, computer time was not spent projecting individual scores along this vector.)

Variations of the transport medium with altitude, however, do produce net scores along the polar axis, which would otherwise vanish in a completely homogeneous medium. (Because of the symmetry of the geometry about the Z axis, the net polar scores do vanish at detector locations directly above or below a point isotropic source.)

THE INTERMEDIATE ALTITUDE AND CORRELATED PARTICLE HISTORIES

In the intermediate altitude range (15,000 to 50,000 ft) of this study, the escape of particles from the atmosphere and air-ground effects may be ignored. Hence, polar Compton currents in this intermediate range are produced entirely by the density variation of the atmosphere. The density variations involved are not drastic and thus polar currents are small compared to the radial currents.

Studies with the United Nuclear Monte Carlo air transport code AIRTRANS[1] have shown that, if usual Monte Carlo particle tracking techniques are used for sources in the intermediate altitude range, polar currents are calculated with absolute variances about equal to the absolute variances associated with the

radial currents despite the fact that the polar currents are often two or three orders of magnitude smaller than the radial currents. Clearly, then, inordinately large amounts of computer time would be required to determine, with reasonable statistical accuracy, polar currents for the intermediate altitude range.

Hence United Nuclear developed a correlated sampling technique especially designed to improve the computation of the small polar currents.

In this correlated sampling technique, a particle and its geometric "mirror" image about the source-detector (radial) axis are tracked simultaneously from collision to collision. The "weight" of the mirror history is altered at each collision point in a manner appropriate to the forced change in transport necessary to maintain the geometric symmetry. This involves a multiplication of the mirror weight by an $e^{-\Delta\lambda}$ term to account for the difference in mean free paths which the mirror history was forced to fly, and by a ρ(mirror)/ρ(real) term to account for the altered density and therefore the altered probability of collision for the mirror history.

The adjusted weight of a mirror particle at any point in its history is the cumulative product of all the weight alterations to that point.

Each time a score is made at a detector, contributions from both the real particle and the weighted mirror particle are estimated, added vectorially, and projected upon the radial and polar axes. With this technique, the net correlated polar component of the current is estimated directly every time a score is made and the fractional variances of the polar currents are reduced to the same order of magnitude as the fractional variances of the radial currents.

Additional discussion of the correlated tracking technique is presented as Appendix A.

COMPUTER CODES

The CORSAIR System

CORSAIR is a system of FORTRAN Monte Carlo codes used to track correlated (mirror) neutrons or gamma rays in the variable density atmosphere. An option also exists to generate secondary gamma rays from neutron inelastic scattering, (n,p) and (n,α) events.

In CORSAIR, time- and energy-dependent fluxes are calculated at point-detector locations in the atmosphere. The time and energy bins are specified by the user. Uncollided fluxes are estimated analytically at each detector, whereas collided fluxes are estimated by the once-more-collided flux-at-a-point[2,3] or flux-at-a-ring[4,5,6] techniques.

The CORSAIR system uses an analytic importance sampling technique for deep penetration problems which is designed to keep nearly constant the number of particles passing any surface of constant penetration (in mean free paths). The importance sampling process can be terminated beyond a given penetration, specified by the user.

Energy-dependent response functions are applied to the gamma-ray fluxes to obtain energy deposition in air in units of rads. These response functions are taken from Reference 7.

Parameters describing individual correlated flux estimates are written on output magnetic tape. Subsequently, the CORREDIT routine (see below) is utilized to convert gamma-ray fluxes to Compton currents and to obtain the components of the currents along the radial and polar axes.

The CORREDIT Routine

Program CORREDIT reads in the individual correlated flux estimates

written on output magnetic tape by CORSAIR. Included with each flux estimate are parameters describing the detector position and the energy, direction cosines, and time of arrival of the incoming gamma rays. CORREDIT utilizes this information and the well-known Klein-Nishina formula to generate, by Monte Carlo methods, the energy, direction cosines, and magnitude (weight) of the generated Compton electron. The crow-flight distance traveled by this electron is then calculated from tables of the range of electrons in air vs electron energy (see Appendix B), and this computed distance is resolved about the radial and polar axes to give an estimate of the radial and polar currents.

(In the CORREDIT calculations it is assumed that the time of flight of electrons is negligible compared to the times of flight of the gamma rays and also that all Compton currents may be localized to the detector location where the electrons were born. Another assumption is that electron transport in the nonuniform medium has negligible effect upon the polar currents.)

CORREDIT converts each flux estimate from CORSAIR to a radial and polar Compton current estimate and stores this information in the proper detector-energy-time-bin. When all flux estimates have been converted to currents and these currents have been resolved and stored in their proper bins, CORREDIT algebraically sums the individual current estimates and applies a statistical analysis to the results to evaluate the variance for each answer.

The output of CORREDIT is then energy- and time-dependent radial and polar Compton currents at each detector location.

SECTION III

PROBLEM DESCRIPTION

PRIMARY RADIATION SOURCES

All primary radiation is assumed to be emitted instantaneously from point isotropic sources. These are described in Tables I and II.

TABLE I — PRIMARY GAMMA RADIATION

Energy	Altitude, ft
500 kev	15,000
500 kev	50,000
5 Mev	15,000

TABLE II — PRIMARY NEUTRON RADIATION

Energy, Mev	Altitude, ft
14	15,000
10	15,000
7	15,000
5	15,000
14	50,000

All calculational results are on a per unit primary radiation particle basis.

THE ATMOSPHERE

The density of the atmosphere as used in all transport calculations is a continuously varying function of altitude. (A table of air density vs altitude,

which was derived from Reference 8 and used in these calculations, is presented as Appendix C.) The atomic constituents considered in gamma-ray transport calculations are nitrogen, oxygen, and argon with atomic fractions of 0.784756, 0.210551, and 0.004693, respectively. Argon was not included in the composition of the atmosphere in the neutron calculations, as studies at United Nuclear have shown that its effect upon the neutron transport is negligible.

The atomic compositions used in the neutron and gamma-ray calculations are assumed constant from ground level up to an altitude of 460 km; the latter is taken as the upper limit of the atmosphere.

CROSS SECTIONS

The microscopic cross-section data were supplied to the CORSAIR system by element data tapes in use at United Nuclear Corporation. The energy range for neutrons is 3.841 to 14 Mev, since neutrons were not tracked below the inelastic scattering threshold of nitrogen. The neutron cross sections, listed in Appendix D, are specified at 300 equally spaced (in lethargy units) mesh points. The gamma-ray energy range is 1 kev to 10 Mev, with cross sections specified at 99 equally spaced lethargy intervals. The gamma-ray data are derived from References 9 and 10.

The probability tables for the generation of secondary gamma rays from neutron charged particle and inelastic scattering events are given in Appendix E.

Energy-dependent response functions, used to convert gamma-ray fluxes to air dose in rads, were derived from Reference 7.

OTHER INPUT DATA

The cutoff times for both the neutron and gamma-ray problems were long enough so that none of the histories followed was terminated by exceeding the time limit.

The cutoff energy for the neutron problems was 3.84 Mev, a value just below the inelastic scattering threshold for nitrogen. The cutoff energies for the gamma-ray problems were functions of the particular transport problem under consideration. In all cases, however, the photon cutoff energy was low enough so that less than 2% of the total dose was estimated to have been lost.

DESCRIPTION OF CALCULATIONS

A summary description of all the CORSAIR problems which were run for this report is given in Appendix F.

SECTION IV

RESULTS OF PRIMARY GAMMA RADIATION STUDIES

ENERGY DEPOSITION

The desire to obtain a relatively simple analytical description of the spatial and temporal distribution of the energy deposition about a point isotropic photon source has led to an examination of the applicability of homogeneous atmosphere scaling to the inhomogeneous atmosphere situation. In the homogeneous case, the total energy deposition per gram of air at a distance R from the source in air of density ρ, $D(\rho R)$, can be expressed in terms of the energy deposition at a distance R_0 in an atmosphere of density ρ_0 as:

$$D(\rho R) = D(\rho_0 R_0) \cdot \frac{R_0^2}{R^2} \tag{1a}$$

where $\rho R = \rho_0 R_0$.

Similarly, for the energy deposition per reduced time interval:

$$d_{\rho R}(t_r) = d_{\rho_0 R_0}(t_r) \cdot \frac{R_0^2}{R^2} \tag{1b}$$

where $\rho R = \rho_0 R_0$

$t_r \equiv$ reduced time

$\equiv (t - t_u)/t_u$, and

t = real time

t_u = uncollided flight time = R/c.

As discussed below, the data generated in this program are consistent with the assumption that these relationships, which are rigorously correct for the homogeneous atmosphere, are also applicable to the inhomogeneous atmosphere.

Effects of Source-Detector Orientation

As indicated in Appendix F, point detectors were positioned at several source-detector orientations about a source to assess the effects of the nonuniform atmosphere.

The calculational results indicate, for the sources of radiation and ranges investigated, that the energy deposition at detector locations surrounding a source is independent of source-detector orientation provided that:

1. Total (time-integrated) energy deposition is expressed in units multiplied by $4\pi R^2$ and energy deposition per second in units multiplied by $4\pi R^2 \times t_u$.
2. Penetrations are expressed in mean free paths or g/cm^2.
3. Times are expressed in units of reduced time, t_r

where R = source-to-detector distance, cm

t_u = time of arrival of uncollided flux, sec

$t_r = (t - t_u)/t_u$

t = real time, sec.

Variation of Energy Deposition, from a 500-kev Source, with Source Altitude

From the discussion above it is evident that the ratio of collided dose rate to uncollided dose, i.e., the normalized collided dose rate, when multiplied by t_u and plotted against the reduced time, will be independent of the source-detector orientation.

To determine the validity of this scaling as a function of source altitude, normalized collided dose rates multiplied by t_u were compared for equal mean-

free-path (mfp) penetrations from the 500-kev sources at 15,000 and 50,000 ft.

Fig. 2, for example, displays the normalized collided dose rates at detectors located 3 mfp from their respective photon sources. The curves were found to be indistinguishable within the Monte Carlo statistical uncertainties that were involved.

Similar results were obtained over the range of source-detector penetrations considered (up to 9 mfp). On the basis of these findings, it is concluded that the energy deposition rates for the 500-kev source may be scaled to any source altitude between 15,000 and 50,000 ft. The validity of this scaling procedure for higher energy sources should be tested.

Analytical Description of Energy Deposition

Histograms of normalized collided dose rate vs time, at various detector locations surrounding the three considered sources, were constructed from the Monte Carlo data and examined in detail to determine if they could be represented by simple analytical fits.

The shape of the histograms, for penetrations up to 9 mfp for the 500-kev source, and 7 mfp for the 5-Mev source, suggested that an adequate analytical representation of the data could be obtained in the form of the sum of two decaying exponentials. The collided dose rate is then given by:

$$d_c(t)\ (\text{rads/sec}) = \frac{A\, e^{-\alpha_1 t_r} + B\, e^{-\alpha_2 t_r}}{4\pi R^2 \cdot t_u} \qquad (2)$$

where A, B, α_1, α_2 are functions of source energy (E_0) and mean free paths (λ) only.

The uncollided dose, D_u, is:

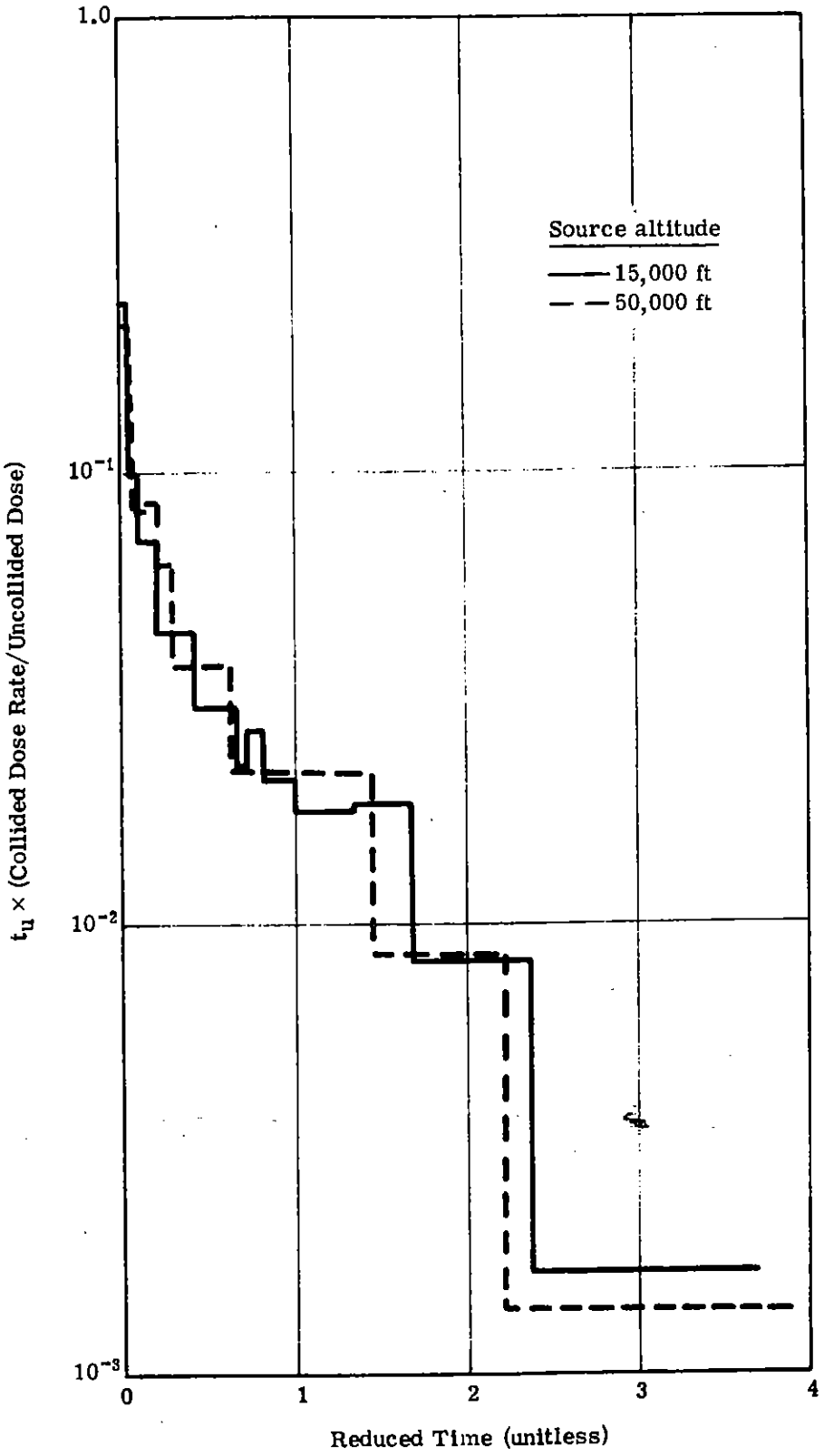

Fig. 2 — Ratio of Collided Dose Rate to Uncollided Dose as a Function of Source Altitude (Source: 500-kev photons; Detectors: 3 mfp along the horizontal)

$$D_u\,(\text{rads}) = \frac{e^{-\lambda}\,\bar{R}(E_0)}{4\pi R^2} \qquad (3)$$

where $\bar{R}(E_0) = 2.36 \times 10^{-10}$ rads/(photon/cm^2), E_0 = 500 kev[7]

$= 1.46 \times 10^{-9}$ rads/(photon/cm^2), E_0 = 5 Mev[7]

Hence,

$$\frac{d_C(t)}{D_u}\,(\text{sec}^{-1}) = \frac{e^{+\lambda}\,[A(E_0,\lambda)\,e^{-\alpha_1(E_0,\lambda)\,t_r} + B(E_0,\lambda)\,e^{-\alpha_2(E_0,\lambda)\,t_r}]}{t_u \cdot \bar{R}(E_0)} \qquad (4)$$

Plots of A, B and α_1, α_2 vs λ are presented for E_0 = 500 kev and 5 Mev as Figs. 3 and 4, and Figs. 5 and 6, respectively.

Examples of the adequacy of the fit to the Monte Carlo data can be seen in Figs. 7 and 8 (500-kev source) and Figs. 9 and 10 (5-Mev source), which correspond to energy deposition rates at detectors at various penetrations from the photon sources. (The statistical uncertainty of the Monte Carlo results is shown on all histograms.) On the figures, the solid curve represents the analytical fit from expression (4).

It is seen in Figs. 7 through 10 that the analytical fit does appear to represent adequately the Monte Carlo data for the temporal ranges investigated.

A limitation of the calculational results, discussed in more detail in Section VI, should be noted at this point. The width of the time bins in the Monte Carlo calculations was adjusted so that a sufficient number of scores could be obtained to make the statistical results meaningful. As a result, the important short temporal ranges, where the dose rates are at their maximum and are changing most rapidly with time, were represented by no more than two or three time intervals. Hence, much of the detail of the dose rate behavior at earliest temporal ranges was not obtained. Thus, the accuracy of the analytical fit at early temporal ranges has not been determined.

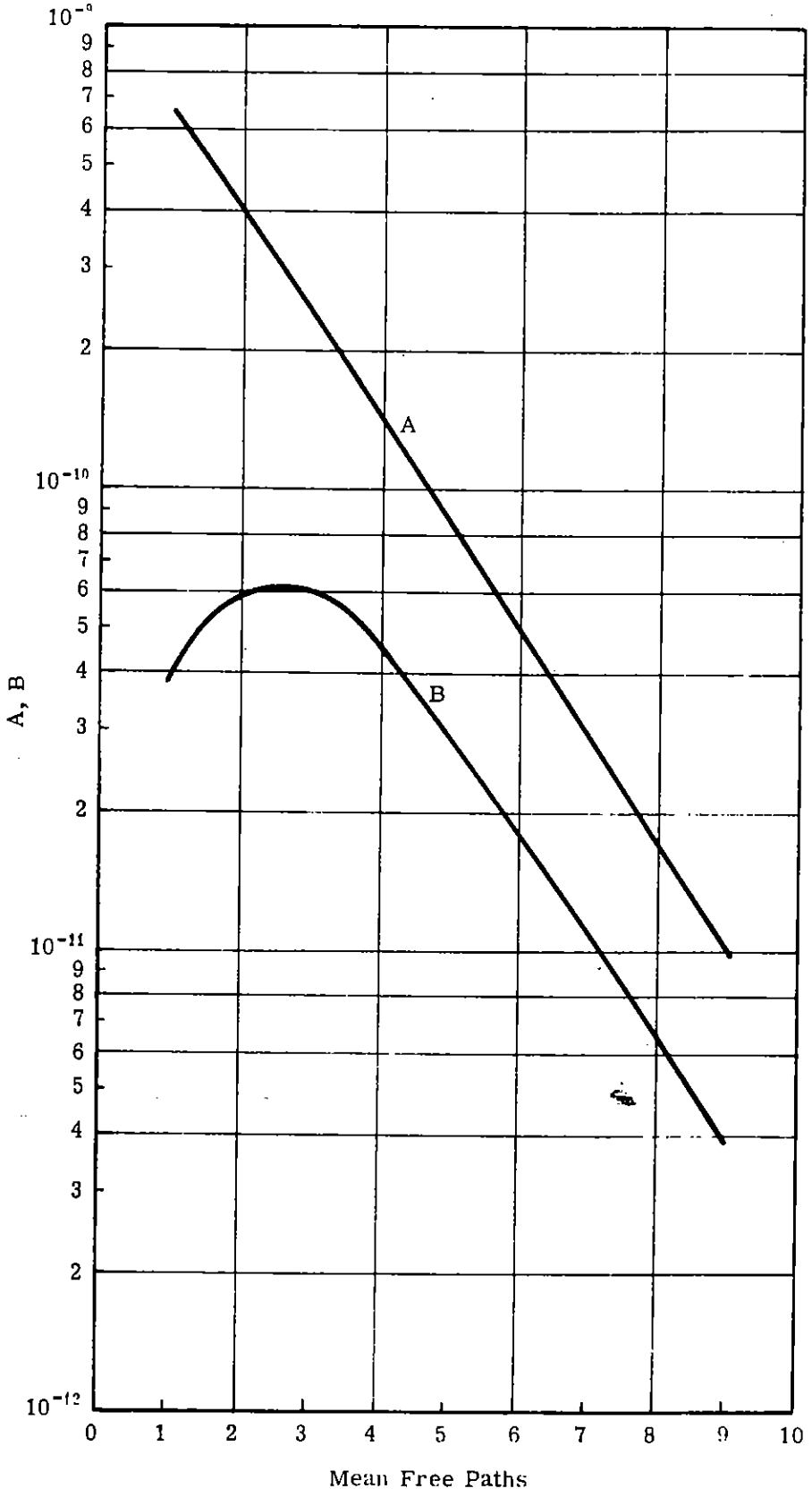

Fig. 3 — Dose Rate – 500-kev Photons – A and B Parameters

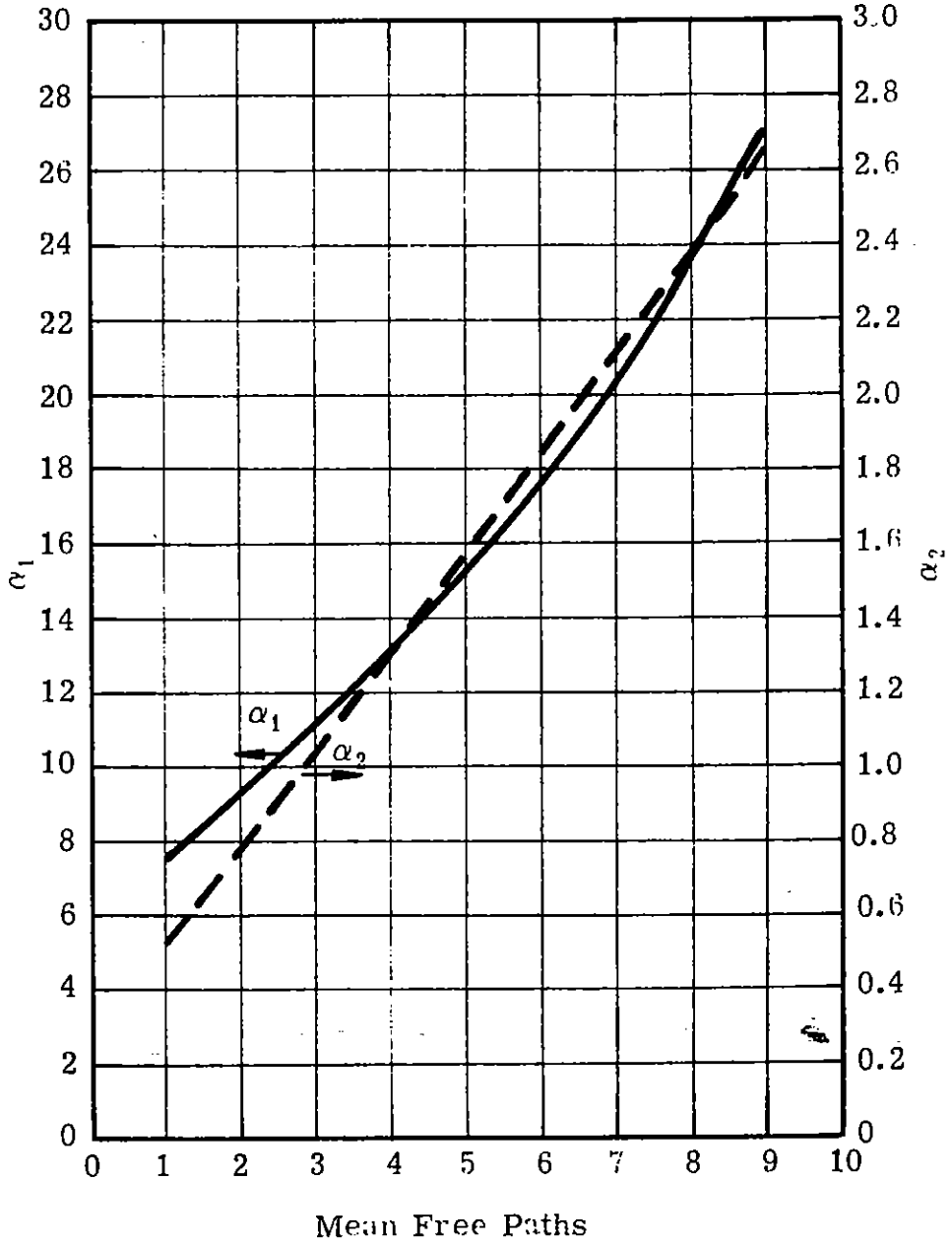

Fig. 4 — Dose Rate – 500-kev Photons – α_1 and α_2 Parameters

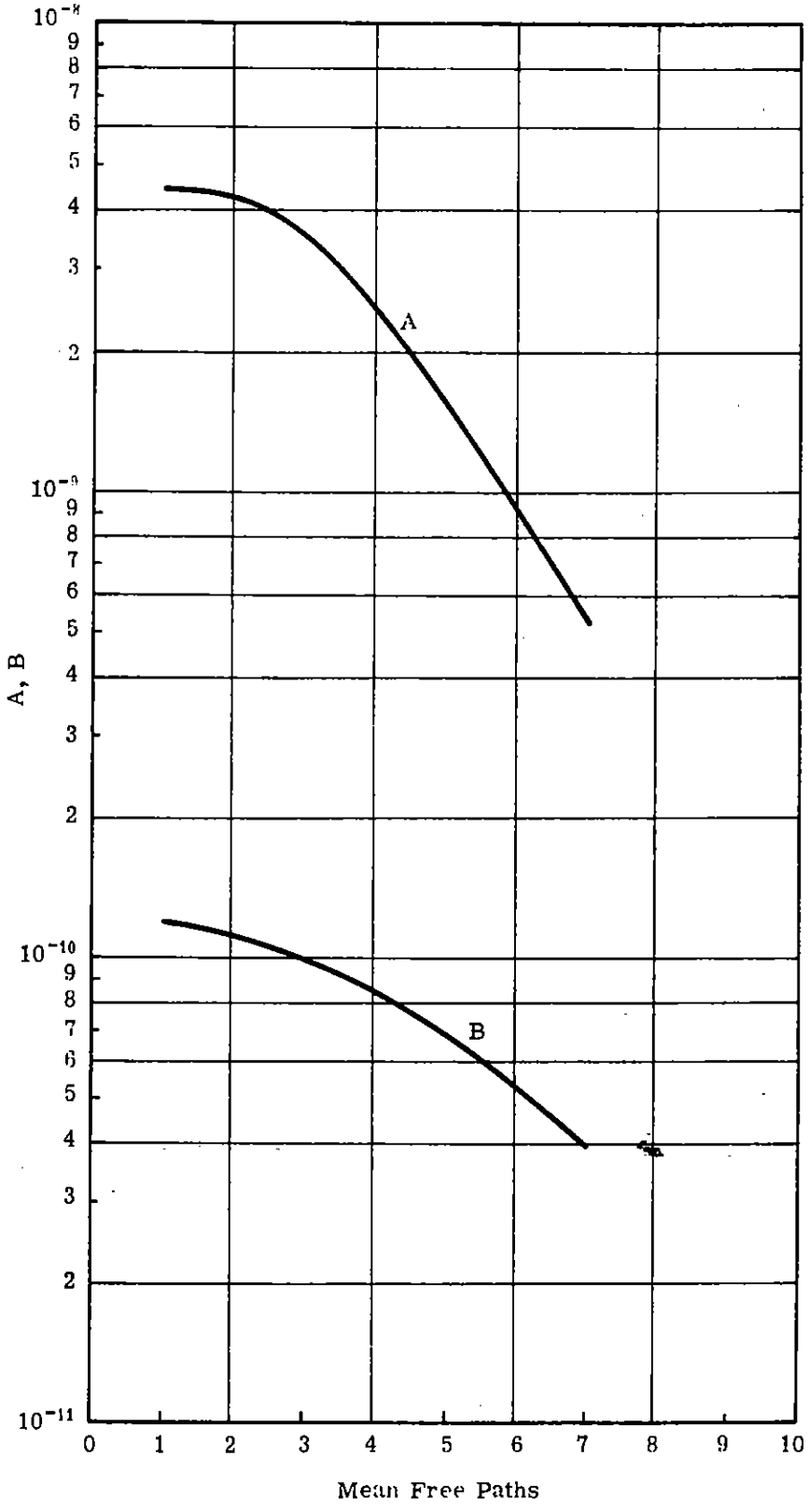

Fig. 5 — Dose Rate – 5-Mev Photons at 15,000 ft – A and B Parameters

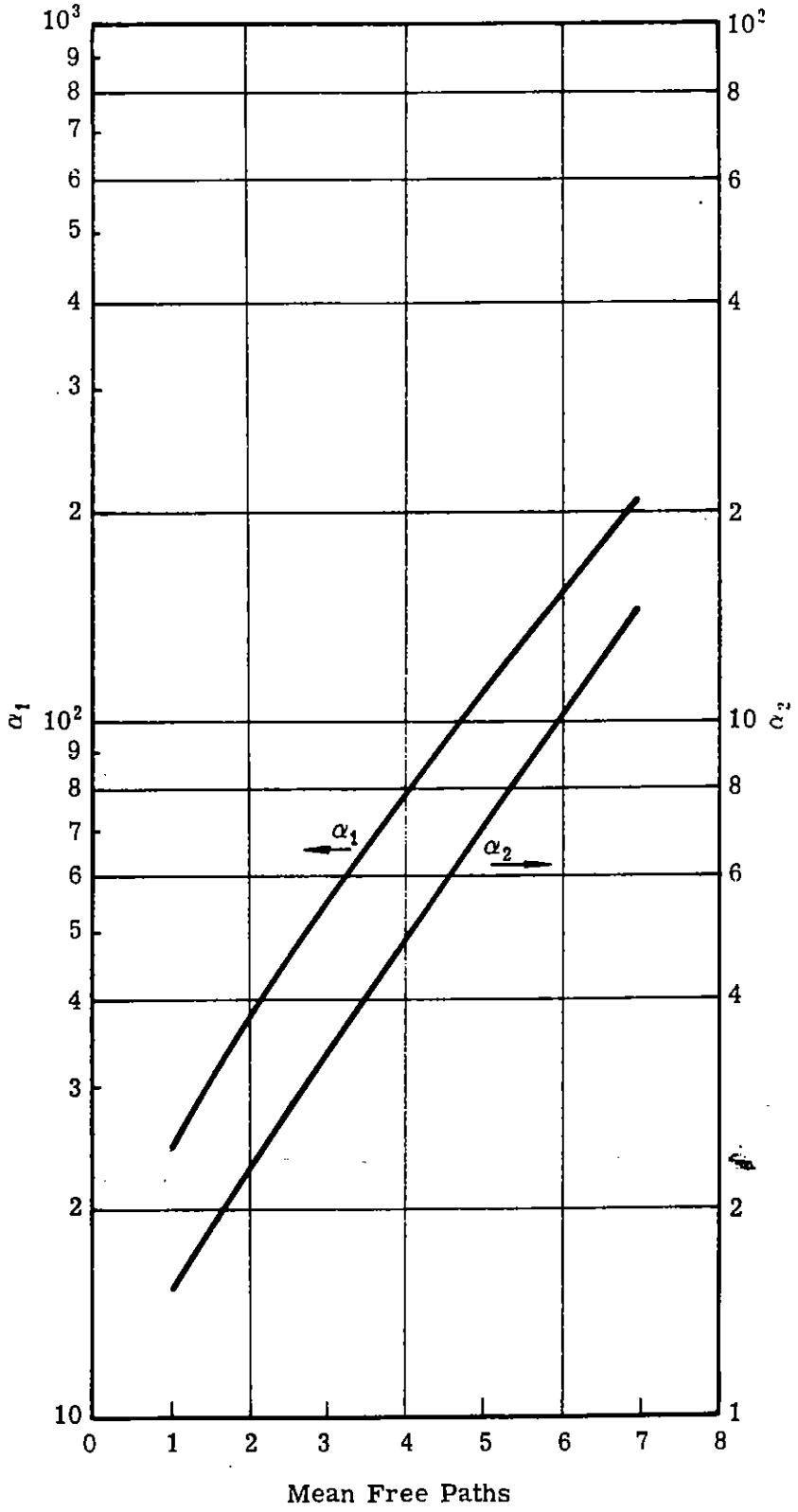

Fig. 6 — Dose Rate – 5-Mev Photons at 15,000 ft – α_1 and α_2 Parameters

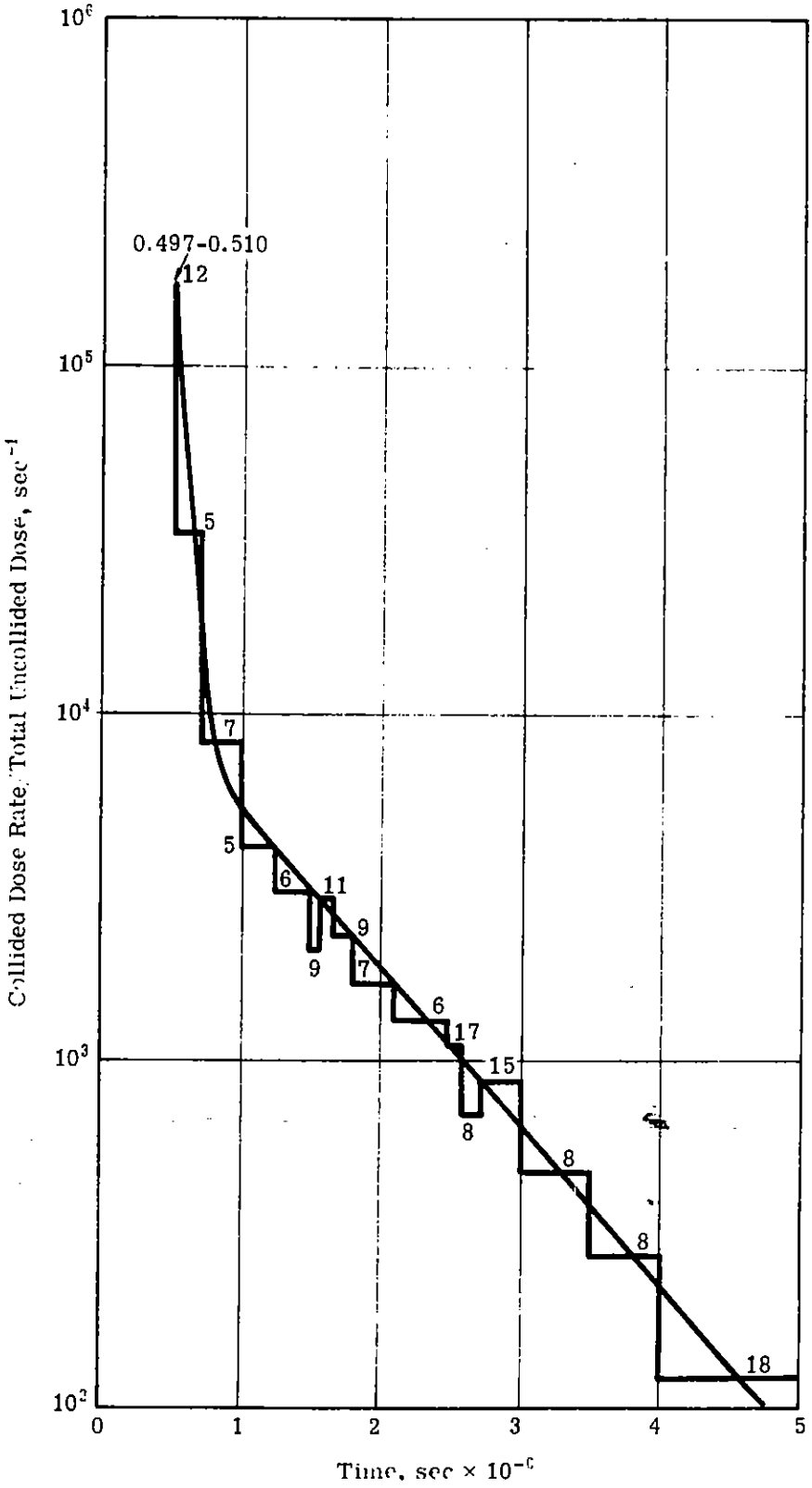

Fig. 7 — Collided Dose Rate [Source: 500-kev photons at 15,000 ft; Detector: 15,000 ft, 1 mfp (148.9 meters)]

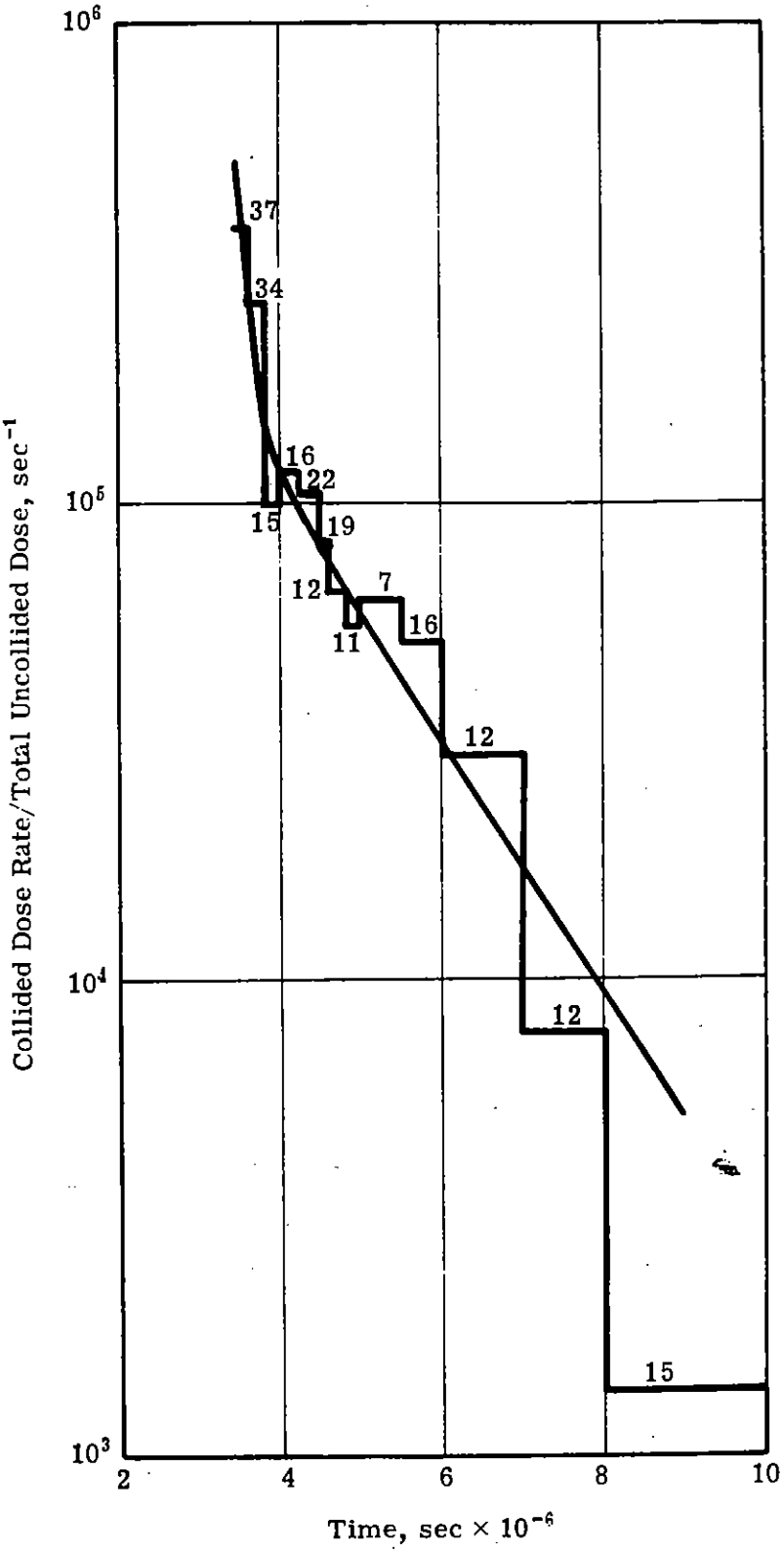

Fig. 8 — Collided Dose Rate [Source: 500-kev photons at 15,000 ft; Detector: 15,000 ft, 7 mfp (1042 meters)]

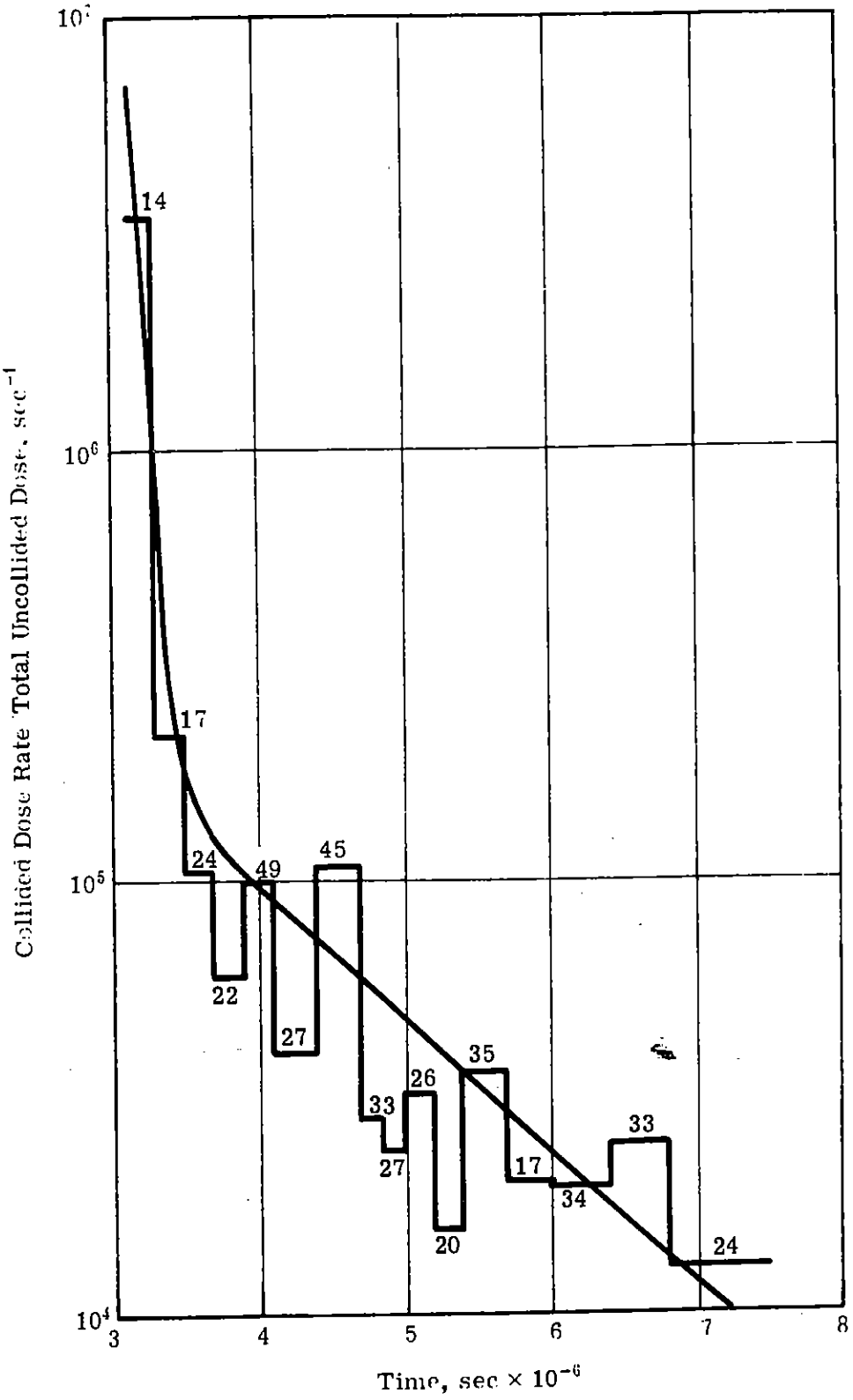

Fig. 9 — Collided Dose Rate [Source: 5-Mev photons at 15,000 ft; Detector: 15,000 ft, 2 mfp (438.2 meters)]

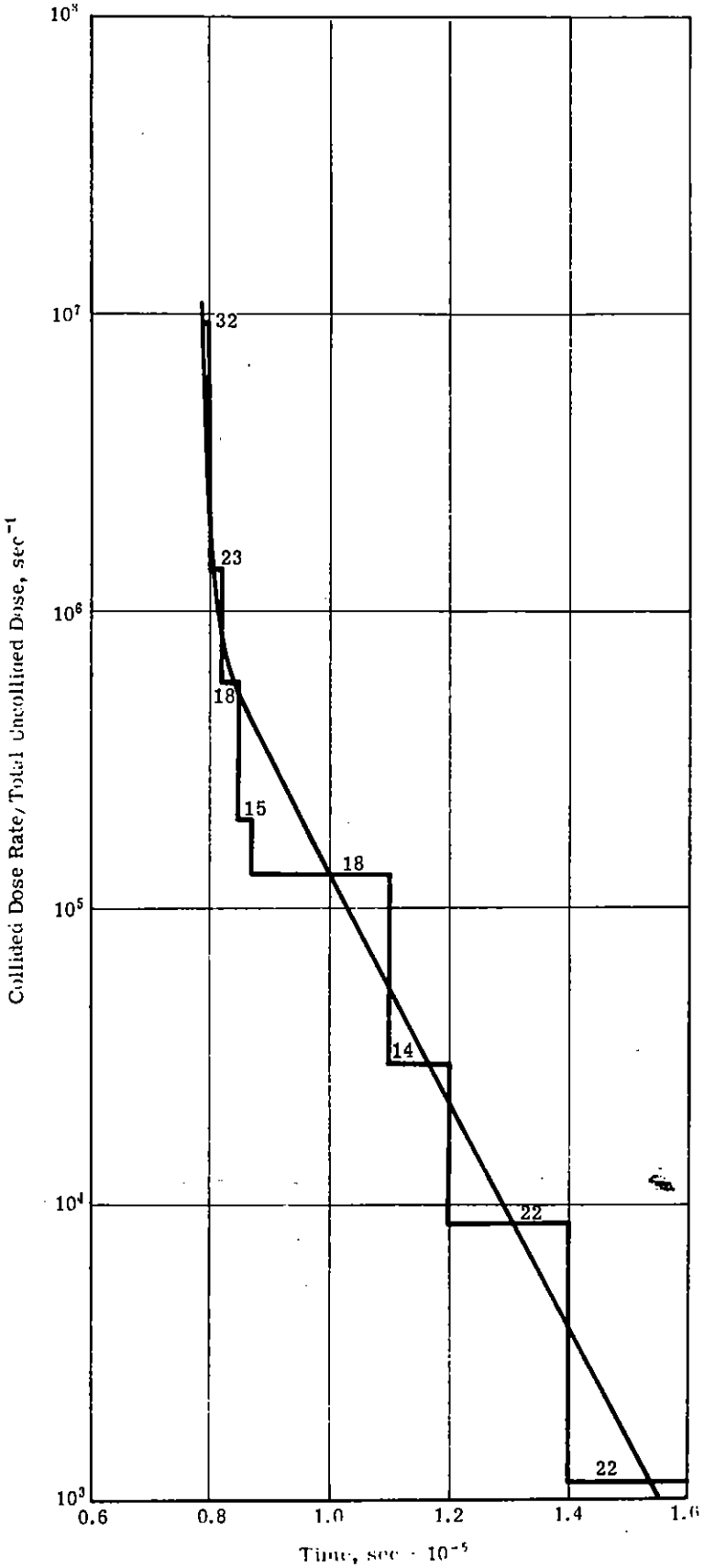

Fig. 10 — Collided Dose Rate [Source: 5-Mev photons at 15,000 ft; Detector: 15,000 ft, 5 mfp (2346 meters)]

Comparison of Dose Buildup Factors with Moments Method Results

The time-integrated energy deposition from collided photons, obtained by the integration of expression (2) over all real time, is given by:

$$D_c = \frac{\frac{A}{\alpha_1} + \frac{B}{\alpha_2}}{4\pi R^2} \tag{5}$$

The dose buildup factor, B_d, is defined as:

$$B_d = \frac{D_c + D_u}{D_u} \tag{6}$$

where D_u is given by (3) and D_c by (5).

Figs. 11 and 12 display for 5-Mev and 500-kev sources, respectively, the dose buildup factors in water as reported by Goldstein.[11] The Monte Carlo results of this study as well as the results obtained by expression (4) involving A, B, α_1, α_2 ("four-parameter fit") are displayed on the same figures. (It is assumed that for these photon energies the moments method results for water are applicable to air as well.)

The best fit through the "four parameter" points for the 5-Mev photons yields a curve very close to that of Goldstein. The best fit through the 500-kev "four parameter" data, however, yields a curve generally below the Goldstein curve, with a maximum deviation of about 25% at $\lambda \approx 4$ to 5. No explanation for this apparent discrepancy has been found.

RADIAL COMPTON CURRENTS

Effects of Source-Detector Orientation

The radial Compton currents at detectors surrounding a photon source of either 500 kev or 5 Mev also were analyzed to assess the effects of source-de-

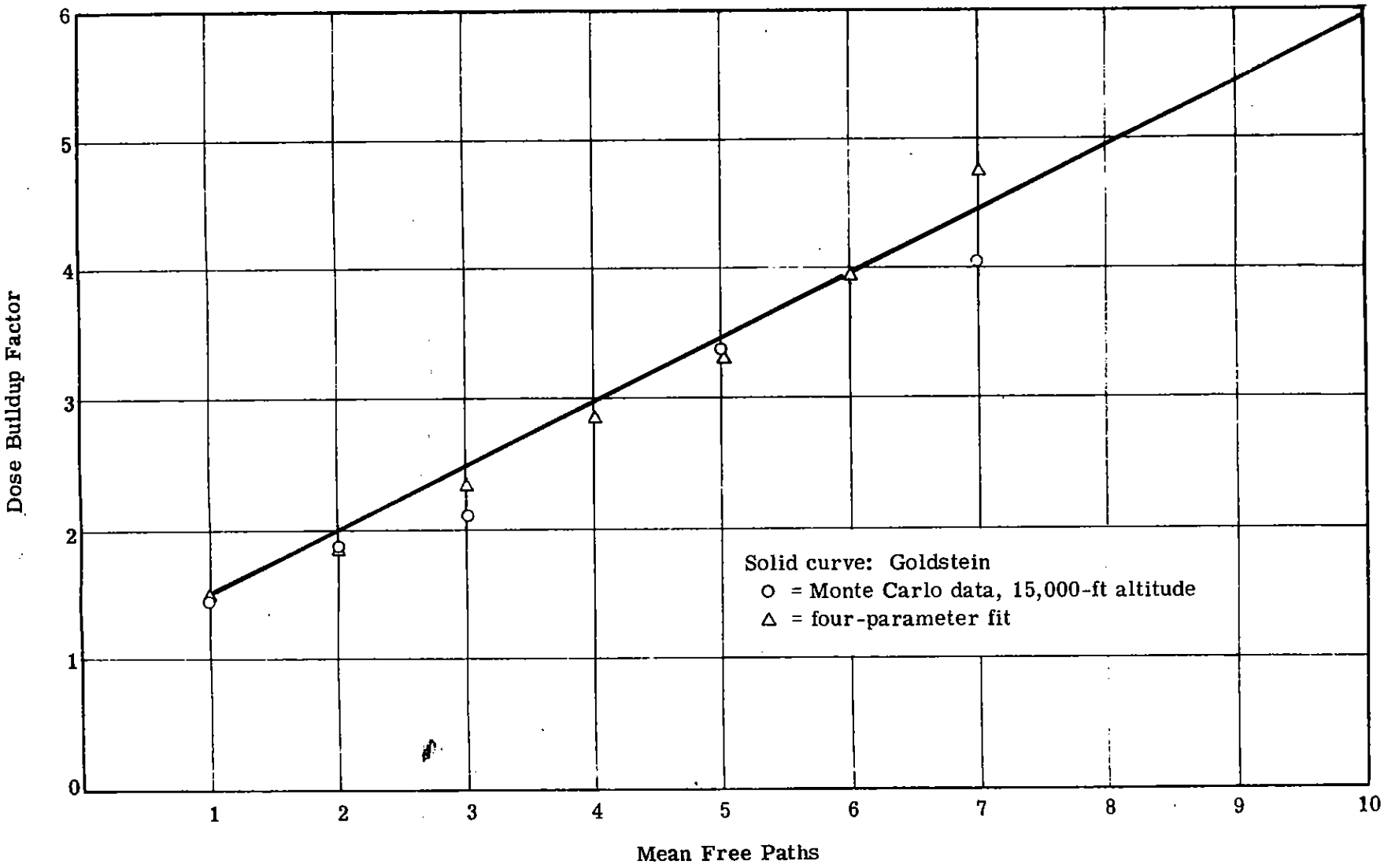

Fig. 11 — Dose Buildup Factor – 5-Mev Primary Photons

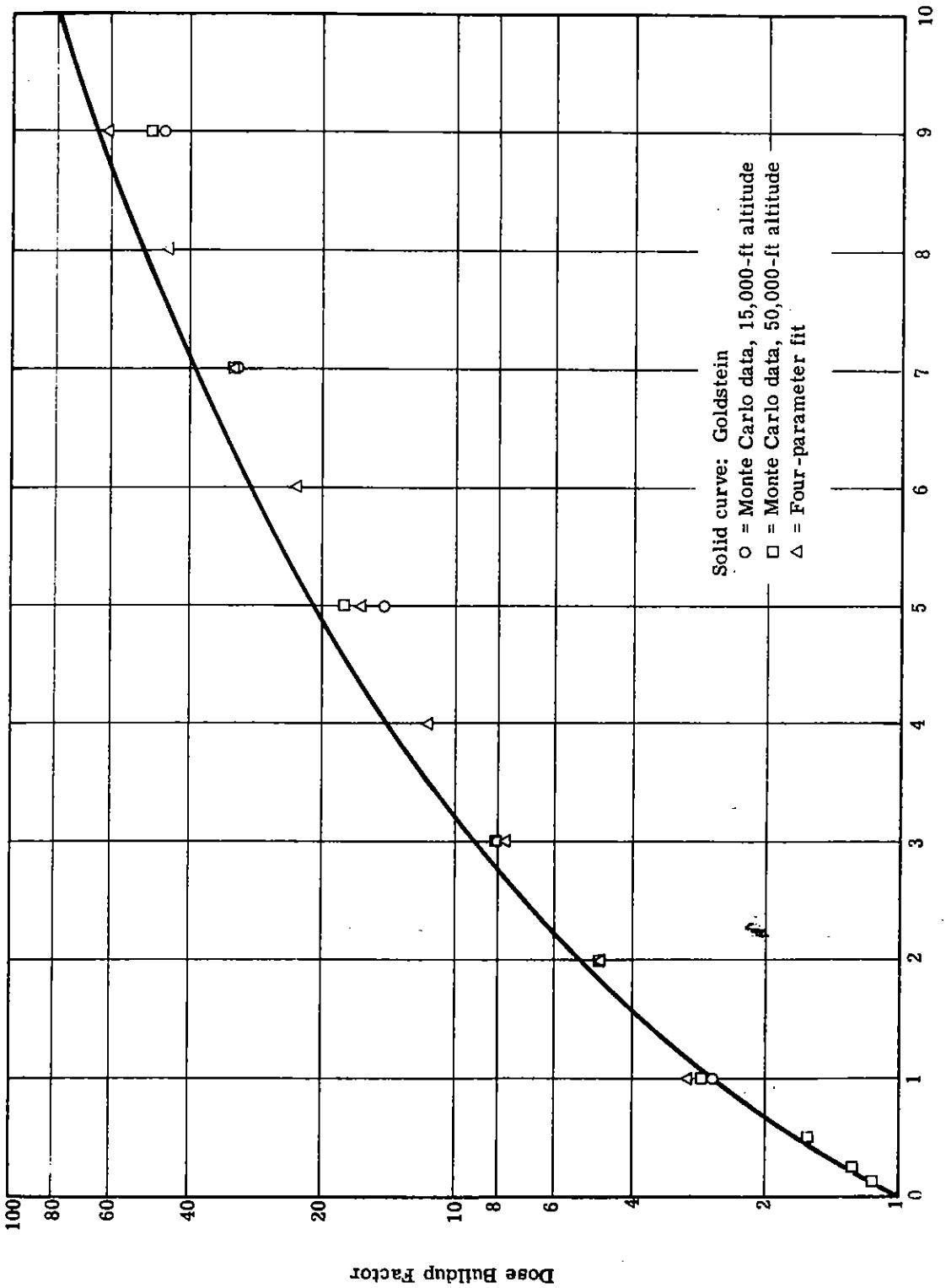

Fig. 12 — Dose Buildup Factor — 500-kev Primary Photons

tector orientation due to the nonuniform atmosphere. It was found, within the statistical accuracy of the Monte Carlo calculations, that the radial currents also are independent of source-detector orientation providing that the units of current are multiplied by $4\pi R^2 \times t_u$ and the times are in units of reduced time.

Variation of Radial Currents, from a 500-kev Source, with Source Altitude

Curves of $t_u \times$ (collided radial current/uncollided radial current) at an equal number of mean free paths from 500-kev photons at 15,000 and 50,000 ft were compared to assess the effect of the source altitude in the nonuniform atmosphere. Fig. 13, for example, displays the normalized radial currents at a penetration of 3 mfp from the respective sources. The two curves are indistinguishable within the Monte Carlo statistics. Similar results were found for other penetrations. Hence, it appears that scaling with altitude of radial currents from a 500-kev source is permissible from 15,000 to 50,000 ft for penetration ranges at least up to 9 mfp.

Analytical Description of Radial Compton Currents

Histograms of radial currents from collided photons, normalized to current from uncollided photons, at various penetrations from the photon sources, were obtained from the Monte Carlo data and analyzed carefully.

The shape of the histograms indicates that the data can be represented by a two-exponential expression similar to expression (4). Curves of A and B, α_1, and α_2 are presented as Figs. 14 and 15 (500-kev source) and Figs. 16 and 17 (5-Mev source). The appropriate $\overline{R}(E_0)$ terms for the radial currents from uncollided photons are:

$$\overline{R}\,(500 \text{ kev}) = 1.648 \times 10^{-3}*$$

$$\overline{R}\,(5 \text{ Mev}) = 3.258 \times 10^{-2}*$$

*Determined by separate Monte Carlo studies at United Nuclear Corporation.

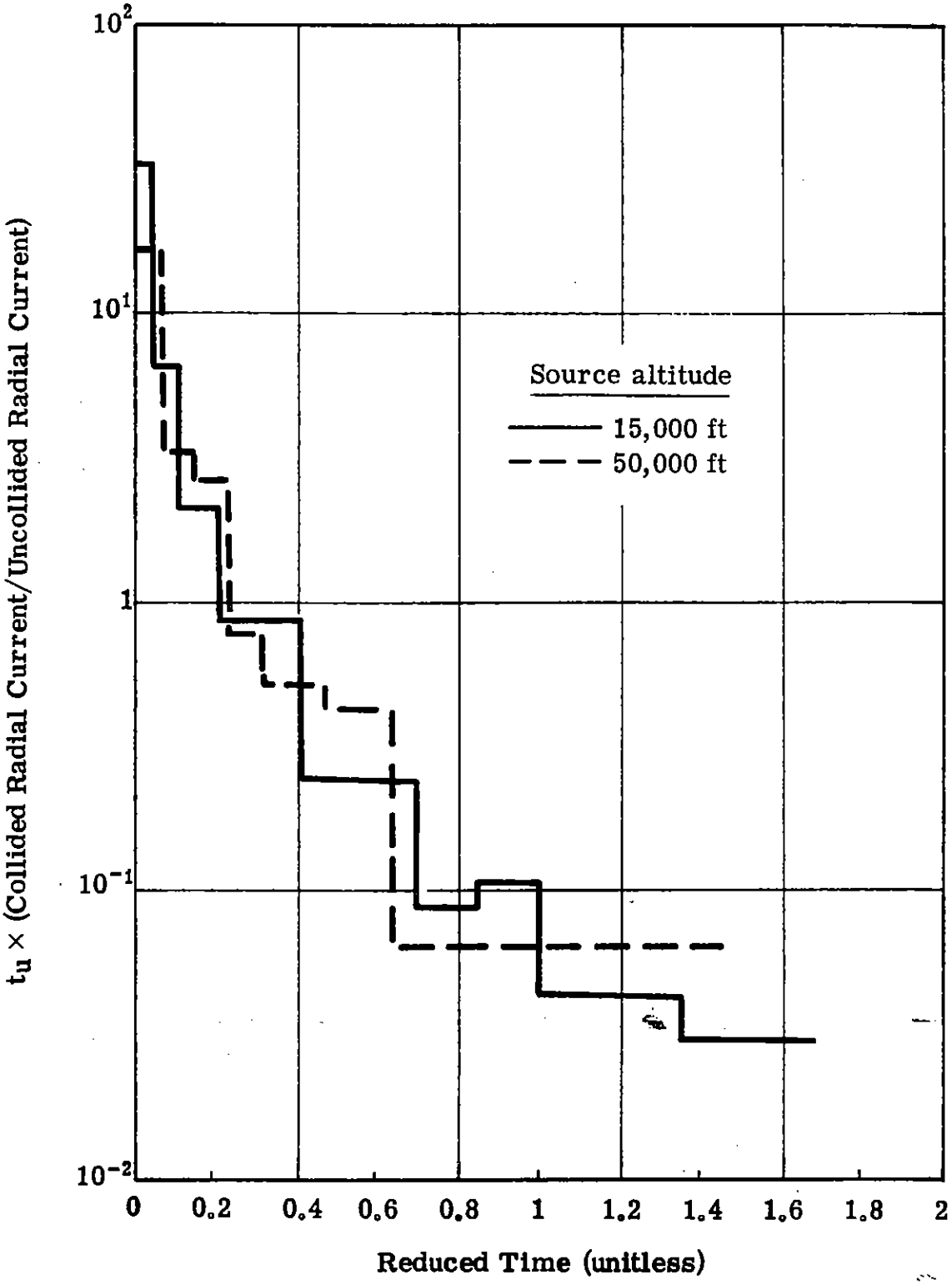

Fig. 13 — Ratio of Collided Radial Compton Current to Uncollided Radial Compton Current as a Function of Source Altitude – (Source: 500-kev photons; Detectors: 3 mfp along the horizontal)

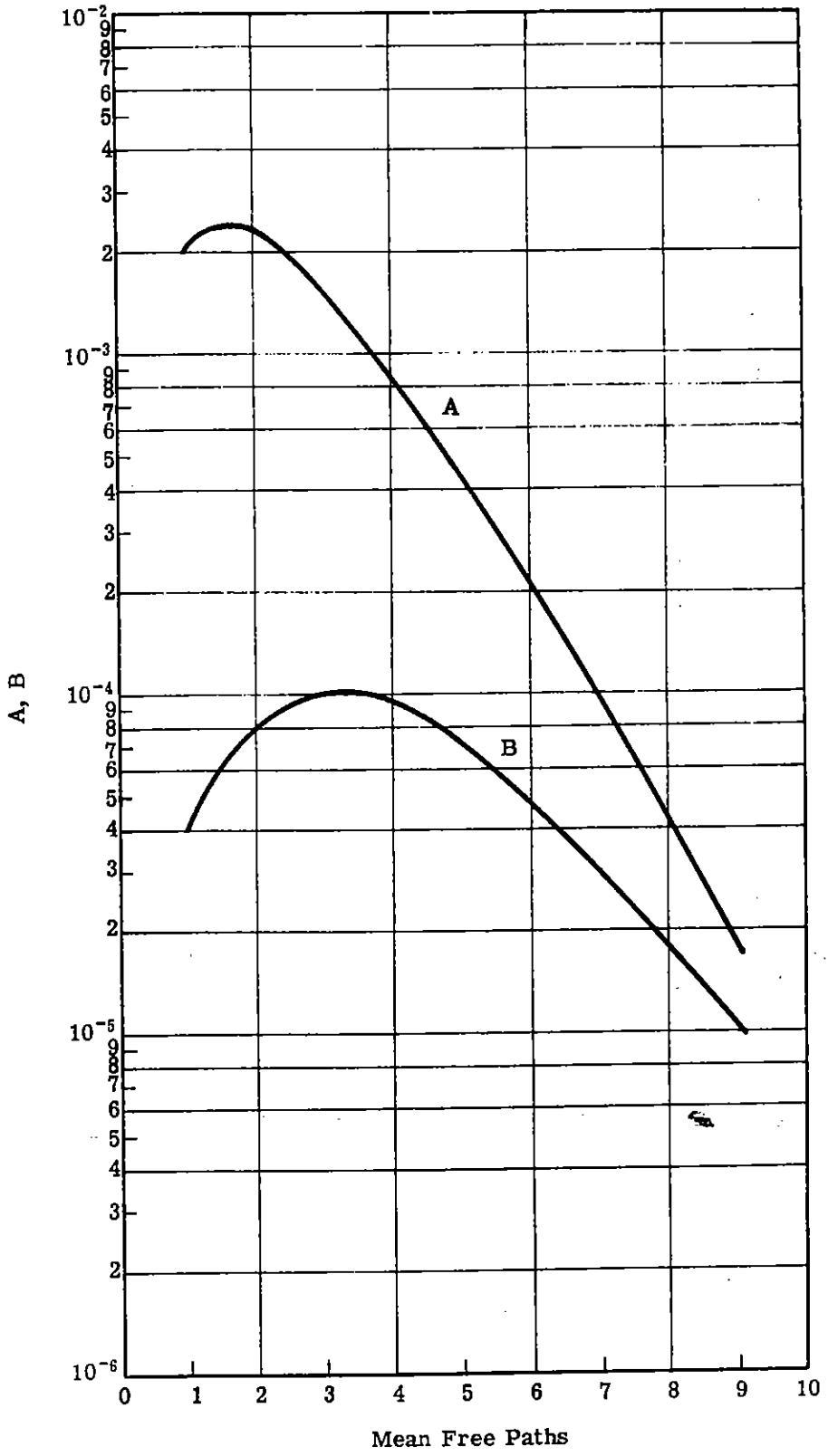

Fig. 14 — Radial Compton Current – 500-kev Photons – A and B Parameters

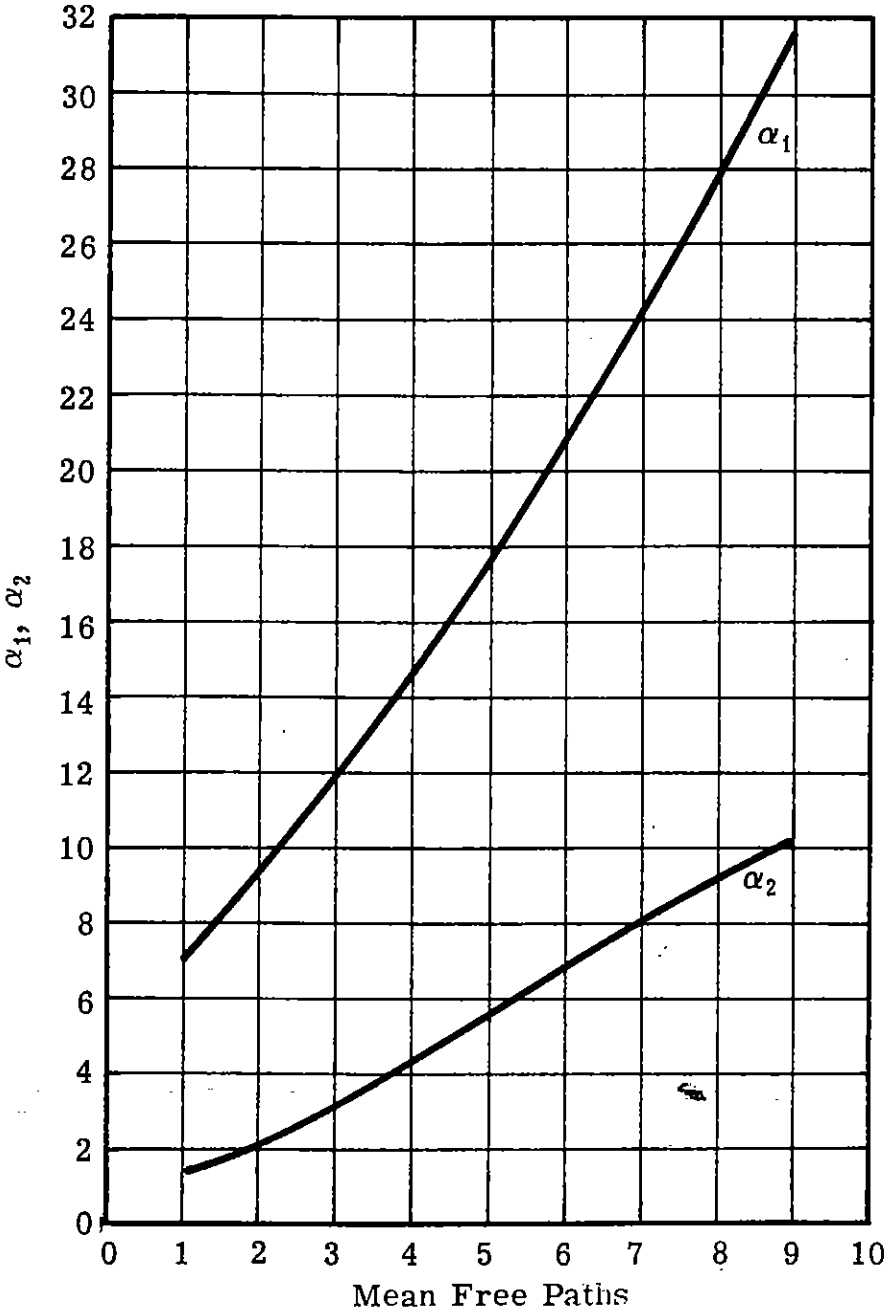

Fig. 15 — Radial Compton Current – 500-kev Photons – α_1 and α_2 Parameters

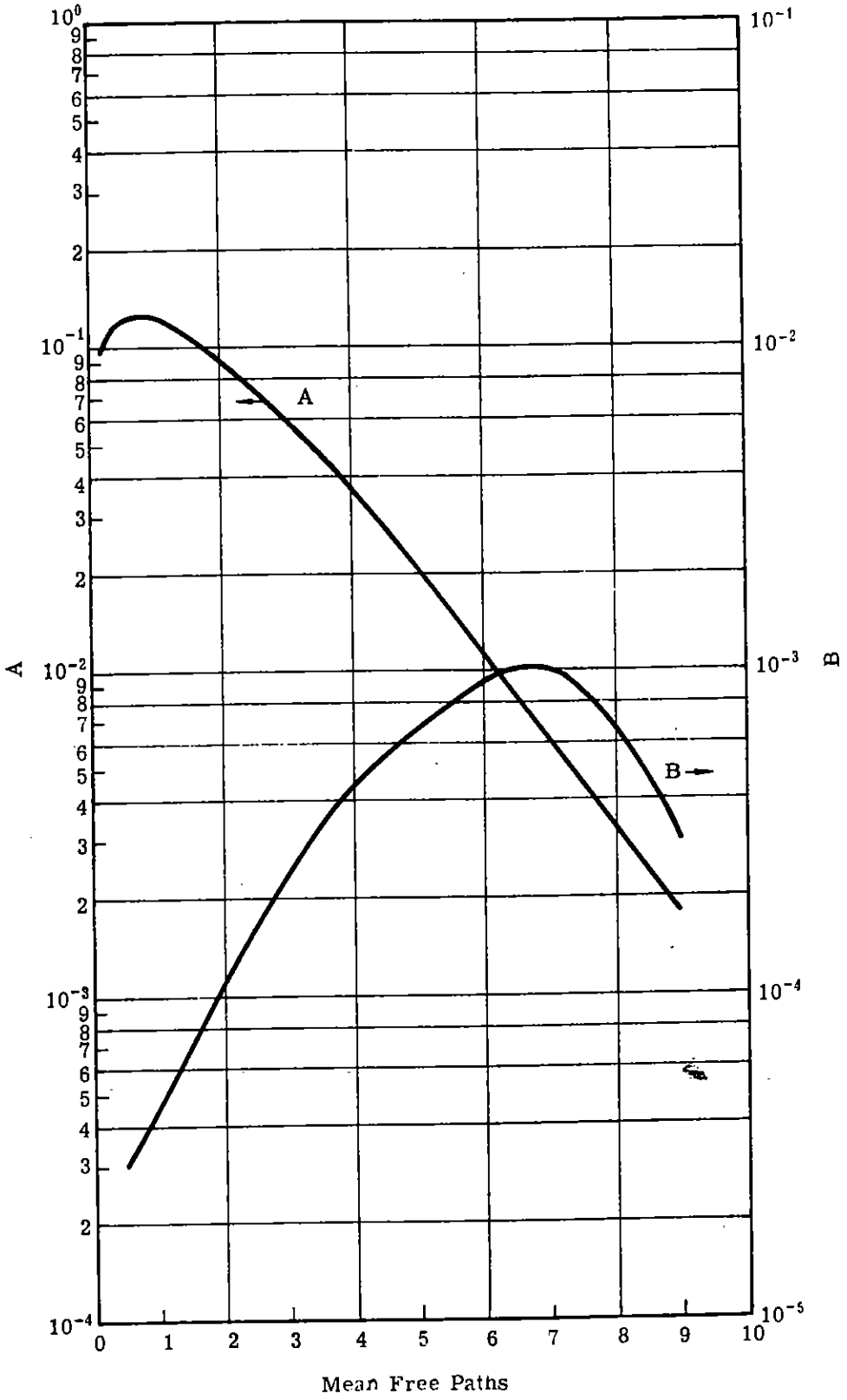

Fig. 16 — Radial Compton Current – 5-Mev Photons at 15,000 ft; A and B Parameters

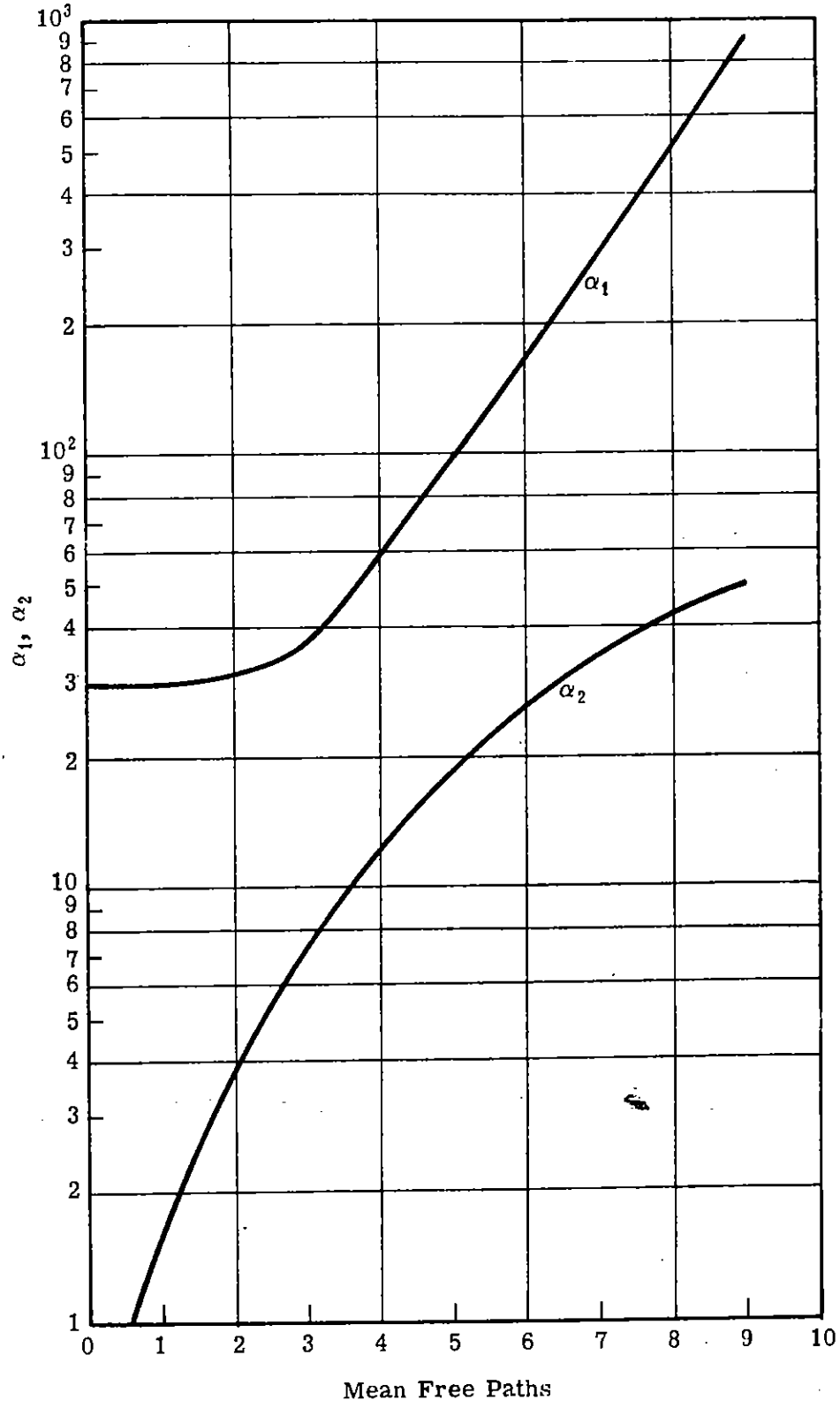

Fig. 17 — Radial Compton Current – 5-Mev Photons at 15,000 ft – α_1 and α_2 Parameters

Examples of the analytical fit to the Monte Carlo data are given in Figs. 18 and 19 (500-kev source) and Figs. 20 and 21 (5-Mev source) which represent normalized radial currents at detector locations at various penetrations from the photon sources.

It should be noted, once again, that the relatively broad time intervals at short temporal ranges impose a limitation on our knowledge of the validity of the analytical fit at very short temporal ranges. This is discussed further in Section VI.

Comparison of Radial Compton Currents with Those in the Literature

The time-integrated radial currents as functions of penetration from the 500-kev and 5-Mev sources were calculated and normalized to $R^2 \times$ current (in statcoulombs) at sea level air density. The results were superimposed on a figure by LeLevier[12] displaying radial currents from 1, 1½, 2, 3, and 4-Mev photons and are presented as Fig. 22. It is seen that the present values are consistent with those reported by Le Levier.

POLAR COMPTON CURRENTS

Effects of Source-Detector Orientation

Fig. 23 displays the time-integrated polar current as a function of source-detector orientation, with penetration in mean free paths as the parameter. This set of curves is applicable to detector locations surrounding the 500-kev source at 15,000 ft. (Note that in the frame of reference used in this report, net downward flow of electrons is considered to be positive in sign.)

It is seen that the magnitude of the polar currents is at a maximum at and symmetric about 90° (coaltitude source and detector), and that it decreases monotonically to zero as the angle varies either to straight up or to straight down.

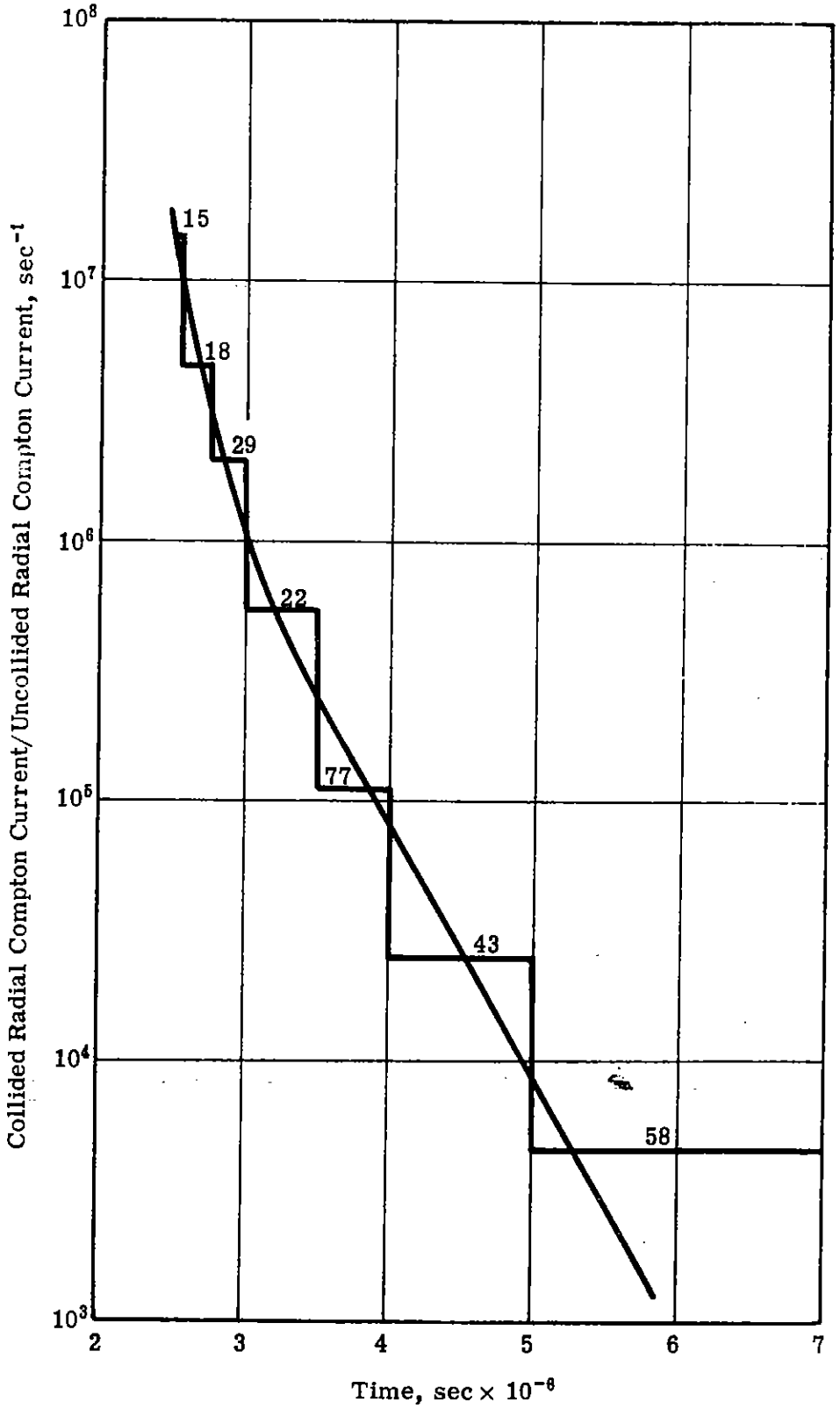

Fig. 18 — Collided Radial Compton Current [Source: 500-kev photons at 15,000 ft; Detector: 15,000 ft, 5 mfp (744.5 meters)]

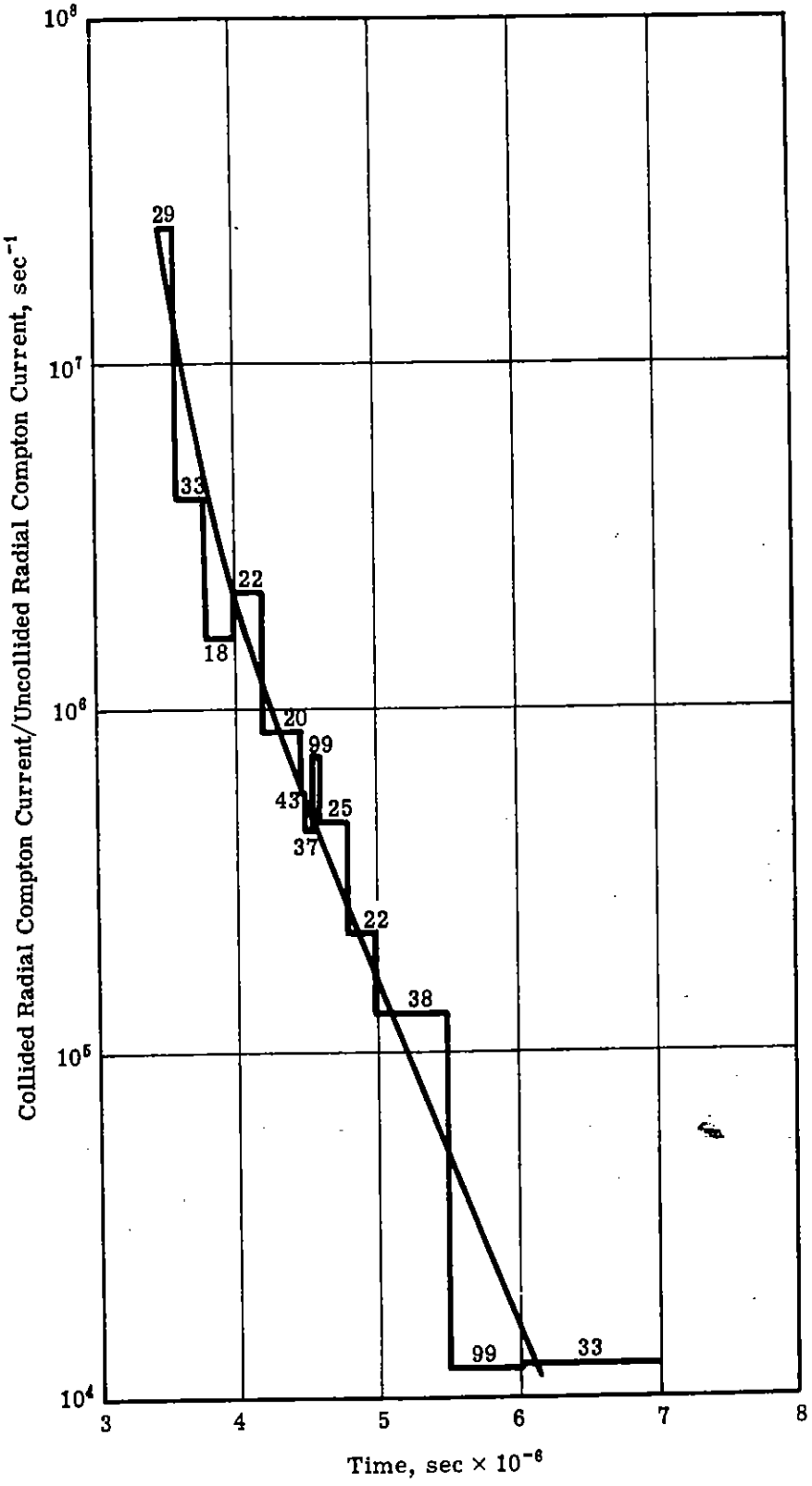

Fig. 19 — Collided Radial Compton Current [Source: 500-kev photons at 15,000 ft; Detector: 15,000 ft, 7 mfp (1042.0 meters)]

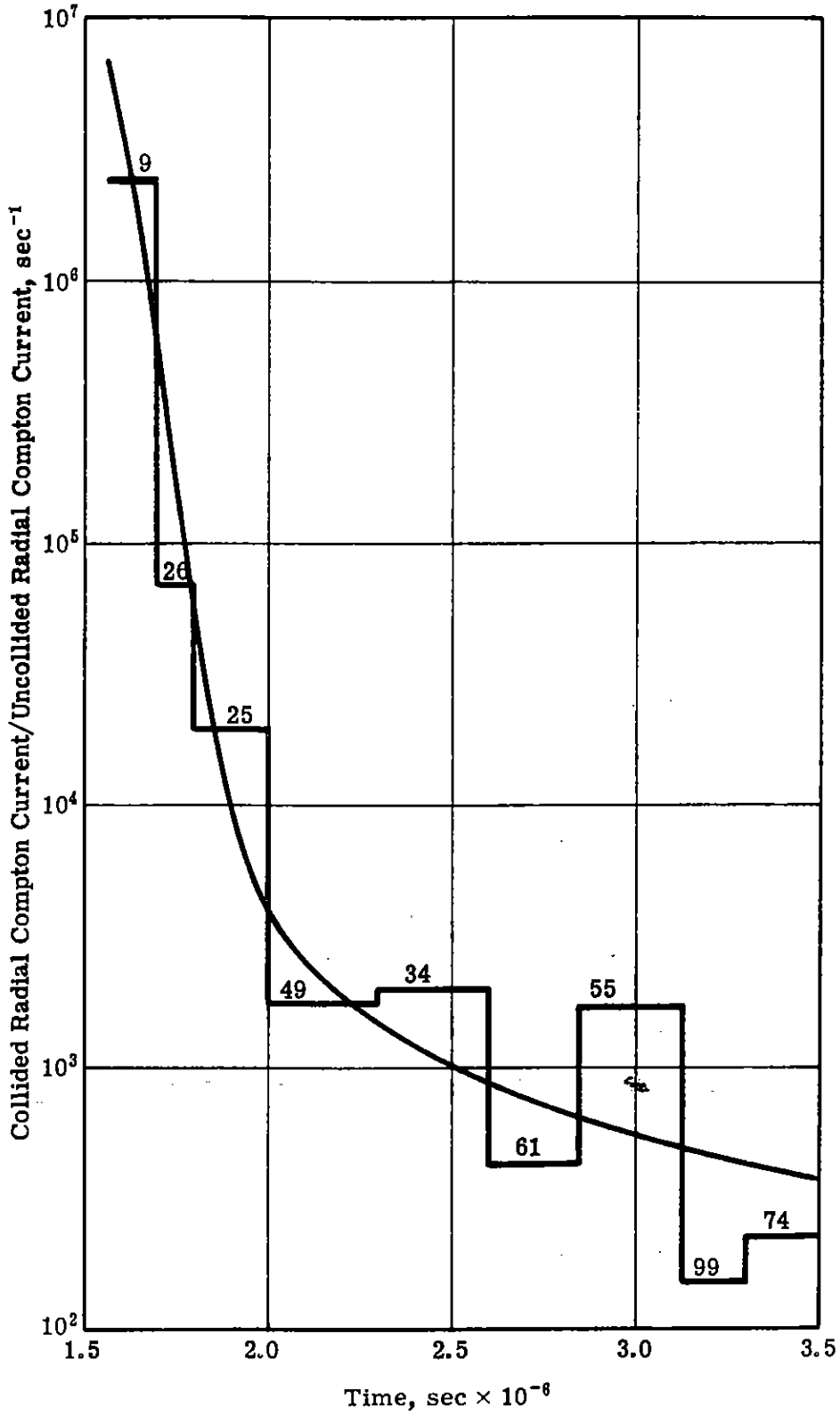

Fig. 20 — Collided Radial Compton Current [Source: 5-Mev photons at 15,000 ft; Detector: 15,000 ft, 1 mfp (469.1 meters)]

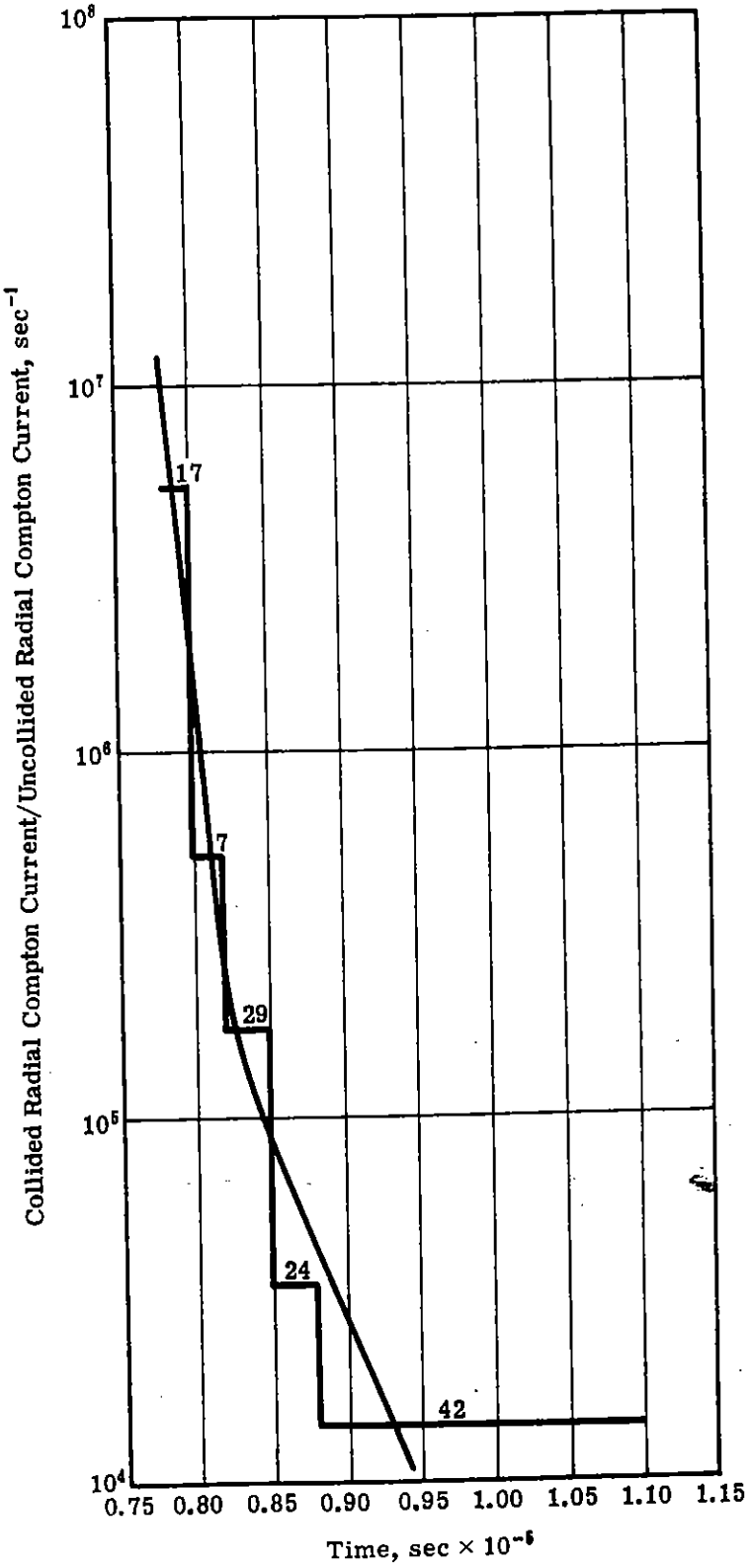

Fig. 21 — Collided Radial Compton Current [Source: 5-Mev photons at 15,000 ft; Detector: 15,000 ft, 5 mfp (2346 meters)]

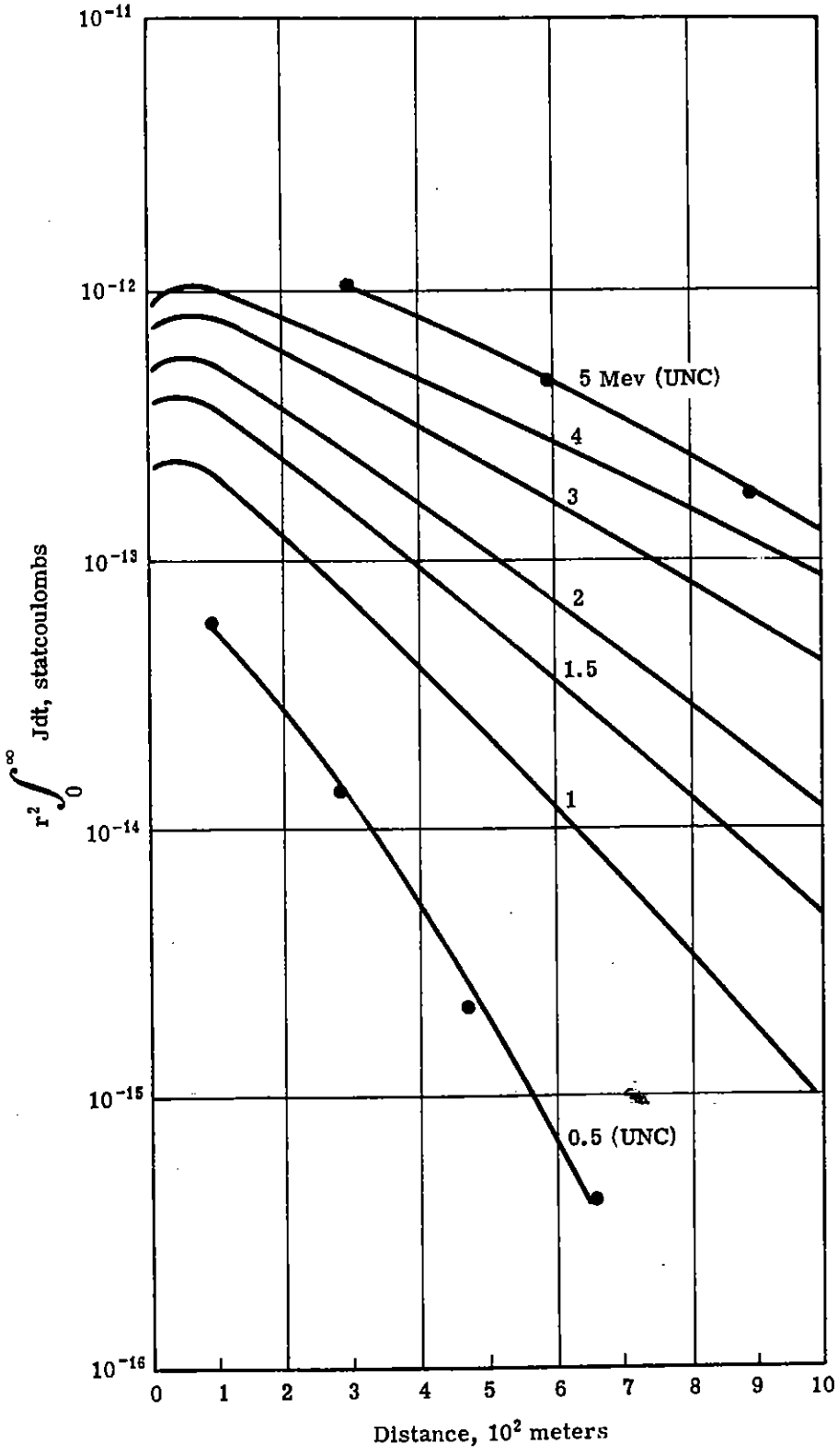

Fig. 22 — Integrated Radial Compton Current vs Distance at Sea Level Air Density

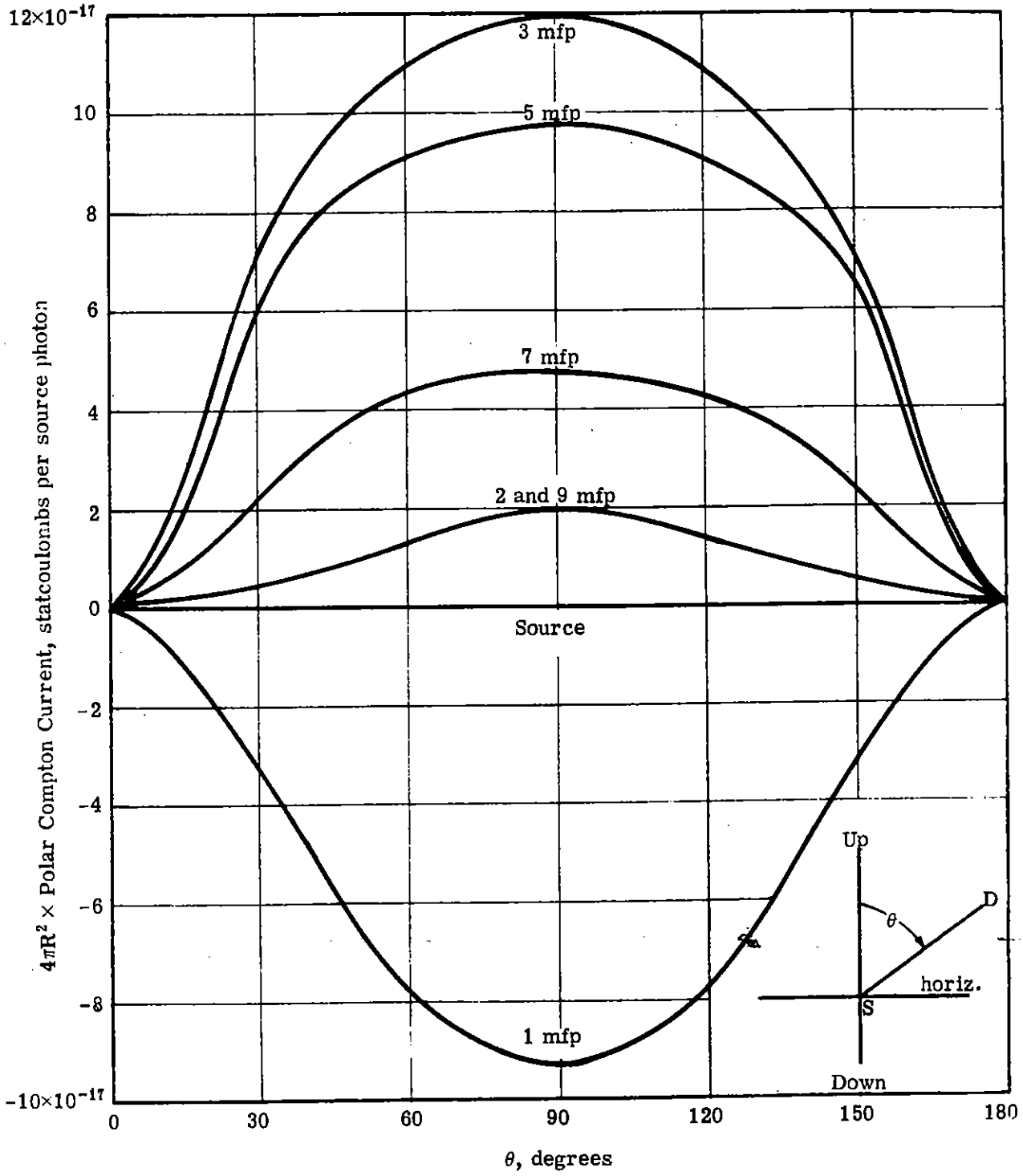

Fig. 23 — Polar Compton Currents – 500-kev photons at 15,000 ft (Polar Current as Function of Source-Detector Orientation)

The shape of the curve is seen to be a function of the penetration distance. A reasonable fit to the polar current data as a function of source-detector angle, θ, and penetration, λ, is given by

$$I_c(\lambda,\theta) = I_c(\lambda,90°)\cdot \left| (\sin\theta)^{n(\lambda)} \right| \qquad \text{for } 20° \leq \theta \leq 160° \tag{7}$$

where $\theta = 90°$ corresponds to coaltitude source and detector.

$$n(\lambda) = 1.35 - 0.15\,\lambda \qquad 1 \leq \lambda \leq 5$$
$$= 0.60 \qquad \lambda > 5$$

For $\theta < 20°$ or $\theta > 160°$, the polar current is very small and probably insignificant for the temporal and spatial ranges of this report. A suggested fit for this angular range is

$$I_c(\lambda,\theta) = \frac{I_c(\lambda,20°)\cdot\theta^2}{400} \qquad \theta < 20°$$
$$I_c(\lambda,\theta) = \frac{I_c(\lambda,20°)\cdot(180°-\theta)^2}{400} \qquad \theta > 160° \tag{8}$$

The angular dependencies of polar current from the other two primary photon sources were not studied in as much detail as were the dependencies for the 500-kev source at 15,000 ft. Although the angular descriptions obtained do seem to differ somewhat from those shown in Fig. 23 (particularly for the 5-Mev source at 15,000 ft where the angular dependence is more sharply peaked about $\theta = 90°$), expressions (7) and (8) can also be used to describe, to a first approximation, the effect of source-detector orientation upon polar currents for these two sources.

The time dependence of the variation of polar current with source-detector orientation, θ, was investigated by examining curves of polar current as a function of θ for reduced times of 0.25, 0.50, 1.0, and 1.5 at detectors positioned 3 mfp from the 500-kev source at 15,000 ft. These curves, along with the time-integrated

curve (as in Fig. 23), are presented on the same set of coordinates in Fig. 24. Surprisingly, it is seen that the functional relationship between polar current and source-detector orientation is not strongly dependent upon time.

The Monte Carlo data were not sufficient to allow examination of this dependency over the range of penetrations involved in this study. Until more detailed information is available (see Section VI), expressions (7) and (8) can be used to describe both the time-integrated and time-dependent relationship between polar current and source-detector orientation.

Polar Current as a Function of Penetration

Fig. 25 displays the complex behavior of time-integrated polar currents vs horizontal penetration (mfp) from the 500-kev source at 50,000 ft. These data, of course, can be scaled to detector positions off the horizontal axis by use of expressions (7) or (8).

At short ranges there is a net upward flow of electrons (negative current) caused by the increased probability of scattering toward a detector for photons emitted downward into the denser medium. As the penetration distance is increased, it becomes harder for the downward-emitted photons to reach the detector through the denser medium until, at about 2 mfp, the positive and negative contributions are equal and there is a null in the time-integrated polar current. Beyond this null position the net flow of electrons is always downward.

Figs. 26 and 27 display the same curves for the 500-kev source and 5-Mev source at 15,000 ft. It is seen that the curves are different in magnitude although the general behavior of each of the three curves with increasing penetration is quite similar. Investigations for source energies and altitudes intermediate to those of this study are necessary before the functional relationships between polar currents and source altitude and energy can be established (see Section VI).

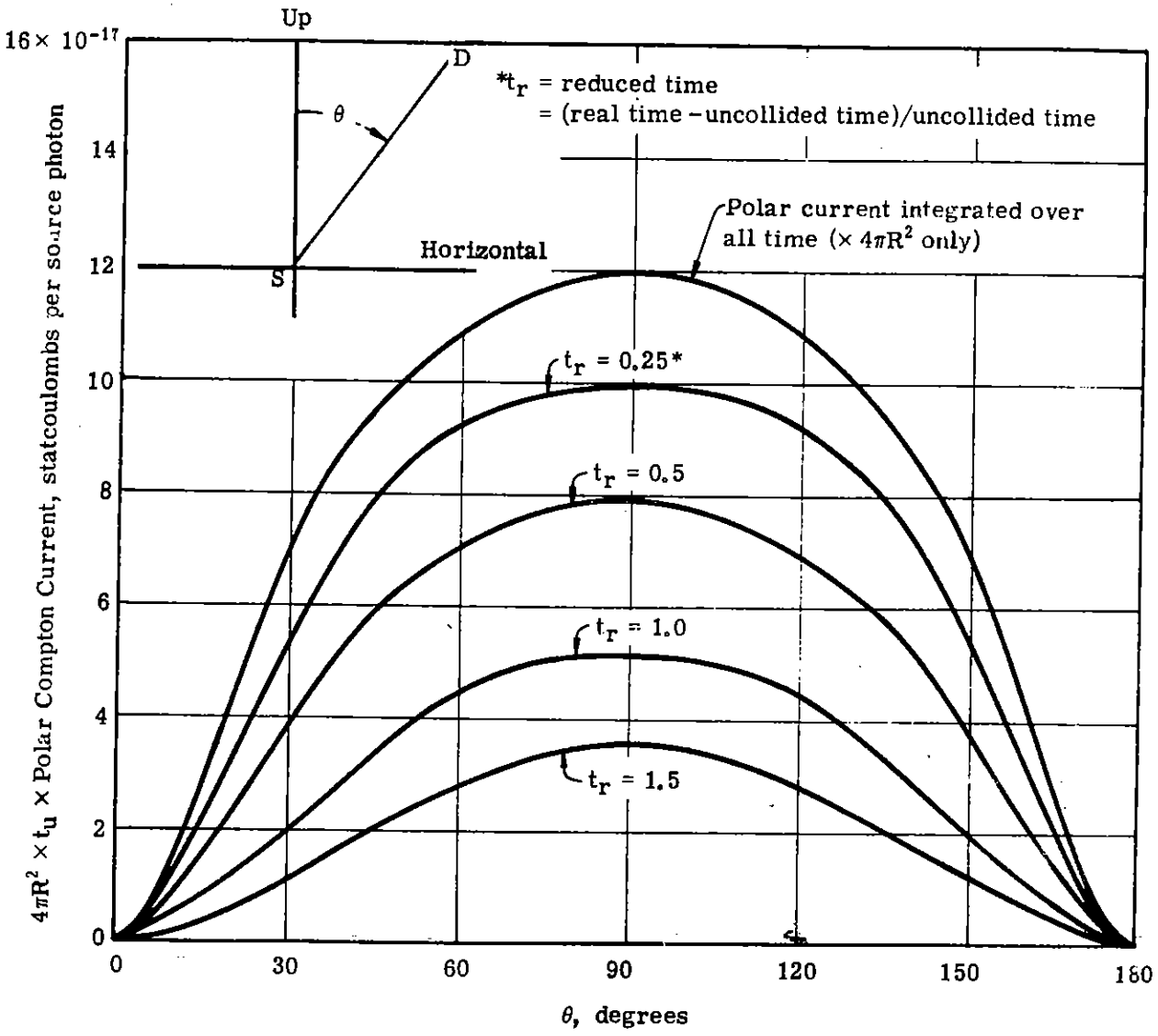

Fig. 24 — Time Dependence of Polar Compton Current vs Source-Detector Orientation (Source: 500-kev photons at 15,000 ft; Detector: 3 mfp from source)

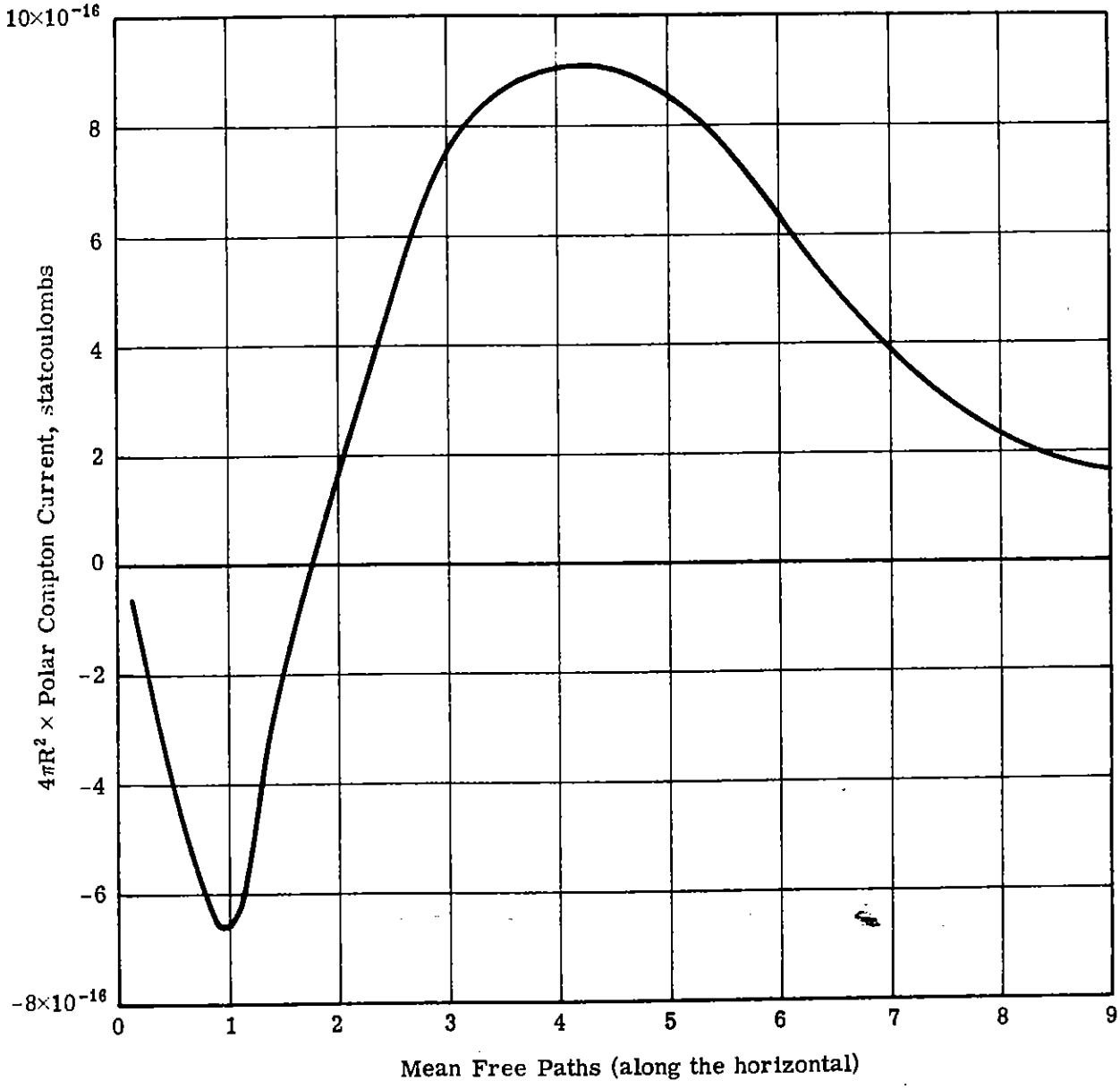

Fig. 25 — Polar Compton Current vs Source-Detector Penetration along the Horizontal (500-kev photons at 50,000 ft)

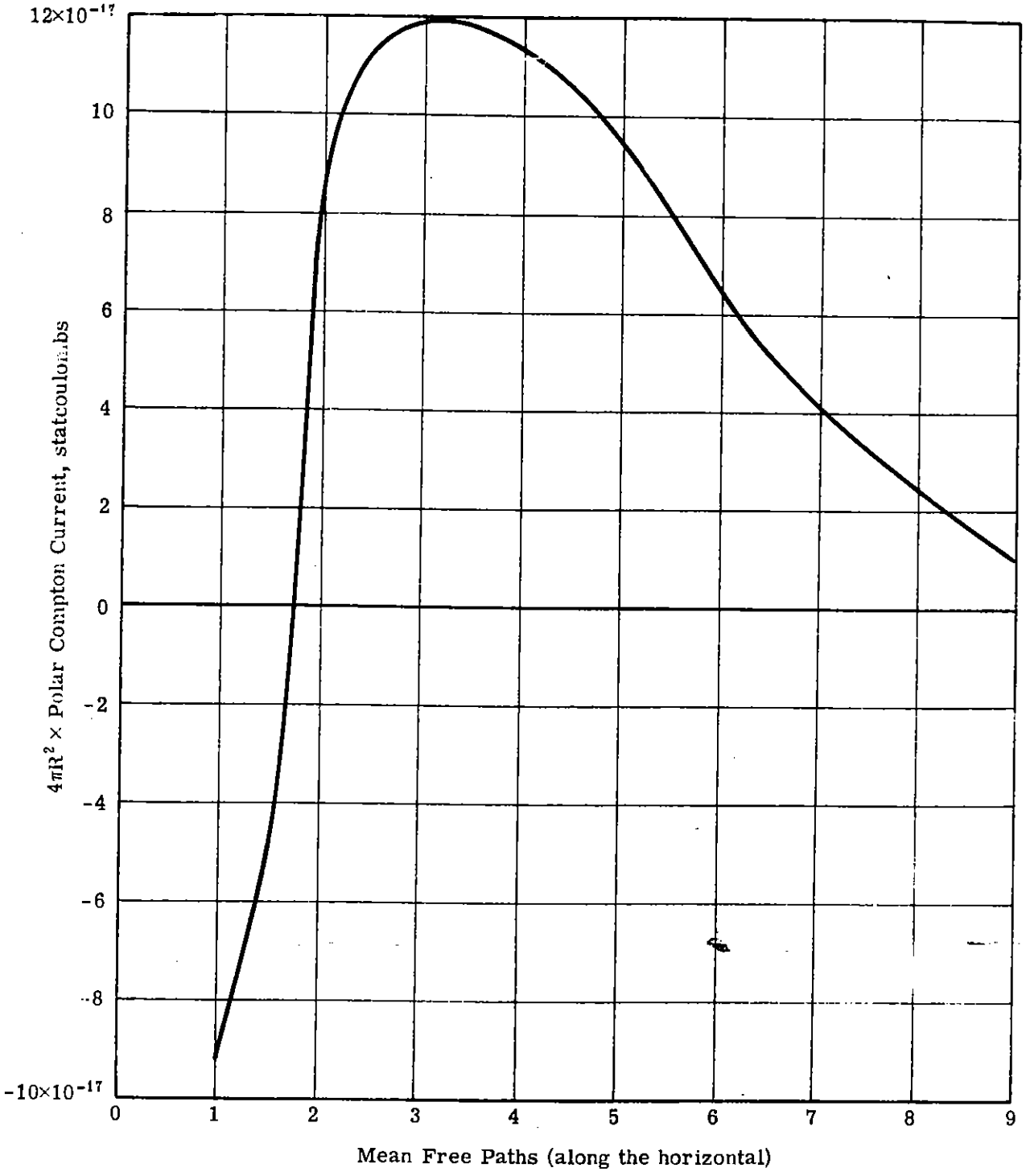

Fig. 26 — Polar Compton Current vs Source-Detector Penetration along the Horizontal (500-kev photons at 15,000 ft)

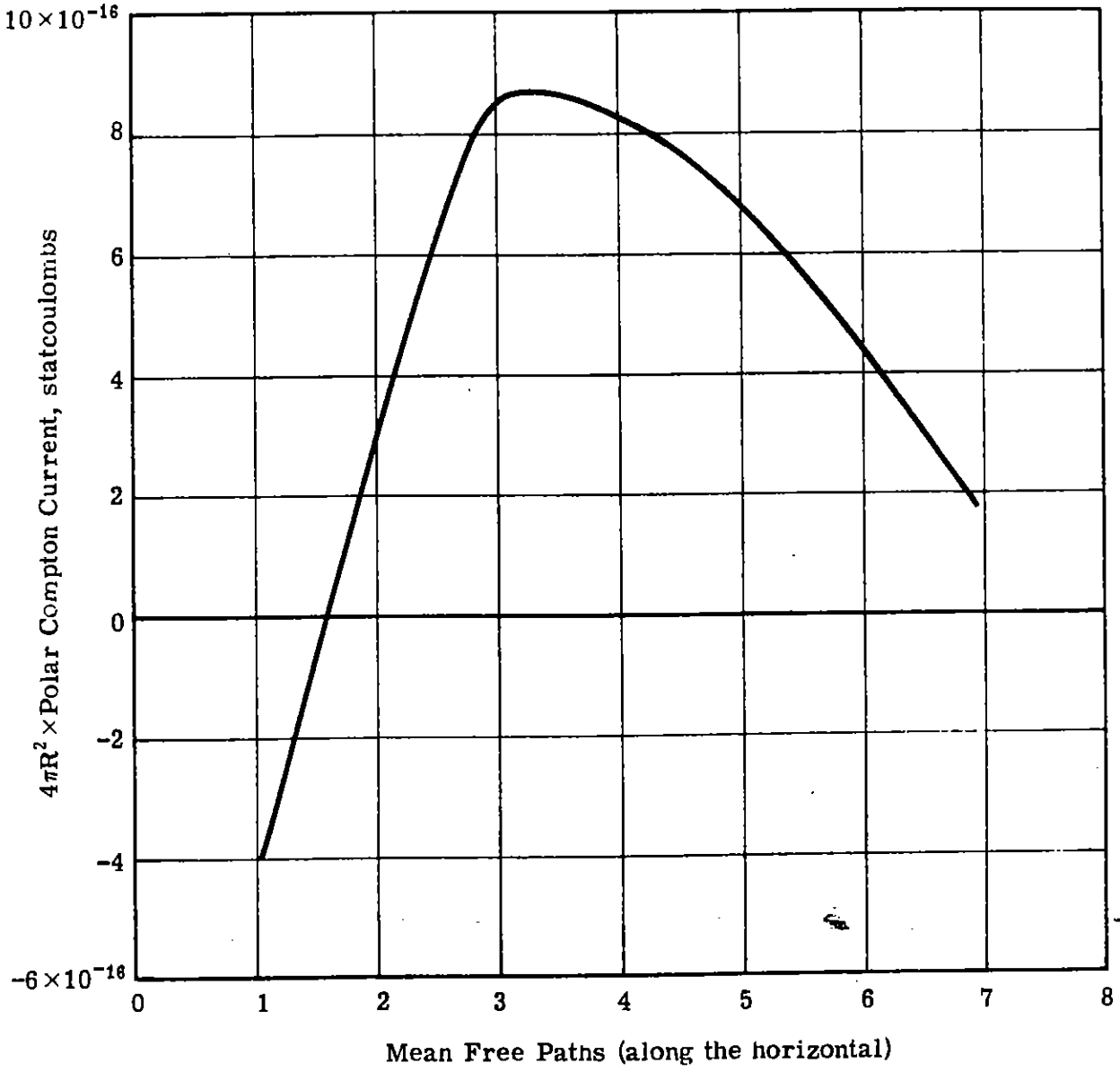

Fig. 27 — Polar Compton Current vs Source-Detector Penetration along the Horizontal (5-Mev photons at 15,000 ft)

Fig. 28 displays the ratio of the time-integrated polar current to radial current, for the three sources, as a function of penetration in mean free paths. Several interesting relationships are revealed by examination of this figure.

First, the polar-to-radial current ratio is greater, over the entire range, for the 500-kev source at 15,000 ft than for the 5-Mev source at the same altitude. The explanation for this is that the differential scattering cross section is decidedly less forward peaked for photons in the 500-kev range than in the 5-Mev range. Hence, 500-kev photons have a considerably greater probability of large-angle scattering and are more likely to arrive at a detector location at a large angle to the radial direction.

Second, the polar-to-radial current ratio is considerably greater for the 500-kev source at 50,000 ft than at 15,000 ft. This is because the atmospheric density varies much faster with changes in altitude at 50,000 ft than it does at 15,000 ft. Thus polar effects are magnified at this higher altitude.

Finally, it is noted that even for the 500-kev source at 50,000 ft (for which the calculated polar-to-radial ratios are the greatest), the polar-to-radial ratio at penetrations less than 2 mfp never greatly exceeds 10^{-3}. It thus appears from Fig. 28 that polar currents are probably not important, for the source energies and altitudes reported here, for penetrations less than 3 mfp. Beyond this penetration, the ratios rise to the 10^{-2} to 10^{-1} range where polar currents indeed may be significant.

Time-Dependent Polar Currents

The time dependencies of polar currents were found to be complex functions of source energy, source altitude, and source-detector orientation. The statistical accuracy of the Monte Carlo time-dependent polar current data was not sufficiently high to determine whether any of the above functional dependencies could be

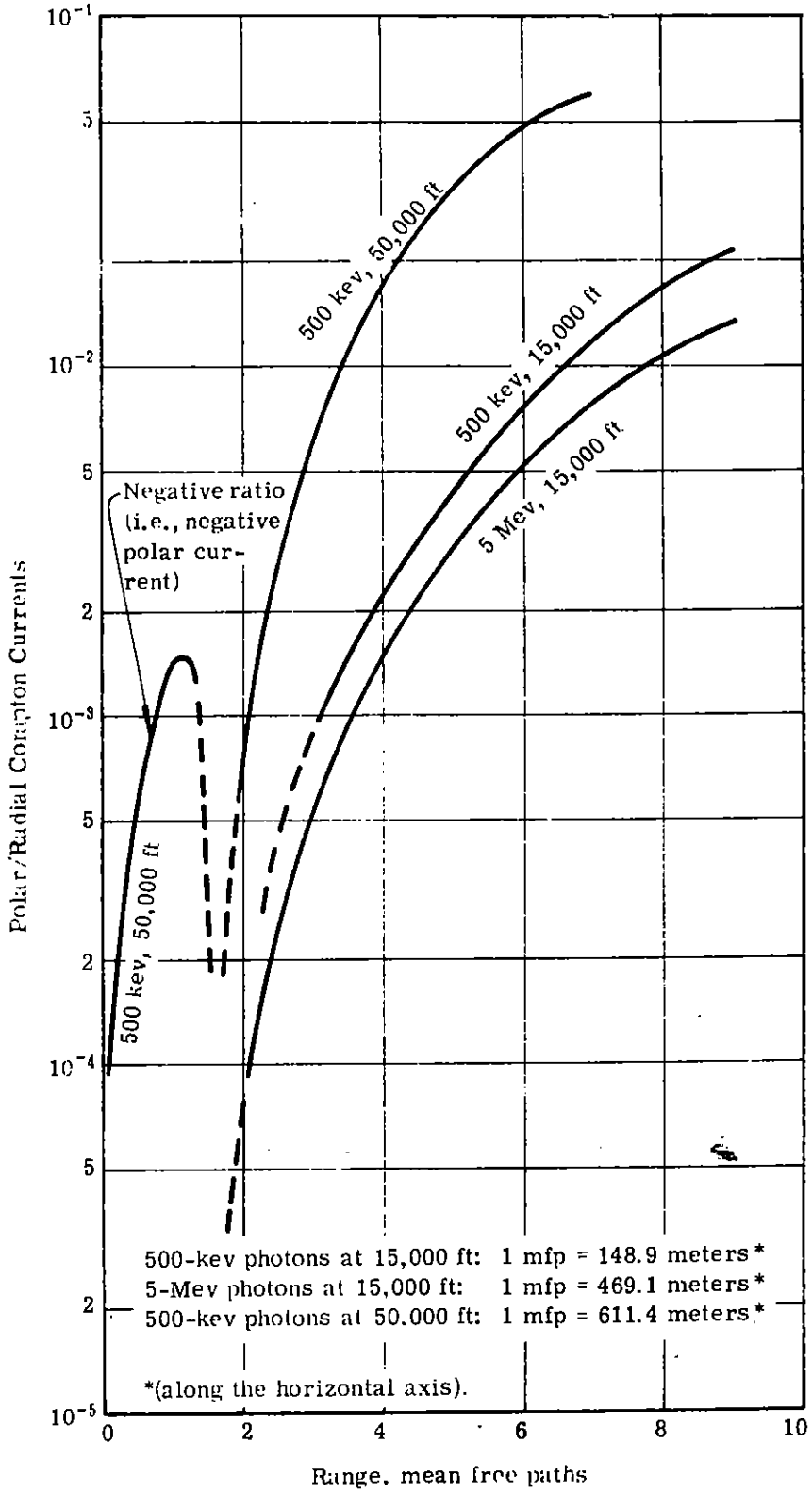

Fig. 28 — Ratio of Time-Integrated Polar-to-Radial Compton Currents (Coaltitude Photon Sources and Detectors)

separated out. For penetrations beyond 3 mfp (where polar currents are more likely to be appreciable) and for temporal ranges other than the very smallest, it appears that a simple exponential relationship may exist between polar currents and time. However, the two parameters associated with a simple exponential (i.e., the normalization and decay constants) do not appear to exhibit any simple functional relationship, and more accurate and detailed data are required before any complete relationship can be established.

Figs. 29 through 44 display the time-dependent polar Compton currents, normalized to the uncollided radial current, at various penetrations from the three sources.

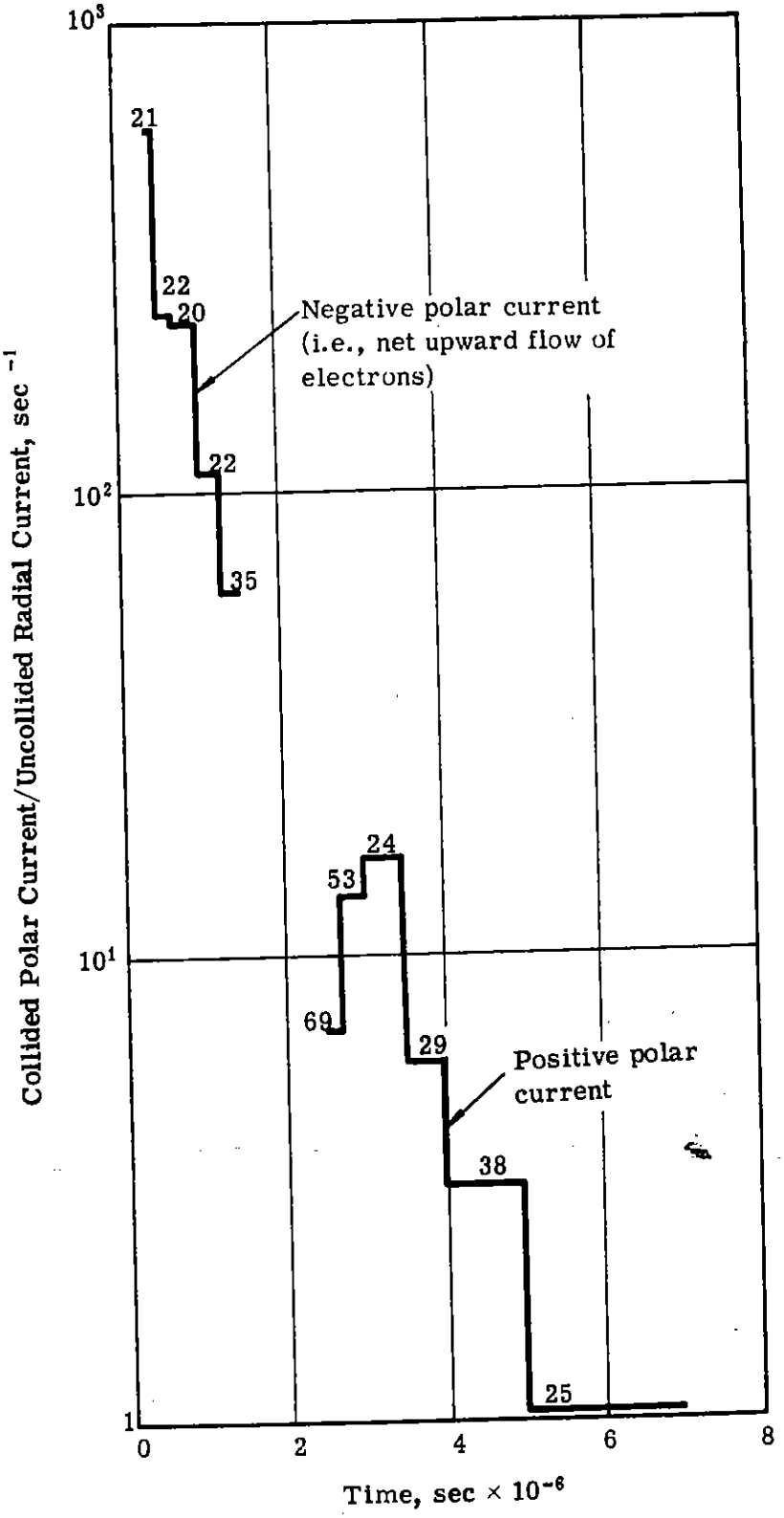

Fig. 29 — Polar Compton Current [Source: 500-kev photons at 15,000 ft; Detector: 15,000 ft, 1 mfp (148.9 meters)]

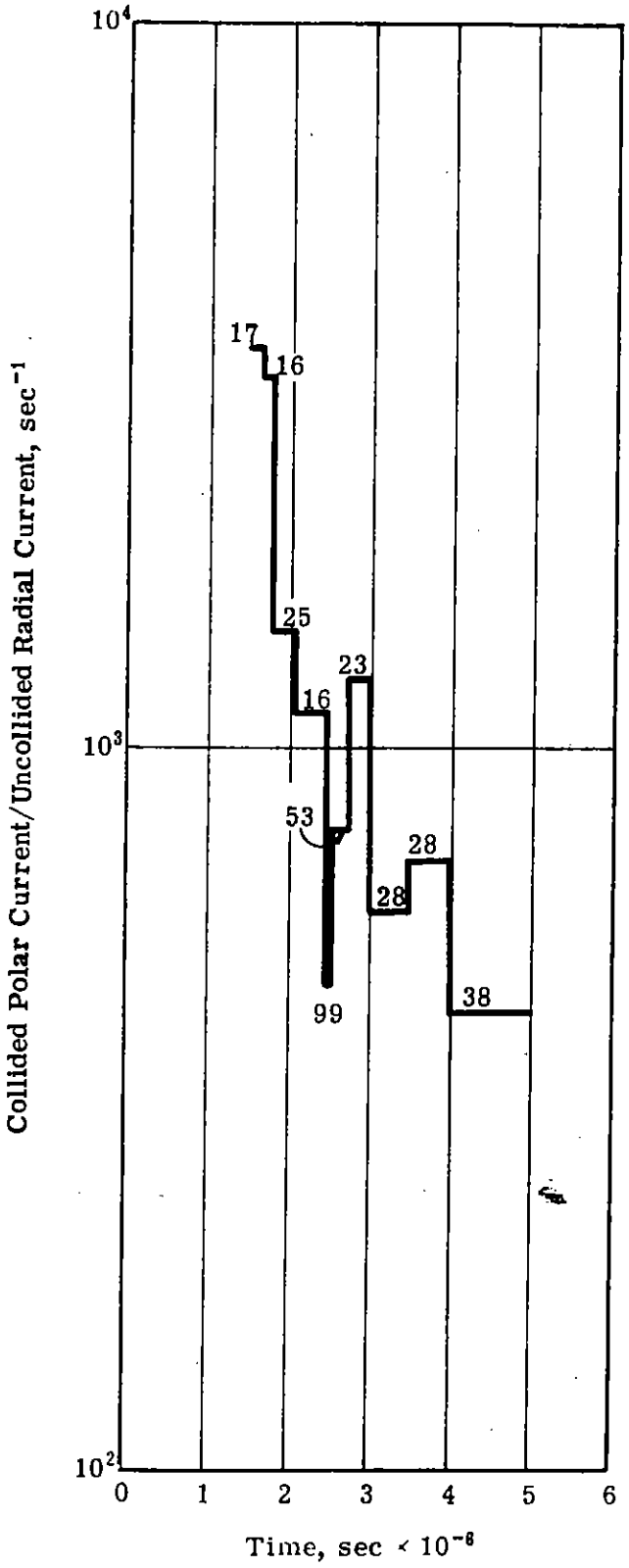

Fig. 30 — Polar Compton Current [Source: 500-kev photons at 15,000 ft; Detector: 15,000 ft, 3 mfp (446.7 meters)]

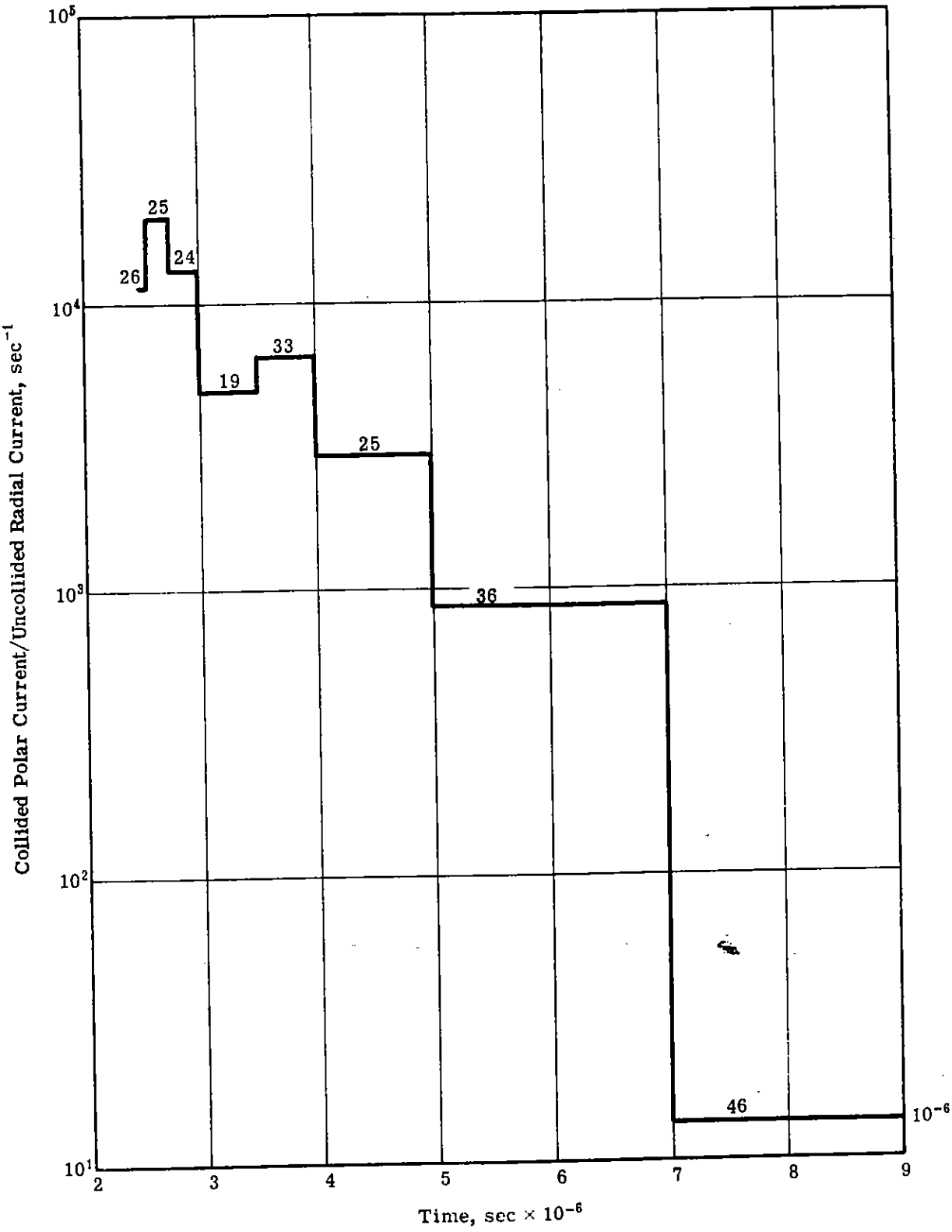

Fig. 31 — Polar Compton Current [Source: 500-kev photons at 15,000 ft; Detector: 15,000 ft, 5 mfp (744.5 meters)]

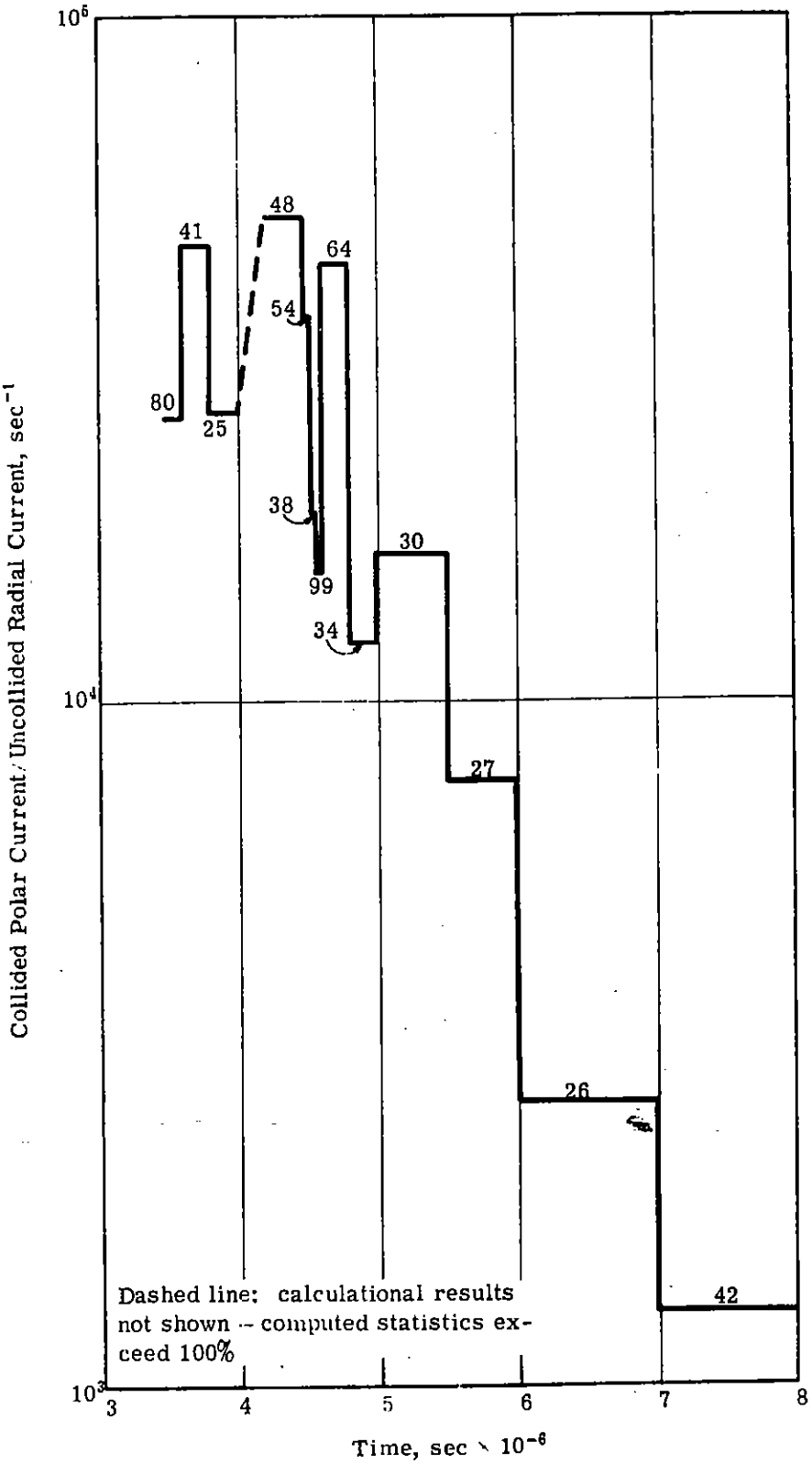

Fig. 32 — Polar Compton Current [Source: 500-kev photons at 15,000 ft; Detector: 15,000 ft, 7 mfp (1042.0 meters)]

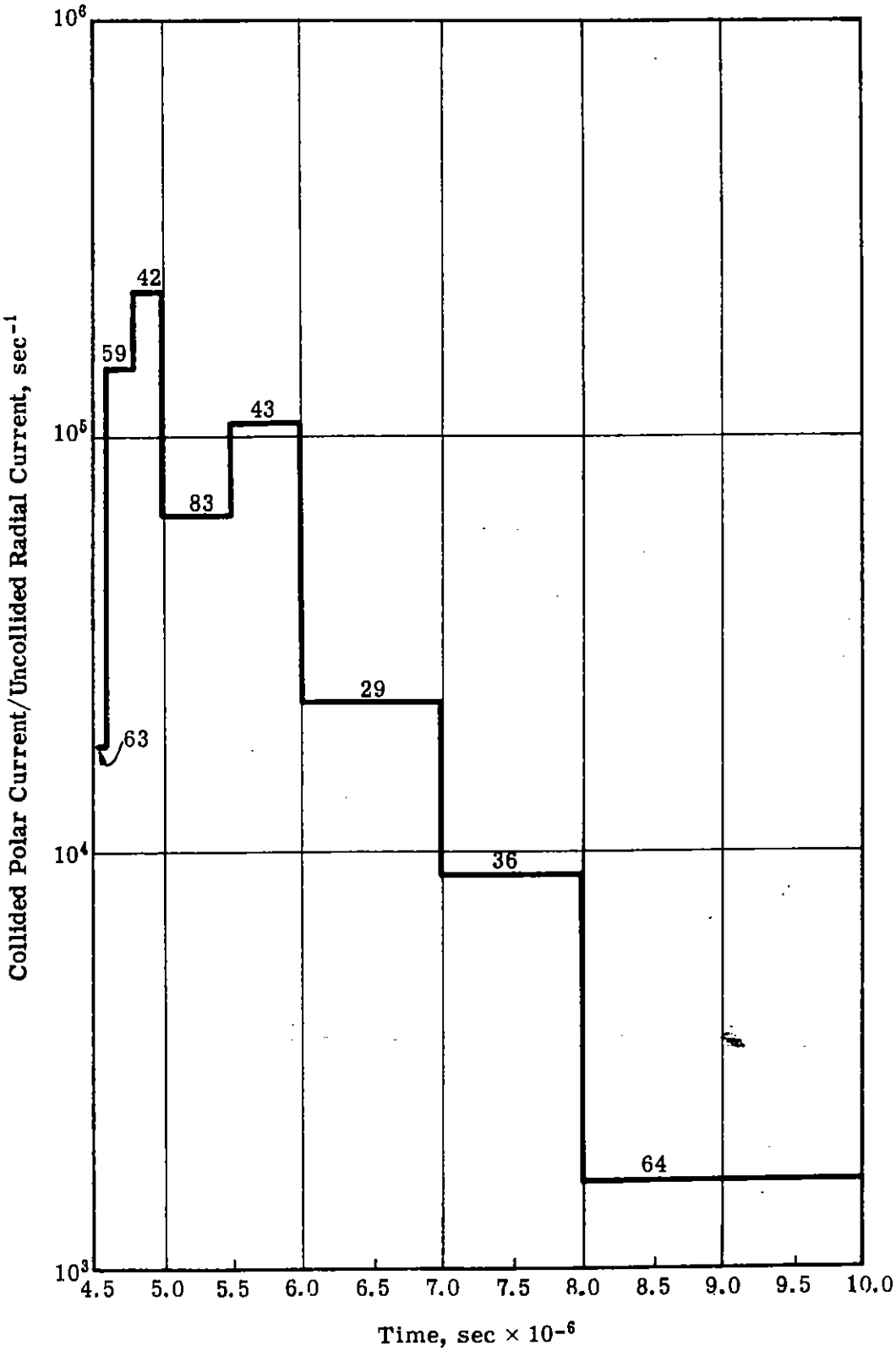

Fig. 33 — Polar Compton Current [Source: 500-kev photons at 15,000 ft; Detector: 15,000 ft, 9 mfp (1340.0 meters)]

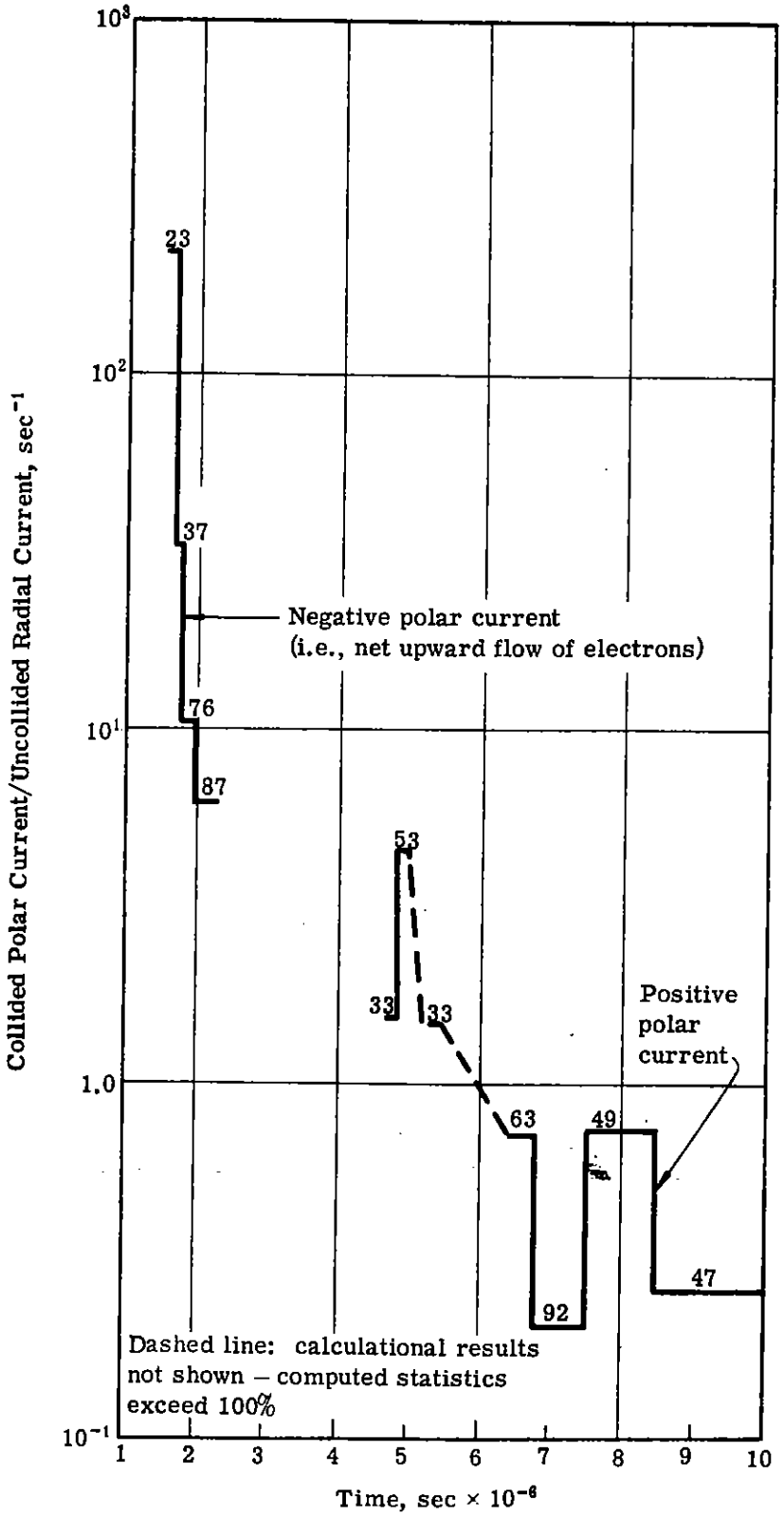

Fig. 34 — Polar Compton Current [Source: 5-Mev photons at 15,000 ft; Detector: 15,000 ft, 1 mfp (469.1 meters)]

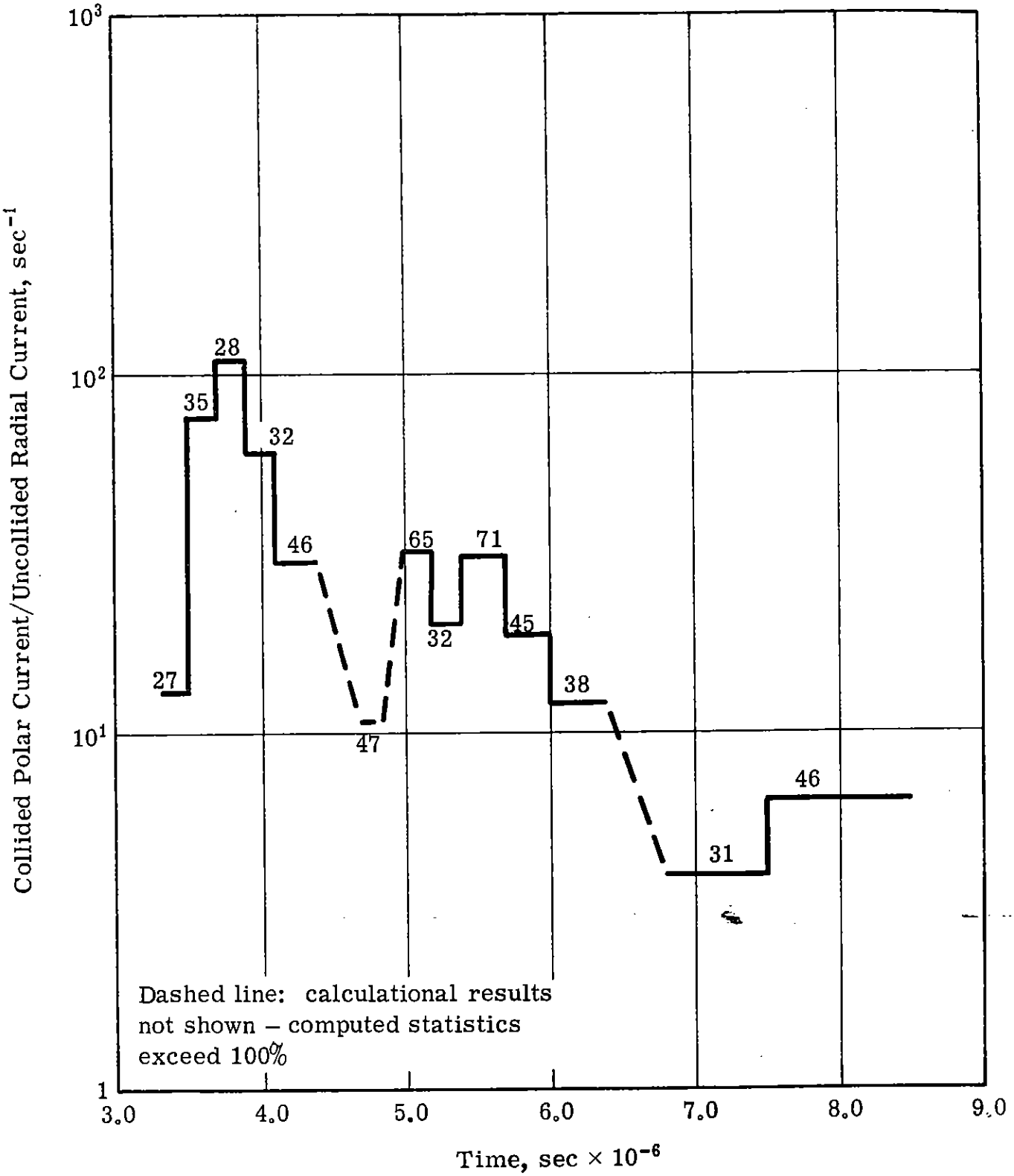

Fig. 35 — Polar Compton Current [Source: 5-Mev photons at 15,000 ft; Detector: 15,000 ft, 2 mfp (938.2 meters)]

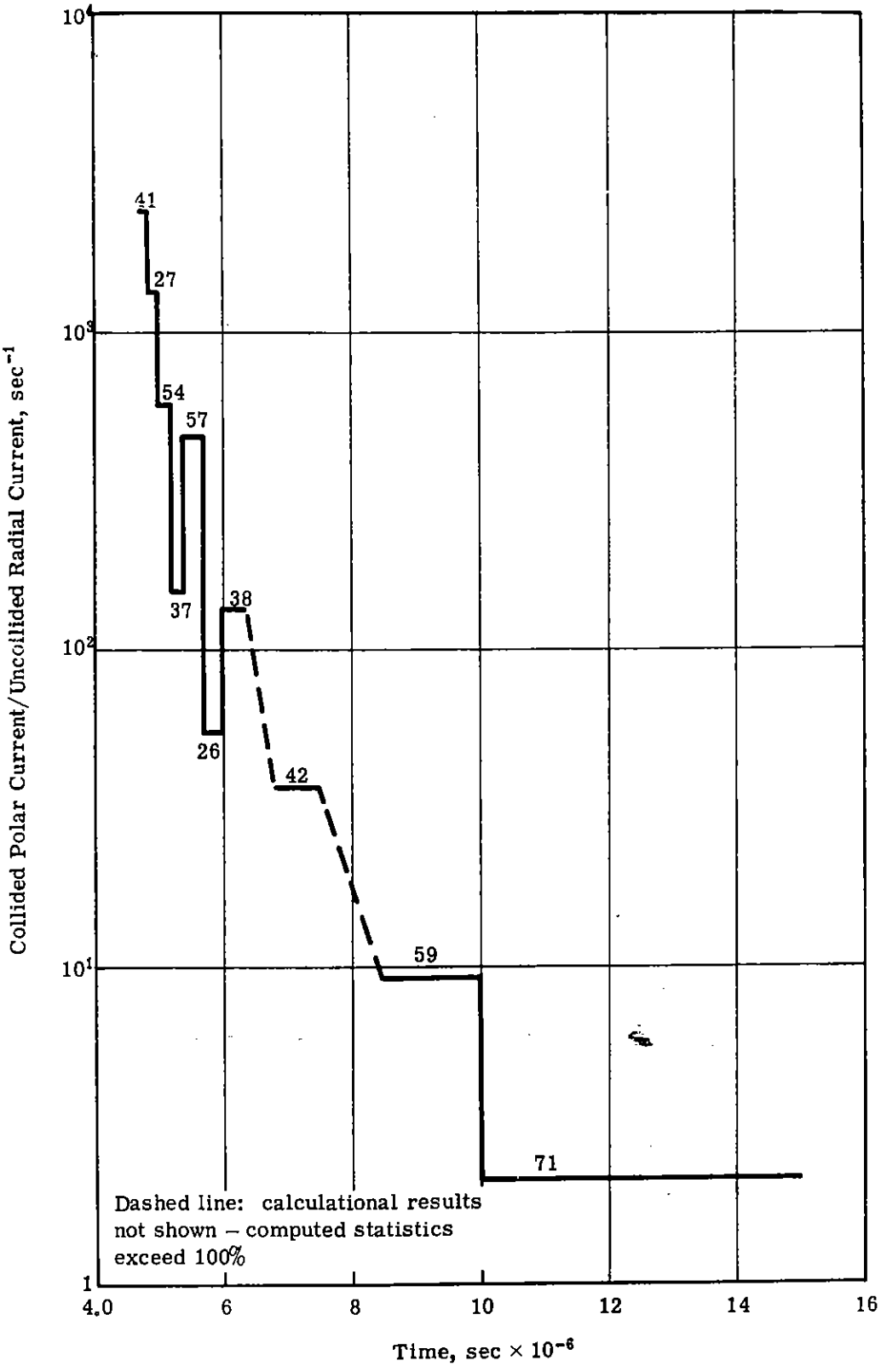

Fig. 36 — Polar Compton Current [Source: 5-Mev photons at 15,000 ft; Detector: 15,000 ft, 3 mfp (1407 meters)]

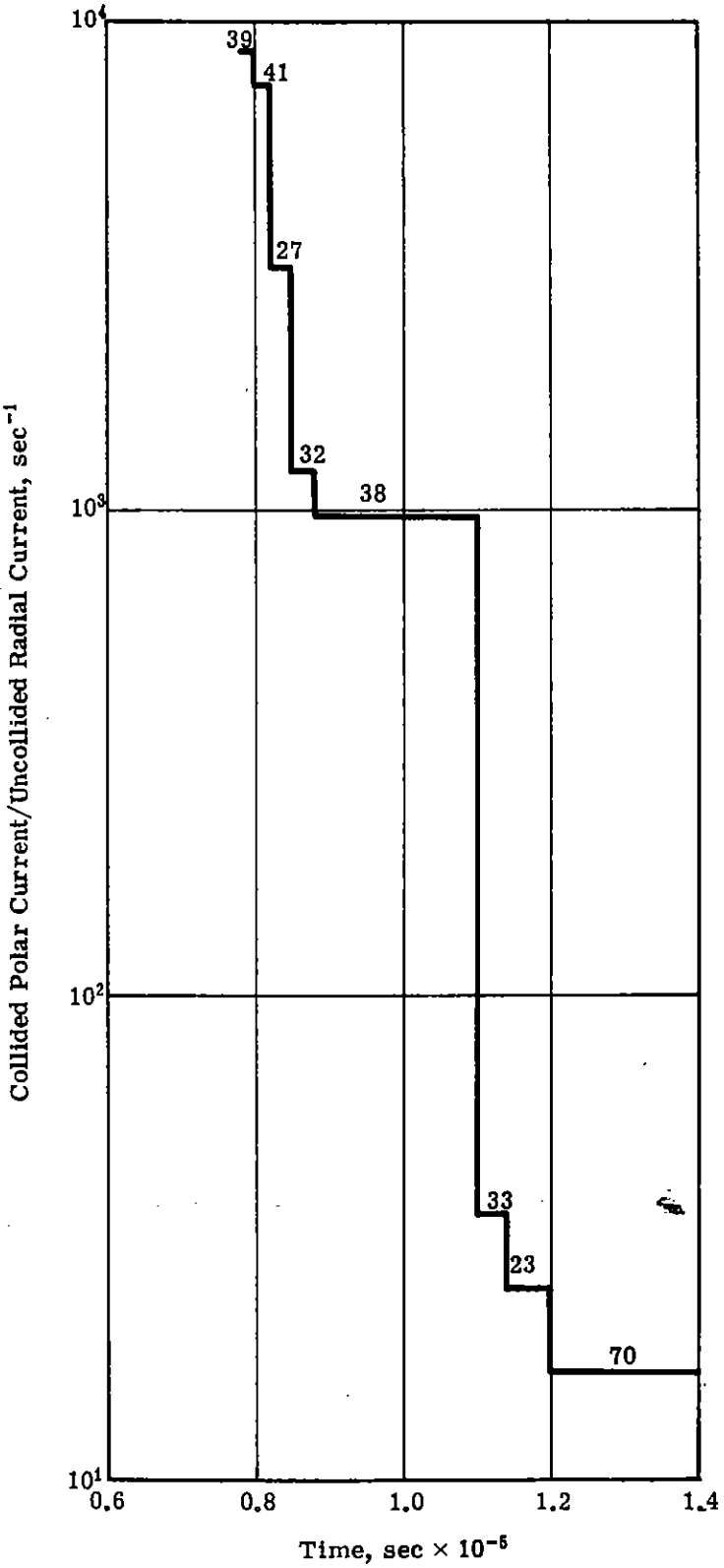

Fig. 37 — Polar Compton Current [Source: 5-Mev photons at 15,000 ft; Detector: 15,000 ft, 5 mfp (2346 meters)]

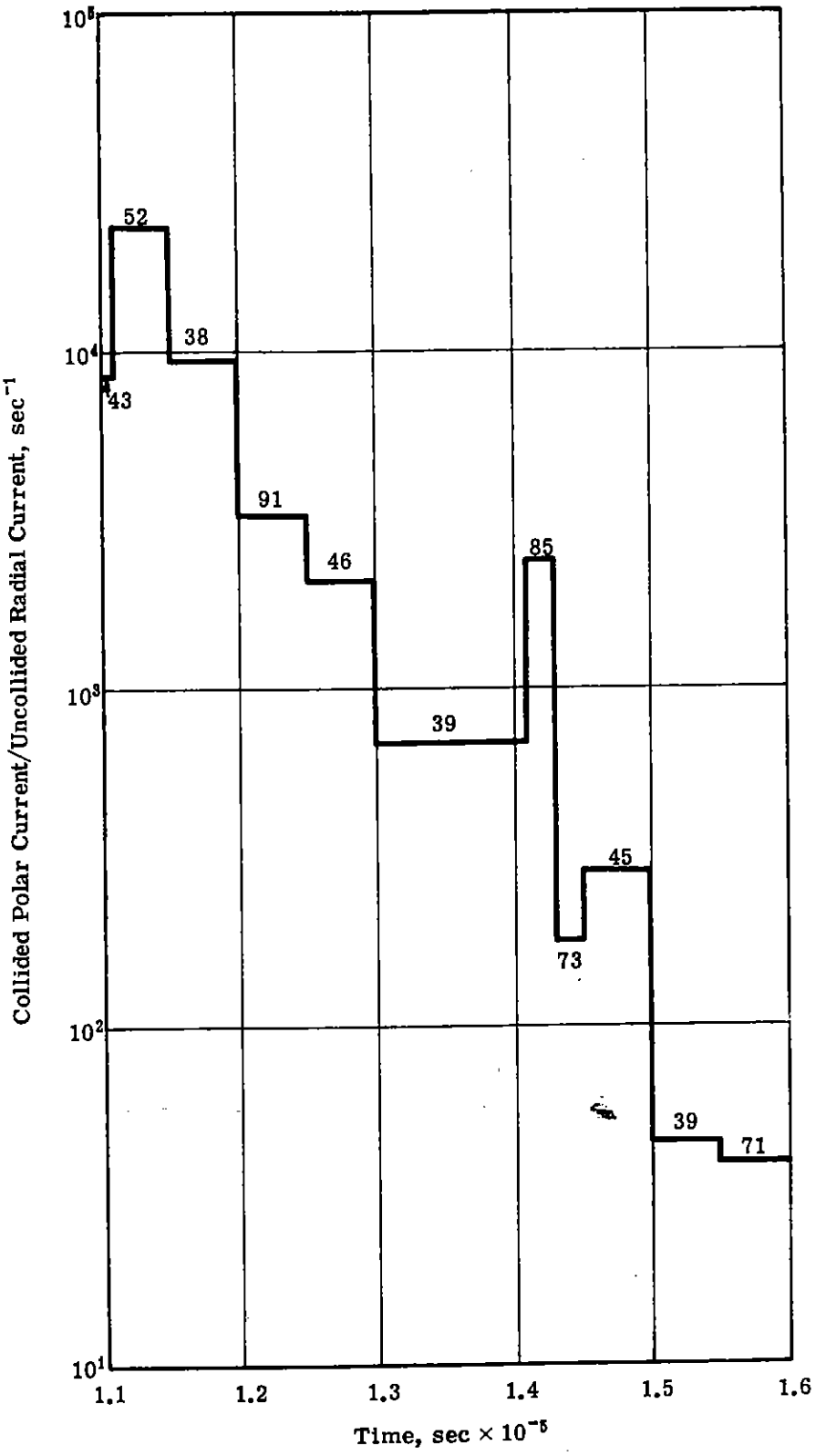

Fig. 38 — Polar Compton Current [Source: 5-Mev photons at 15,000 ft; Detector: 15,000 ft, 7 mfp (3284 meters)]

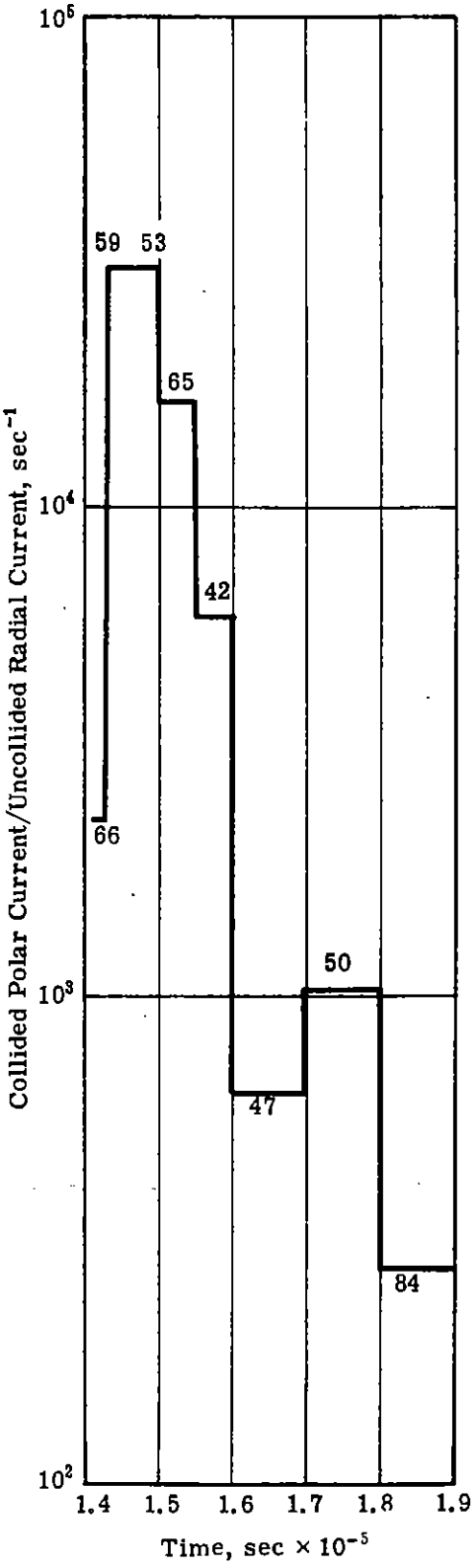

Fig. 39 — Polar Compton Current [Source: 5-Mev photons at 15,000 ft; Detector: 15,000 ft, 9 mfp (4222 meters)]

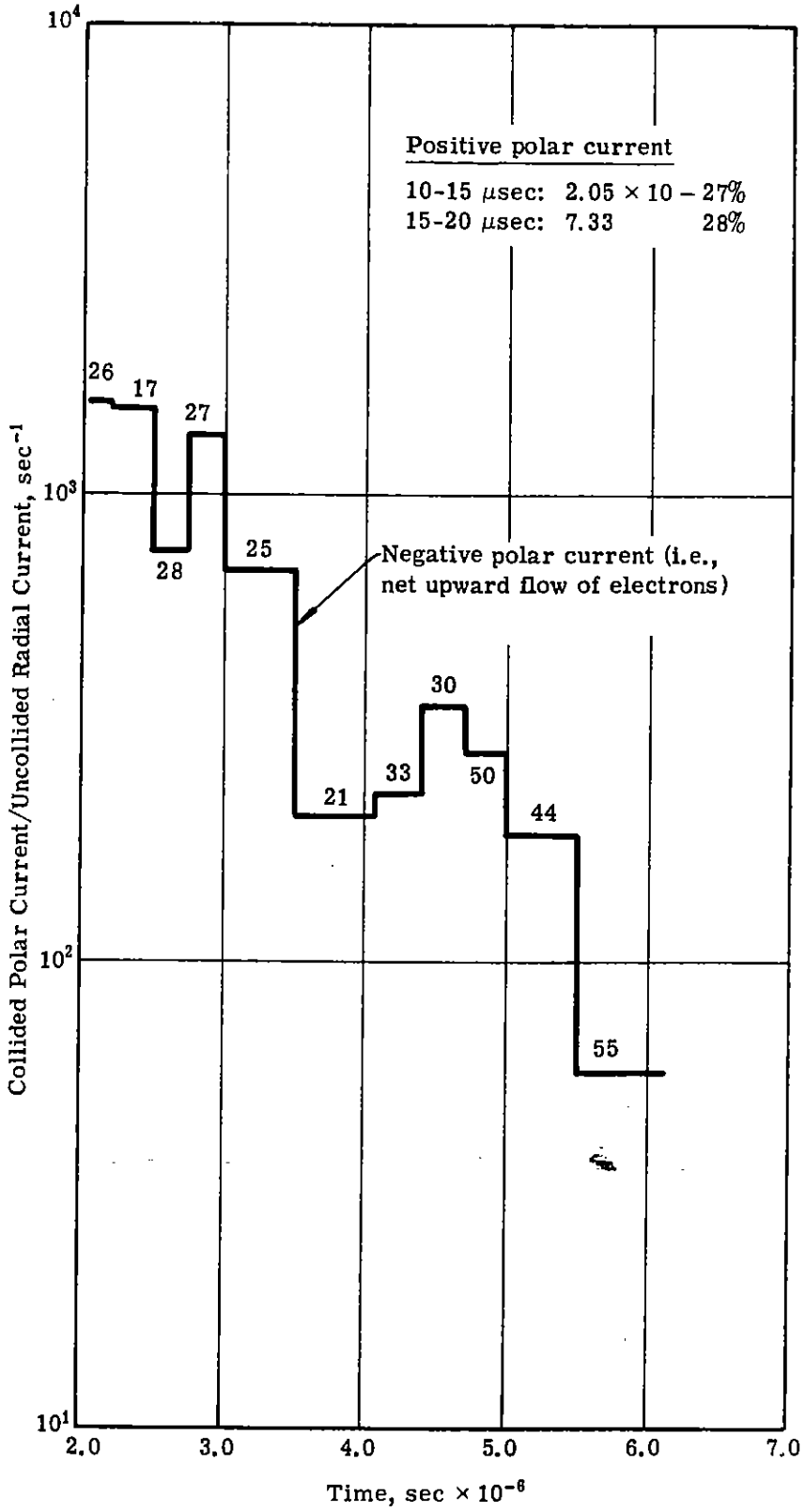

Fig. 40 — Polar Compton Current [Source: 500-kev photons at 50,000 ft; Detector: 50,000 ft, 1 mfp (611.4 meters)]

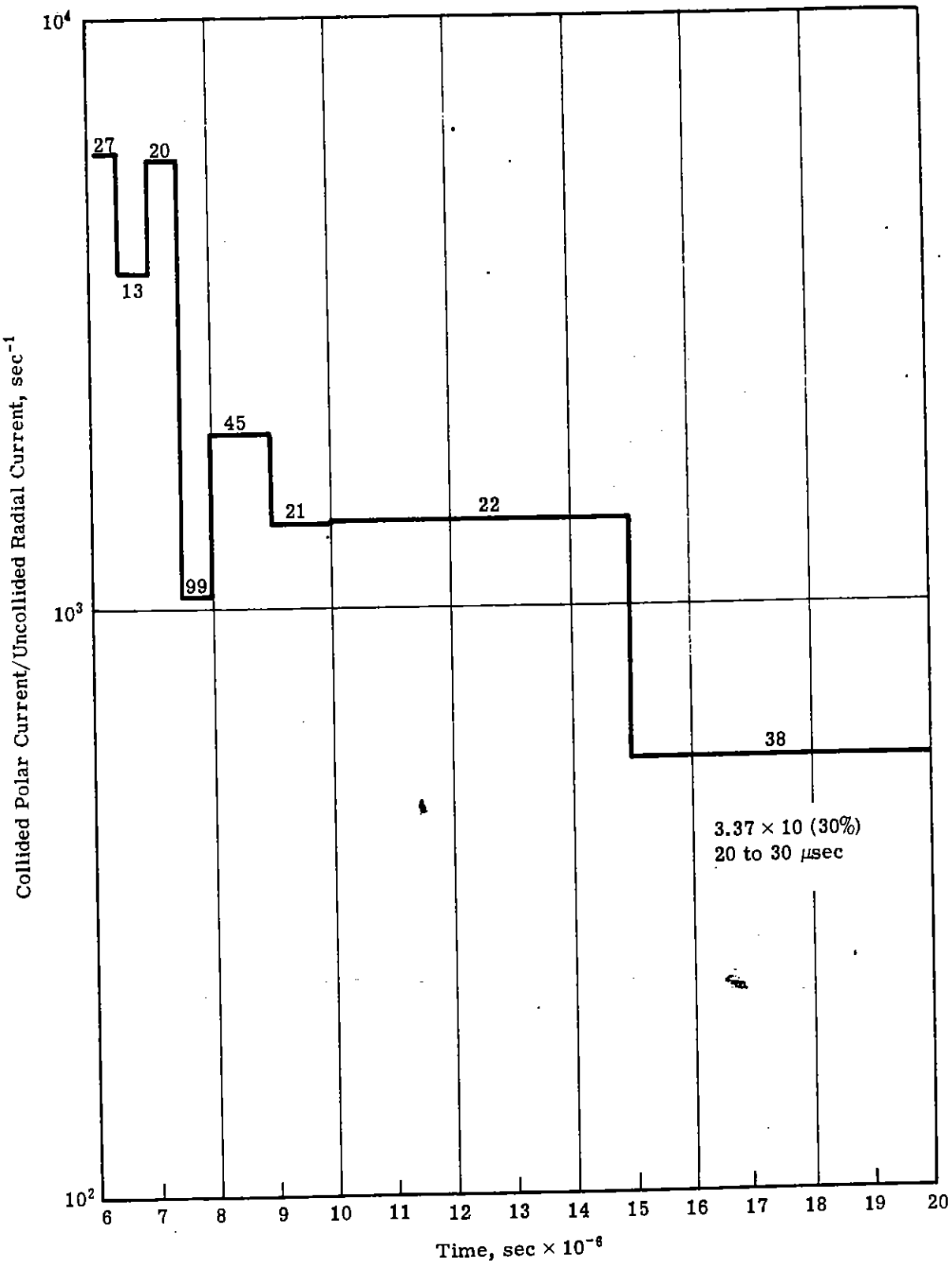

Fig. 41 — Polar Compton Current [Source: 500-kev photons at 50,000 ft; Detector: 50,000 ft, 3 mfp (1834 meters)]

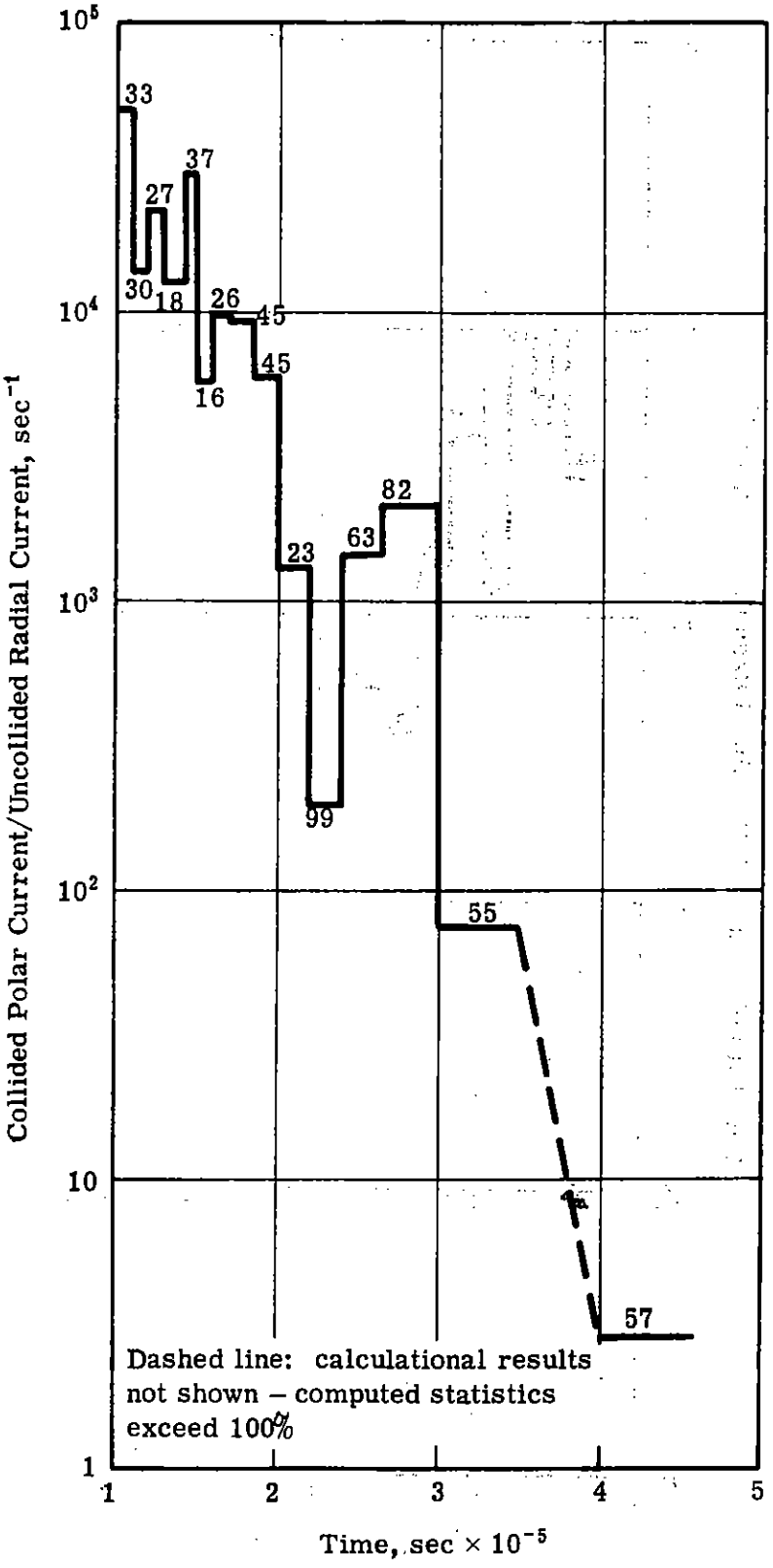

Fig. 42 — Polar Compton Current [Source: 500-kev photons at 50,000 ft; Detector: 50,000 ft, 5 mfp (3057 meters)]

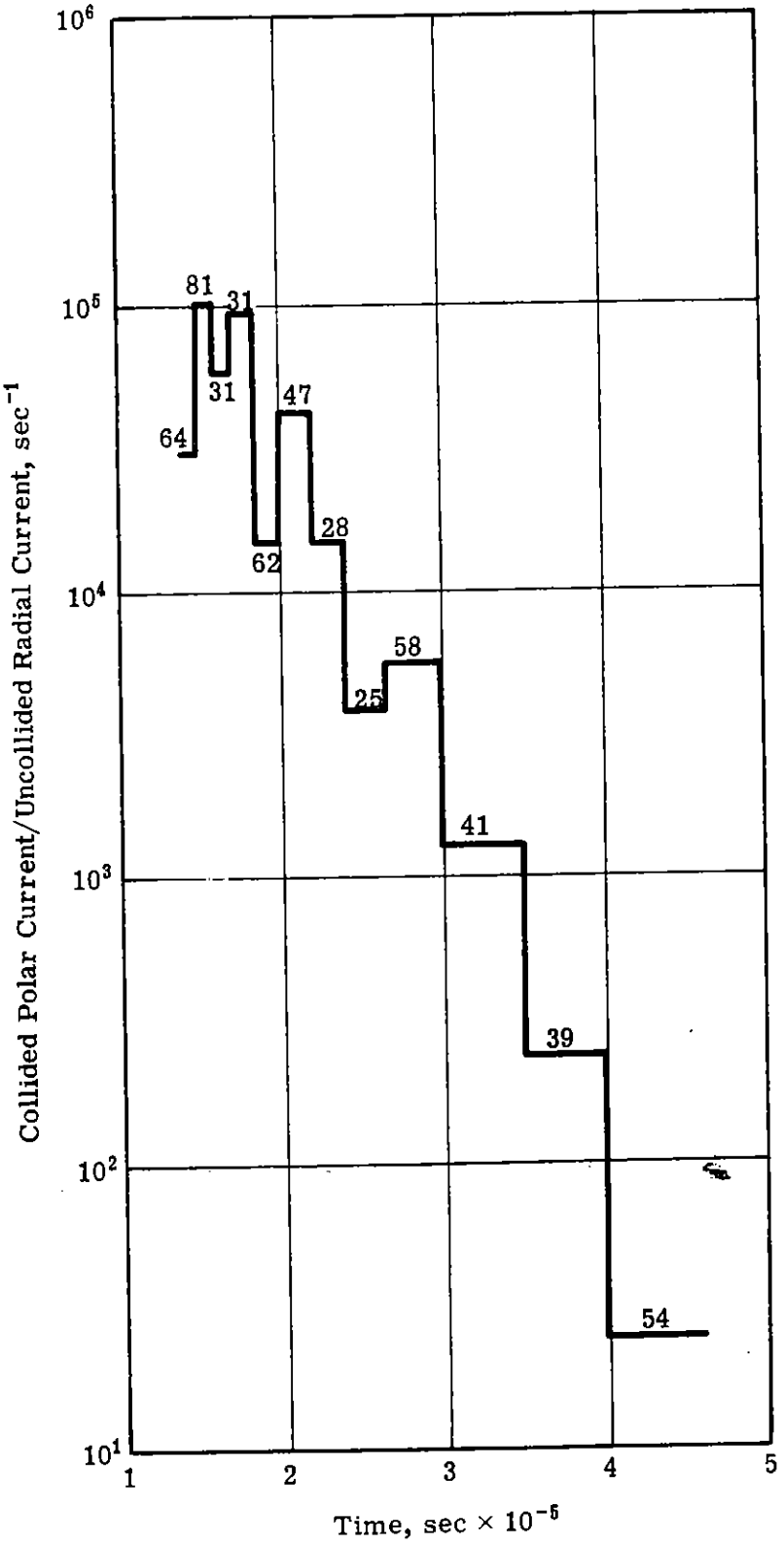

Fig. 43 — Polar Compton Current [Source: 500-kev photons at 50,000 ft; Detector: 50,000 ft, 7 mfp (4280 meters)]

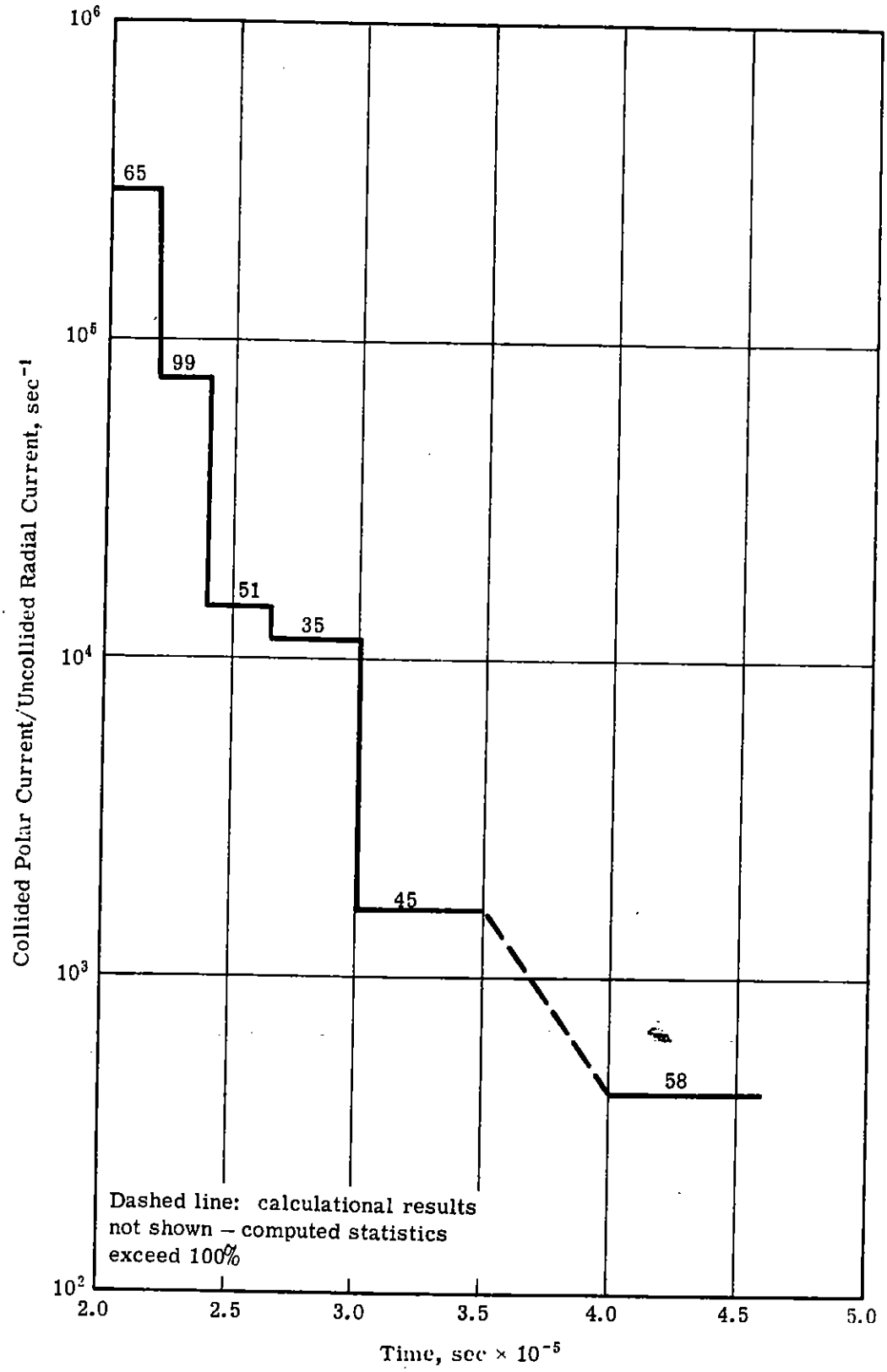

Fig. 44 — Polar Compton Current [Source: 500-kev photons at 50,000 ft; Detector: 50,000 ft, 9 mfp (5502 meters)]

SECTION V

RESULTS OF THE SECONDARY GAMMA RADIATION STUDIES

The effects of the secondary gamma radiation proved to be more difficult to ascertain than had been anticipated. Apparently, the nature of the neutron and secondary gamma-ray transport is such that CORSAIR does not obtain adequate time-dependent results for the number of histories which can be tracked using reasonable amounts of CDC-1604-A computer time (i.e., approximately 20 minutes per detector per 5000 histories – see Appendix F). Calculations of this magnitude are sufficient to provide meaningful time-integrated energy deposition and Compton current results, but it is estimated that it is necessary to track at least 125,000 to 750,000 histories to obtain adequate detailed information on the time dependence.

TIME-INTEGRATED RESULTS

Source Altitude of 15,000 ft

Both the dose and radial currents at detector locations surrounding the 14-Mev source at 15,000 ft were found to be independent of source-detector orientation provided they are expressed in units multiplied by $4\pi R^2$ and the penetrations are expressed in units of g/cm^2. This is the same scaling which has been determined to be applicable to the primary gamma-ray sources. This scaling technique is expected to be valid for lower energy neutron sources at 15,000 ft, since the gamma radiation fields which they produce extend over a smaller spatial range and thus experience smaller variations in atmospheric density. A test

problem for 5-Mev neutrons yielded results that confirmed this expectation. Hence, all results for the time-integrated dose and radial currents are presented for one source-detector orientation (i.e., coaltitude source and detectors), and these may be scaled to other orientations as indicated above.

Figs. 45 and 46 display the time-integrated secondary gamma-ray doses and radial currents, respectively, from the four neutron sources at 15,000 ft. In both figures, smooth relationships are obtained between dose (or radial currents) and range. It is felt that the results at 5, 7, 10, and 14 Mev can be cross-plotted to obtain, with a sufficient degree of accuracy, dose and radial currents corresponding to any source neutron energy from 5 to 14 Mev.

Fig. 47 displays the time-integrated ratio of polar-to-radial currents at detectors coaltitude to the four primary neutron sources at 15,000 ft. These results also can be cross-plotted to obtain polar currents at detectors coaltitude to any neutron source at 15,000 ft in the energy range of 5 to 14 Mev. No attempt was made in this study to establish the dependency of the polar-to-radial ratio upon source-detector orientation.

The polar-to-radial current ratios for all four neutron sources at 15,000 ft appear to approach asymptotic values in the range 2×10^{-2} to 5×10^{-2}. If the results for the primary 500-kev and 5-Mev radiation at 15,000 ft are extrapolated to deeper penetrations (see Fig. 28), they also appear to have asymptotic values in this ratio range. It thus appears that the initial neutron transport has a limited effect upon the time-integrated polar-to-radial current ratios at deep penetrations. Of course, the neutron transport has profound effects upon the time scales of the time-dependent data.

Source Altitude at 50,000 ft

Secondary gamma-ray doses and radial currents were calculated at detector locations coaltitude to a 14-Mev neutron source at 50,000 ft to determine

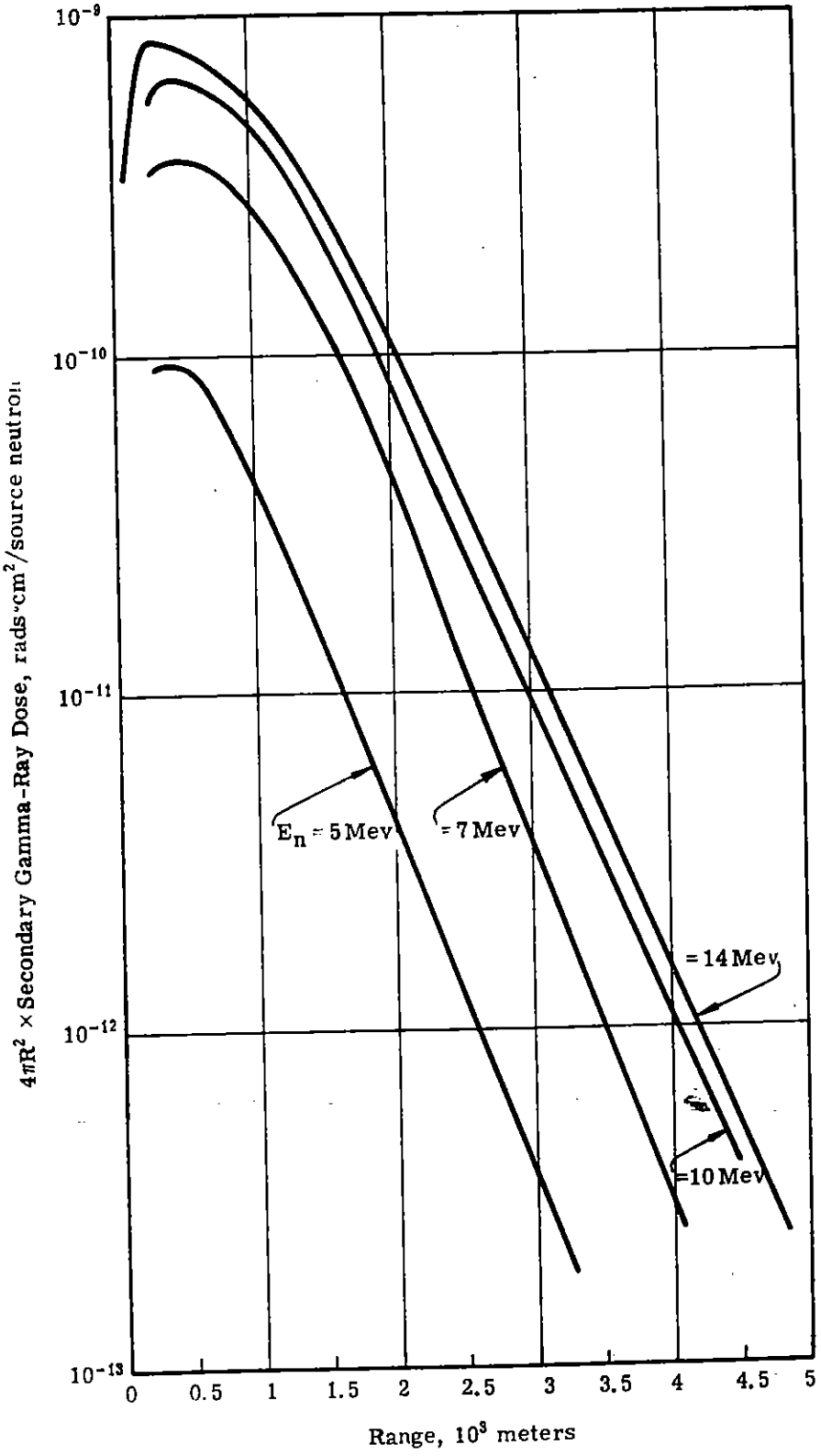

Fig. 45 — Secondary Gamma-Ray Dose (Sources and Detectors at 15,000 ft)

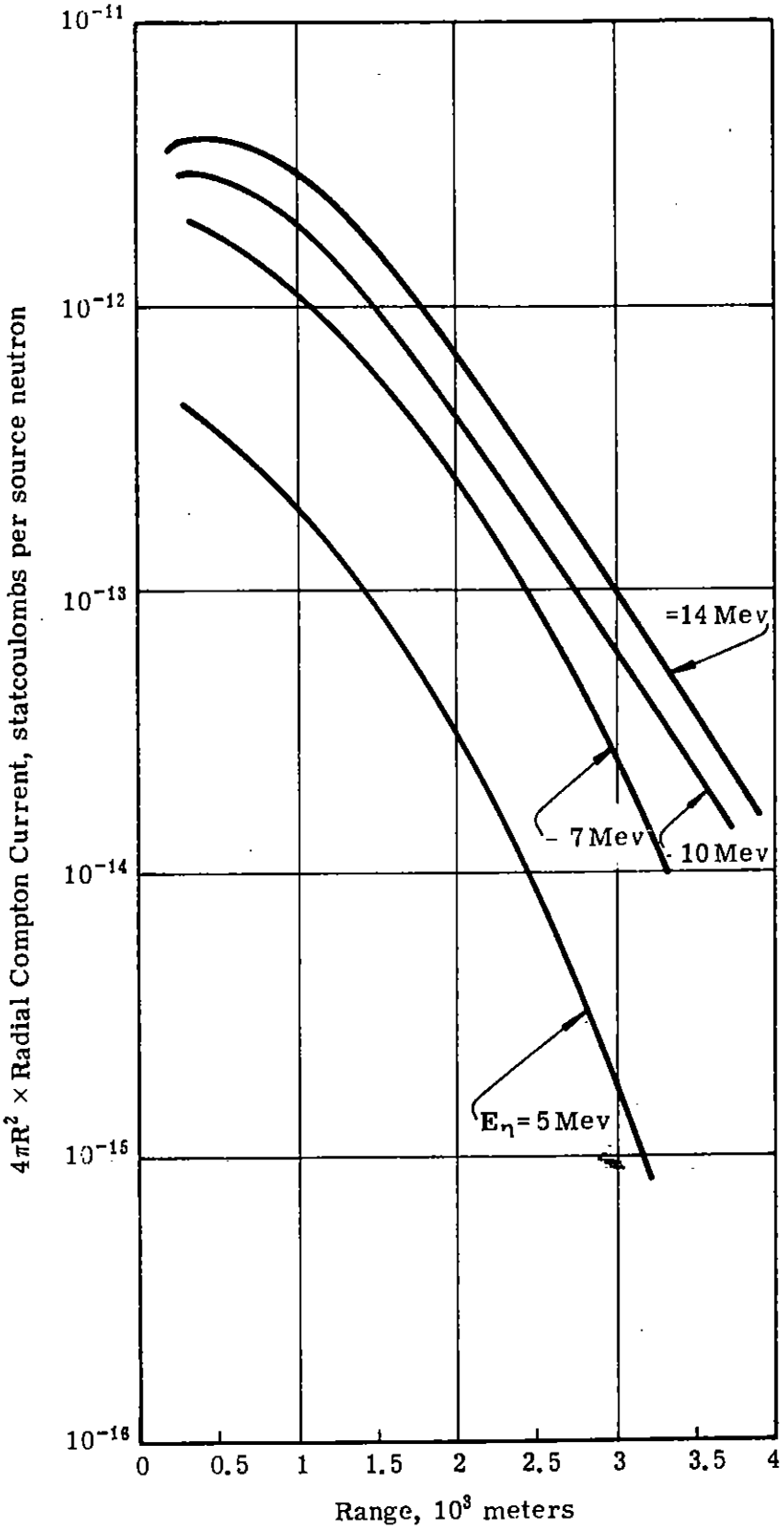

Fig. 46 — Radial Compton Current (Sources and Detectors at 15,000 ft)

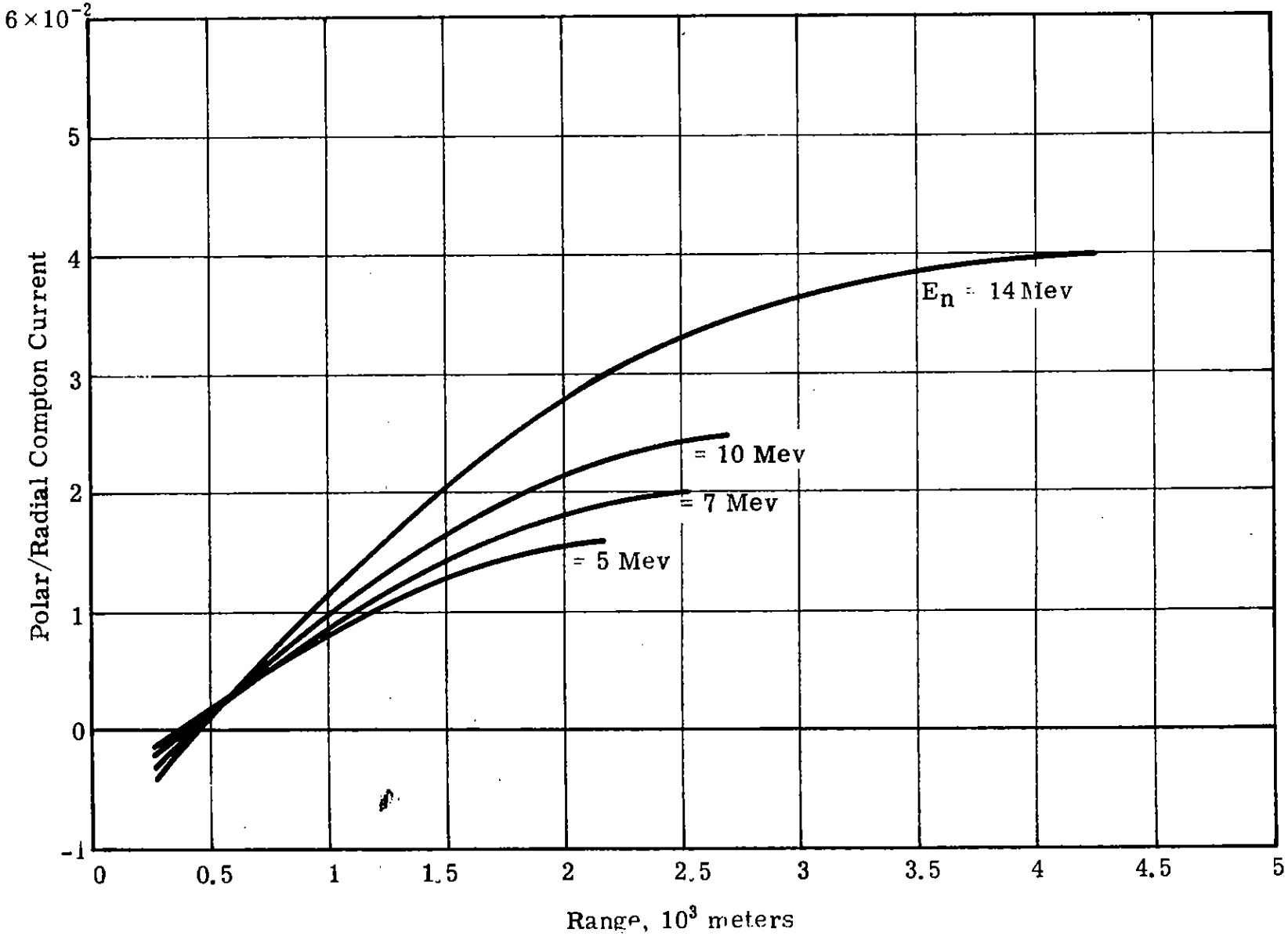

Fig. 47 — Ratio of Time-Integrated Polar-to-Radial Compton Currents (Coaltitude Neutron Sources and Detectors at 15,000 ft)

whether these quantities can be scaled with altitude in the 15,000 to 50,000-ft range. The 14-Mev source was selected for this study since it produces the secondary radiation field which is the most extensive in space and which thus experiences the largest variations in atmospheric density.

In Figs. 48 and 49, dose and radial current, respectively, from the 14-Mev neutron sources at 15,000 and 50,000 ft, multiplied by $4\pi R^2$, are plotted vs source-detector penetration in g/cm^2. In each case the solid curve represents the 15,000-ft source altitude data (from Figs. 45 and 46). The data obtained for a source altitude of 50,000 ft are plotted with vertical bars indicating the variance in the data. The results indicate that scaling with source altitude is possible for the neutron sources and altitudes of this study.

The same set of Monte Carlo calculations also indicated that the polar-to-radial current ratio is larger at 50,000 ft than at 15,000 ft. The ratio is greater than 0.1 at a detector located about 8 kilometers (158 g/cm^2) from, and coaltitude to, the source. However, the Monte Carlo statistical uncertainties in the polar current are of the order of 50% and more particle histories need to be followed before any quantitative conclusions are reached.

TIME-DEPENDENT RESULTS

The time-dependent data for the secondary gamma-ray dose rates and radial currents are insufficient to establish analytical expressions for these quantities. For example, Figs. 50, 51, and 52 display the calculated secondary gamma-ray dose rate as a function of real time at several coaltitude source-detector separations for a 7-Mev neutron source at an altitude of 15,000 ft. Figs. 53 through 56 display the radial Compton current as a function of real time from a 14-Mev neutron source. (Similar histograms of dose rate and radial current as functions of time at detectors surrounding the 14, 10, 7, and 5-Mev sources have been presented in detail in Reference 13.)

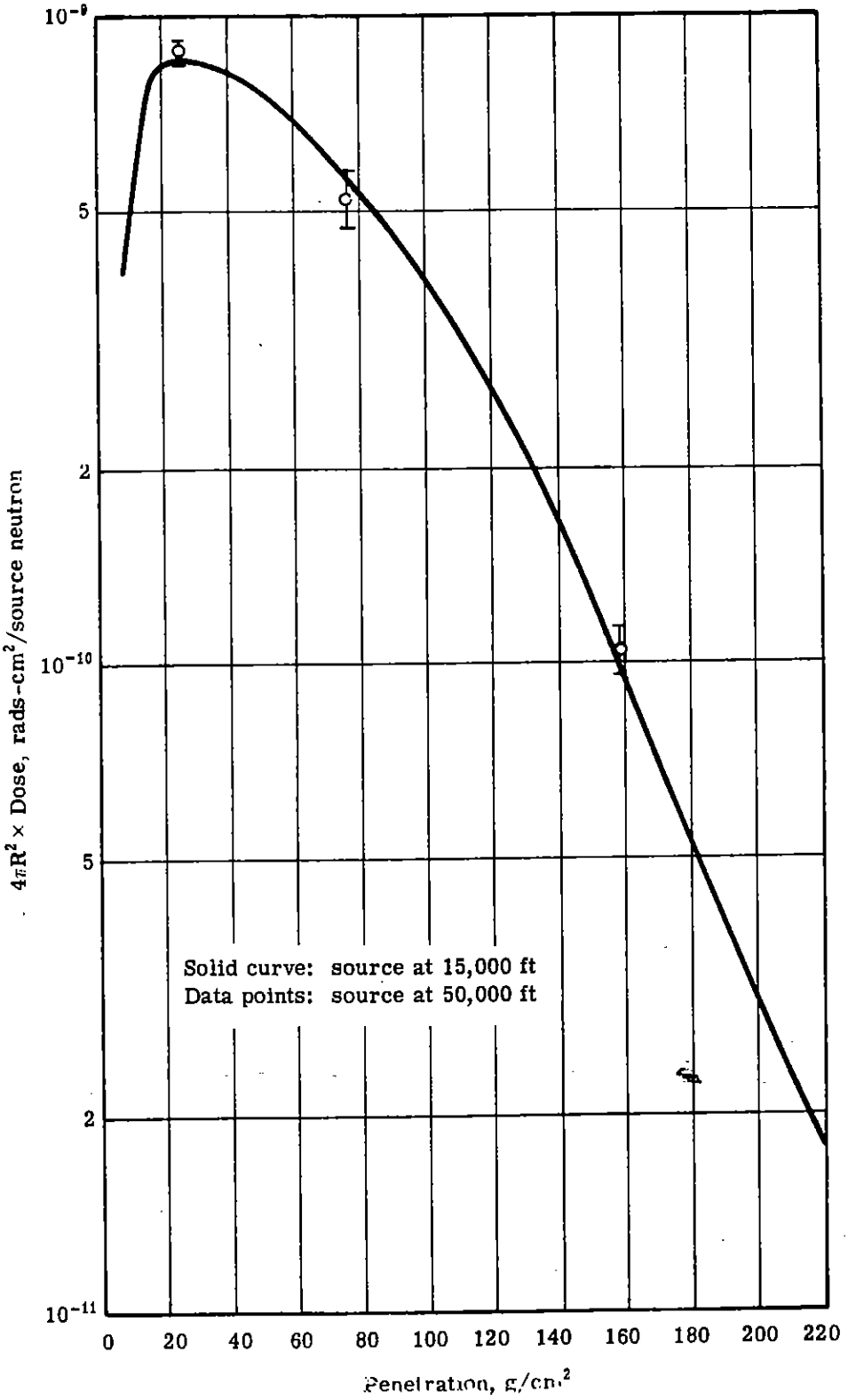

Fig. 48 — Secondary Gamma-Ray Dose (from 14-Mev Neutrons) vs Penetration

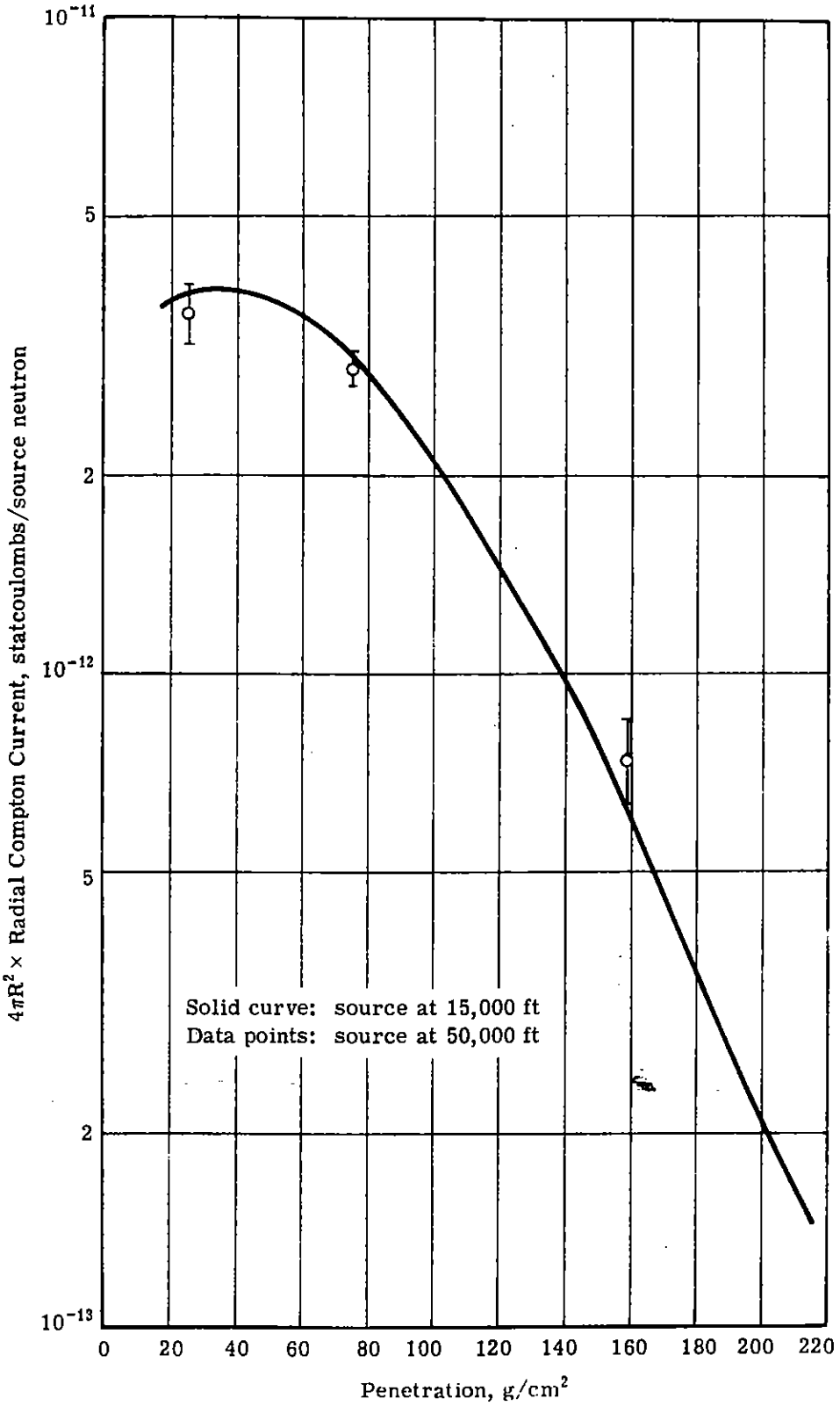

Fig. 49 — Radial Compton Current (from 14-Mev Neutrons) vs Penetration

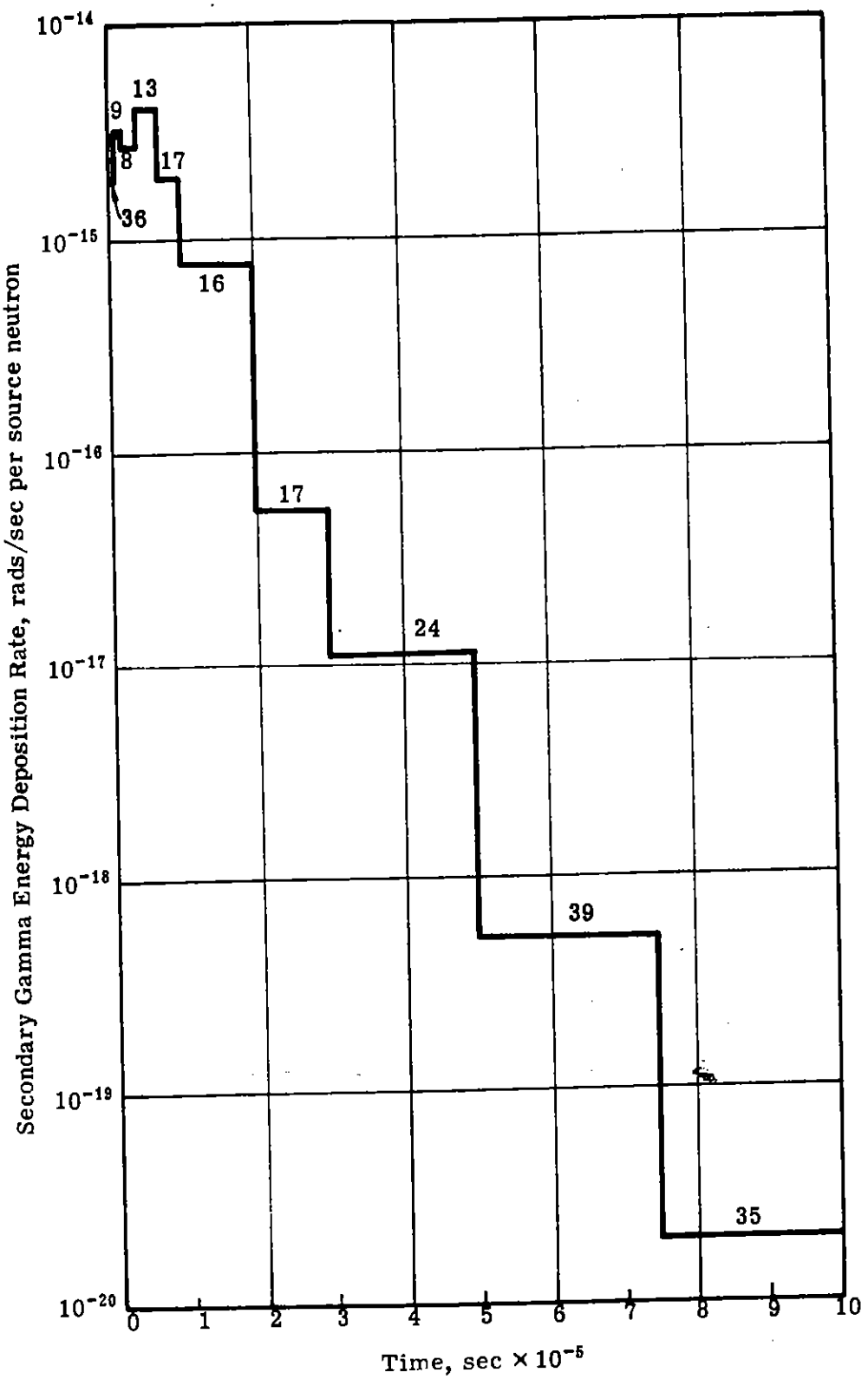

Fig. 50 — Secondary Gamma Energy Deposition Rate (Source: 7-Mev neutrons at 15,000 ft; Detector: 15,000 ft; Source to Detector: 270 meters)

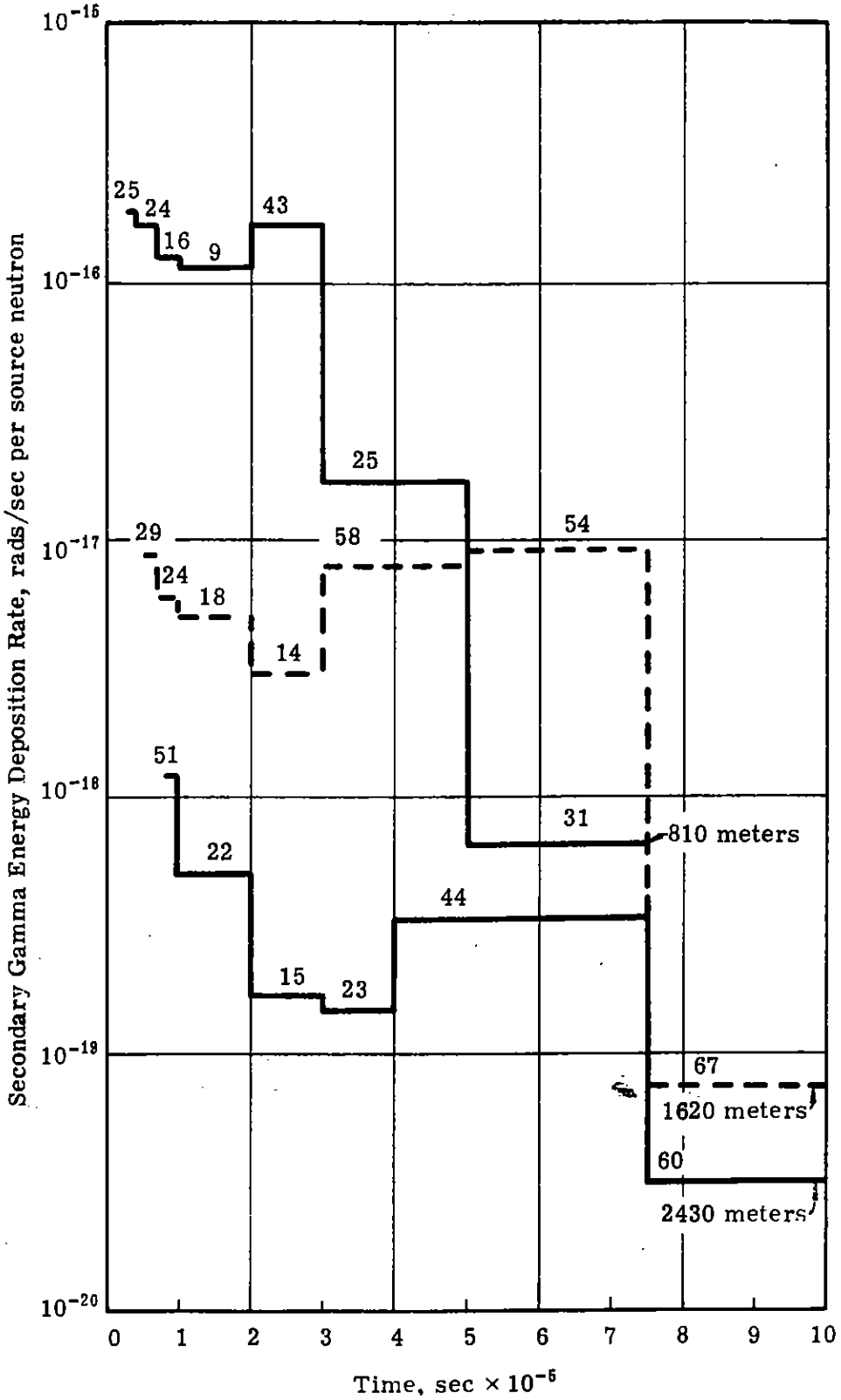

Fig. 51 — Secondary Gamma Energy Deposition Rate (Source: 7-Mev neutrons at 15,000 ft; Detectors: at 15,000 ft)

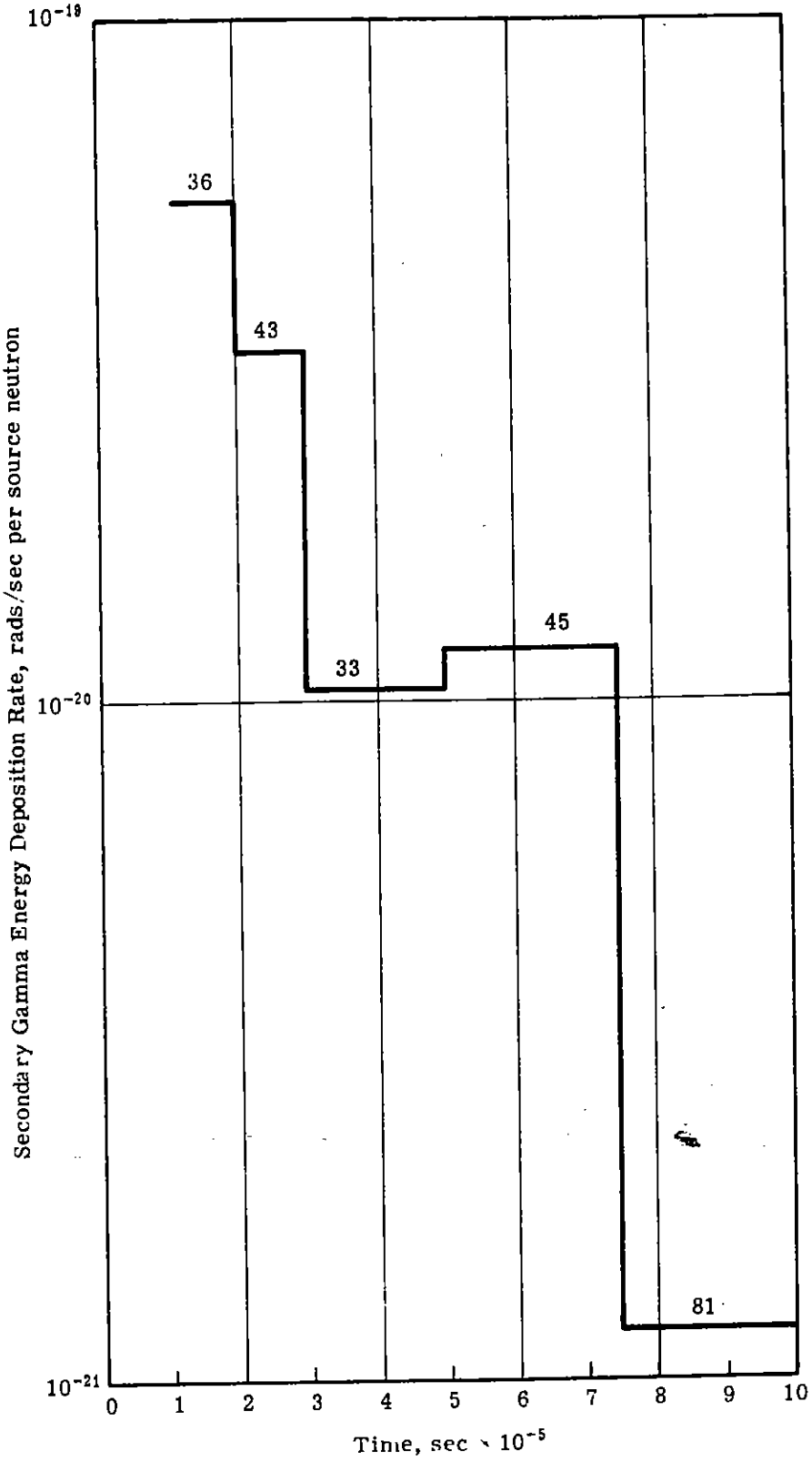

Fig. 52 — Secondary Gamma Energy Deposition Rate (Source: 7-Mev neutrons at 15,000 ft; Detector: 15,000 ft; Source to Detector: 3240 meters)

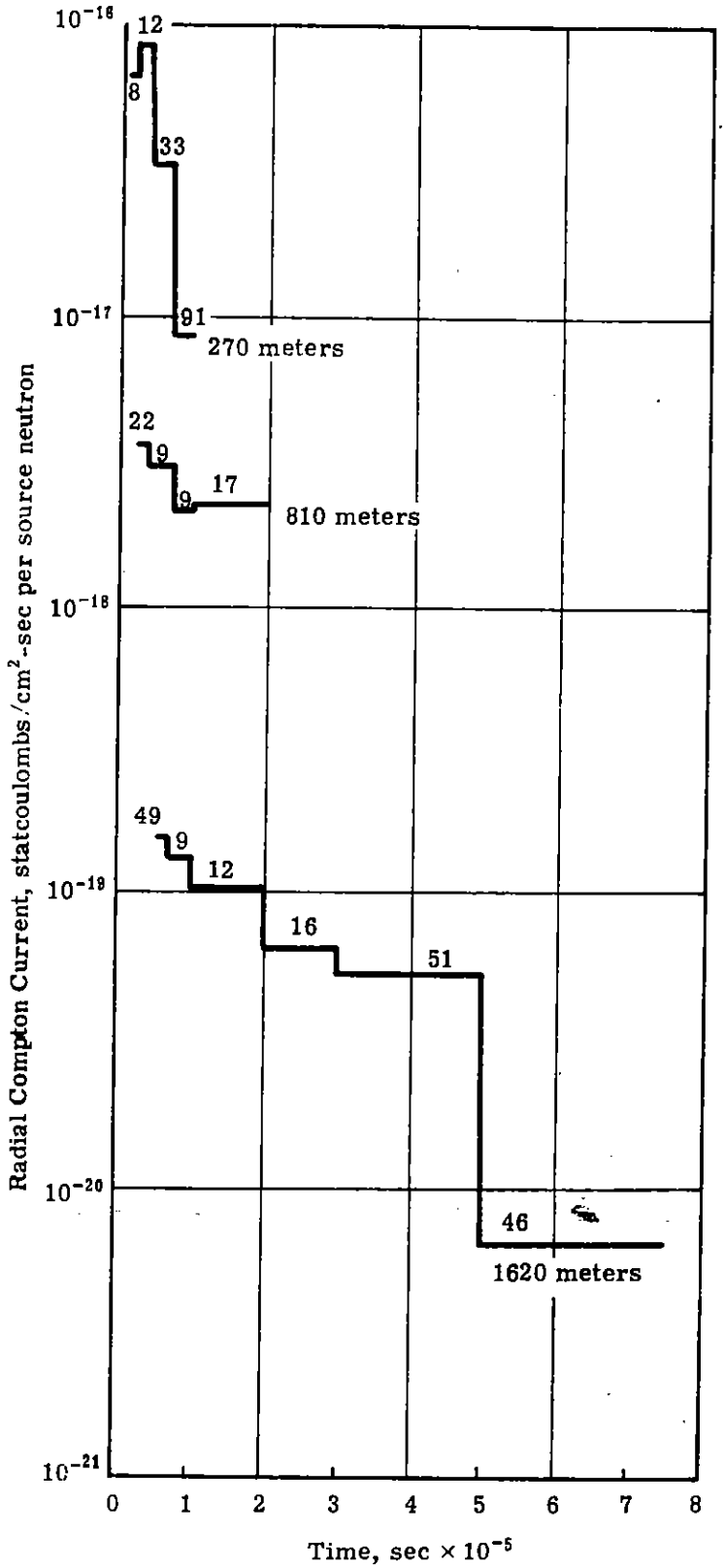

Fig. 53 — Radial Compton Current (Source: 14-Mev neutrons at 15,000 ft; Detectors: at 15,000 ft)

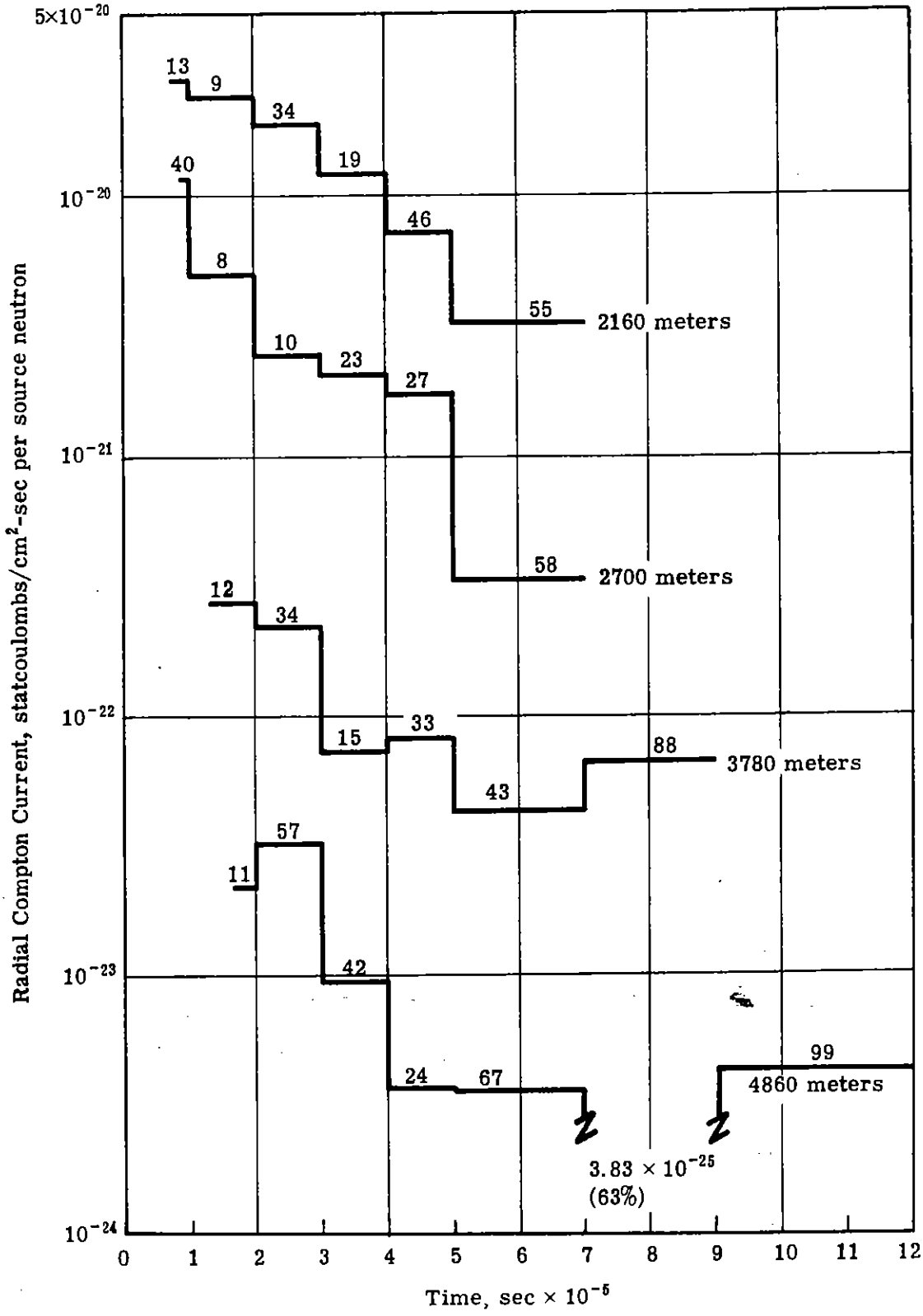

Fig. 54 — Radial Compton Current (Source: 14-Mev neutrons at 15,000 ft; Detectors: at 15,000 ft)

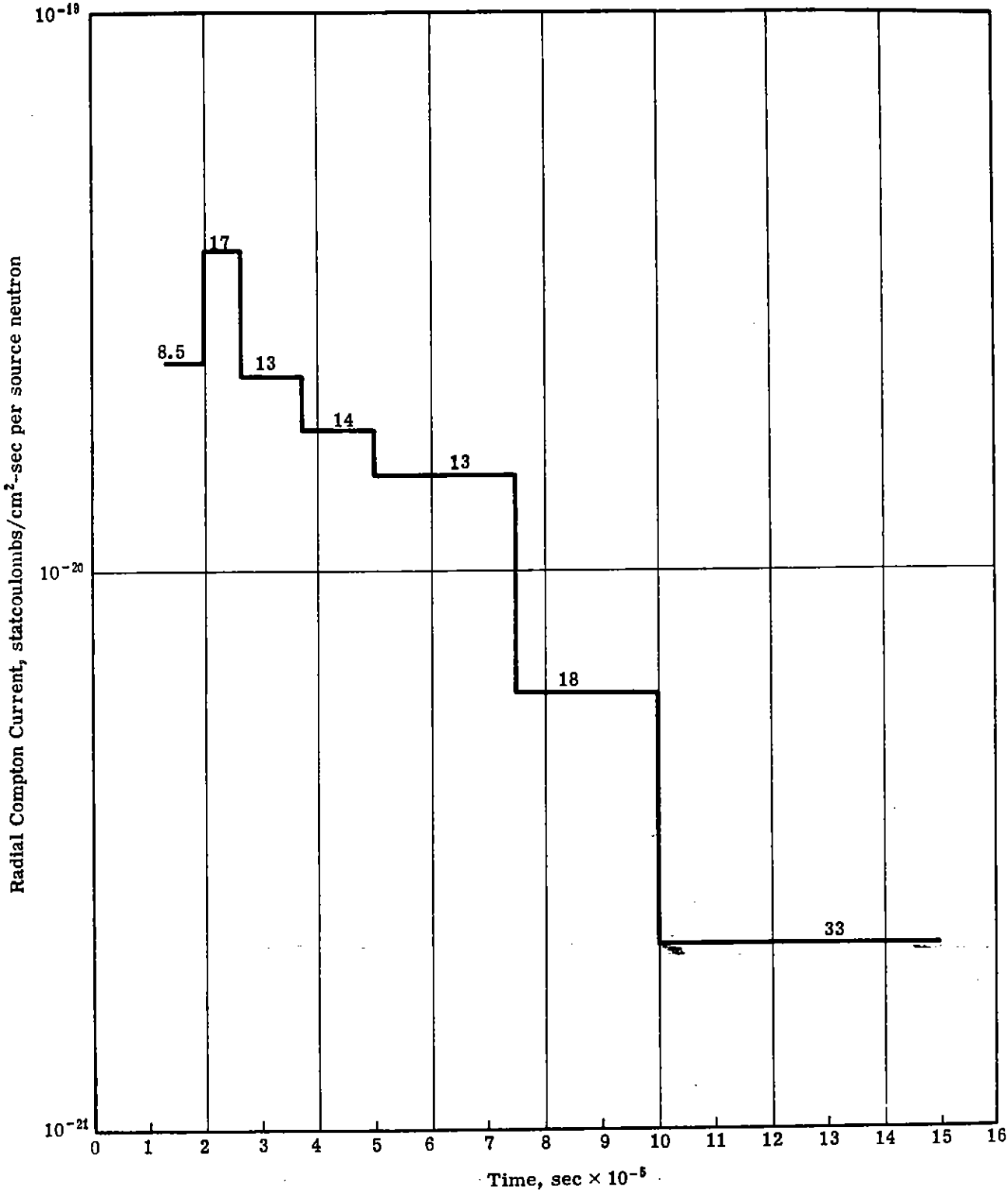

Fig. 55 — Radial Compton Current (Source: 14-Mev neutrons at 50,000 ft; Detector: 50,000 ft; Source to Detector: 3960 meters)

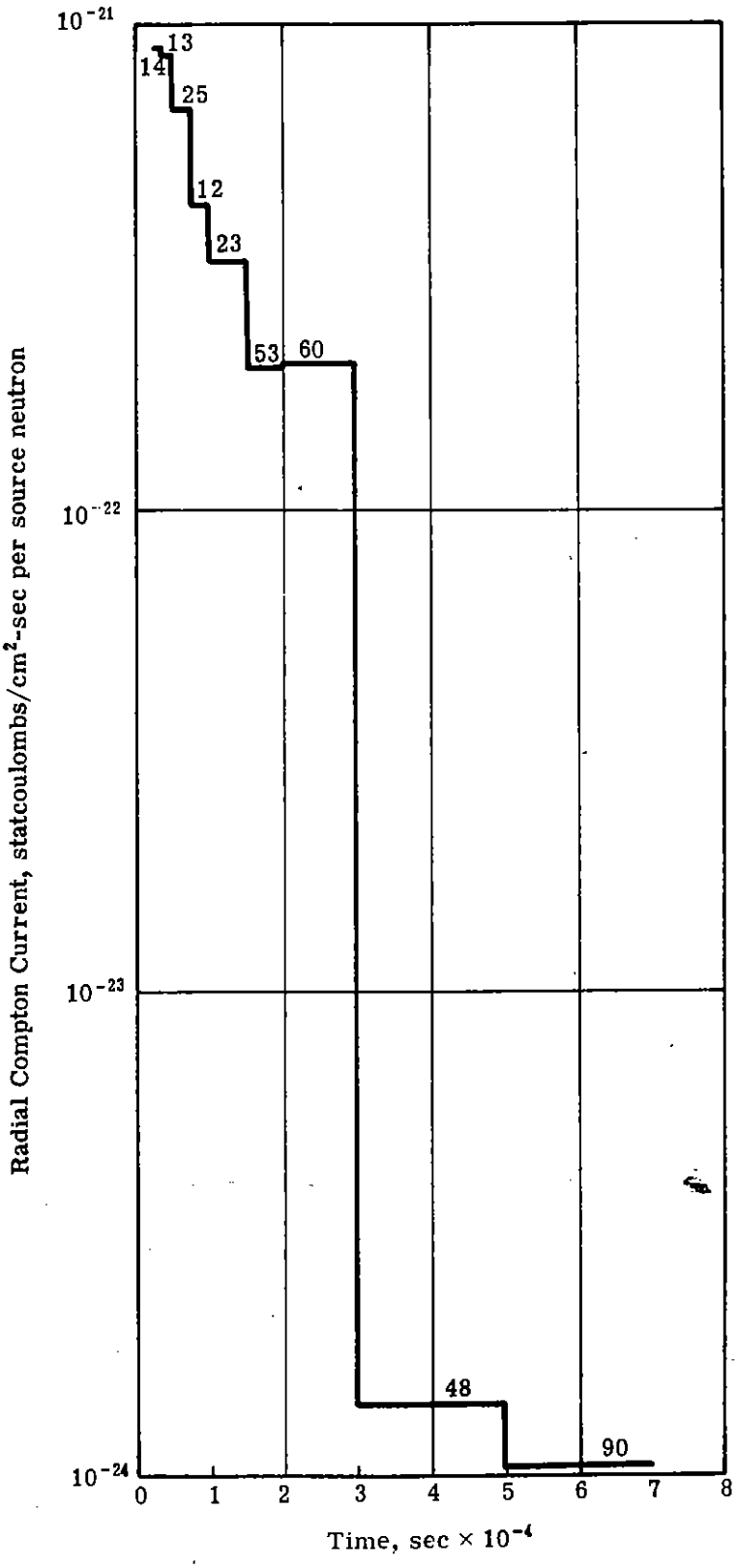

Fig. 56 — Radial Compton Current (Source: 14-Mev neutrons at 50,000 ft; Detector: 50,000 ft; Source to Detector: 7920 meters)

For a majority of the curves, one might suggest a "quick and dirty" single exponential fit to the data. It is apparent from these histograms, however, that the statistical uncertainties involved must be reduced and the number of time bins increased before meaningful fits to the data can be obtained.

A few examples of some of the better results for the polar Compton currents are presented as Figs. 57 through 61. Qualitatively, they are similar to the results from primary gamma radiation with an expanded time scale; that is, they are negative in sign at short times at detectors close to the source and are only positive in sign at larger penetrations.

Clearly, however, an accurate description of time-dependent polar currents from secondary gamma radiation requires improved statistical accuracy.

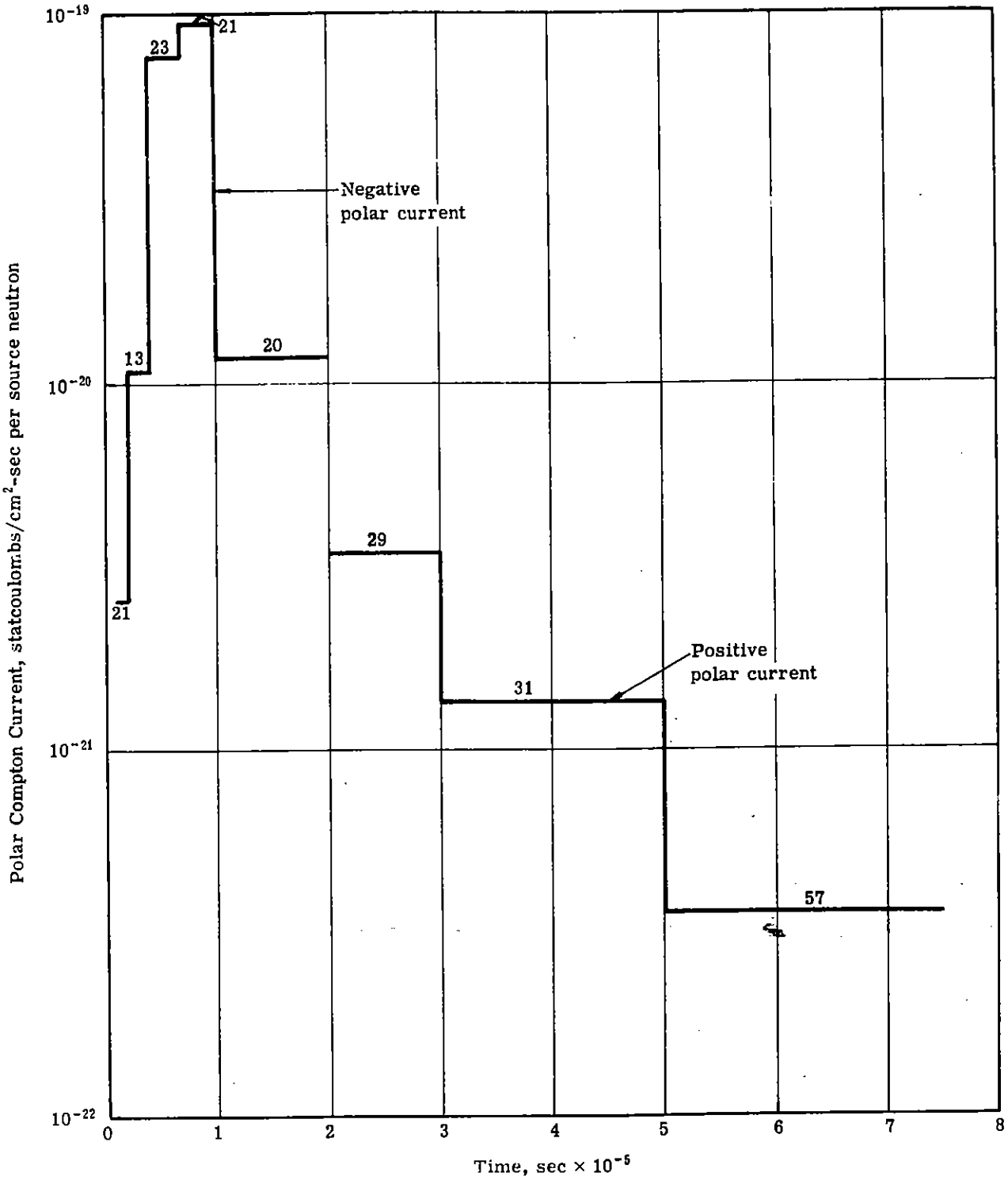

Fig. 57 — Polar Compton Current (Source: 7-Mev neutrons at 15,000 ft; Detector: 15,000 ft; Source to Detector: 270 meters)

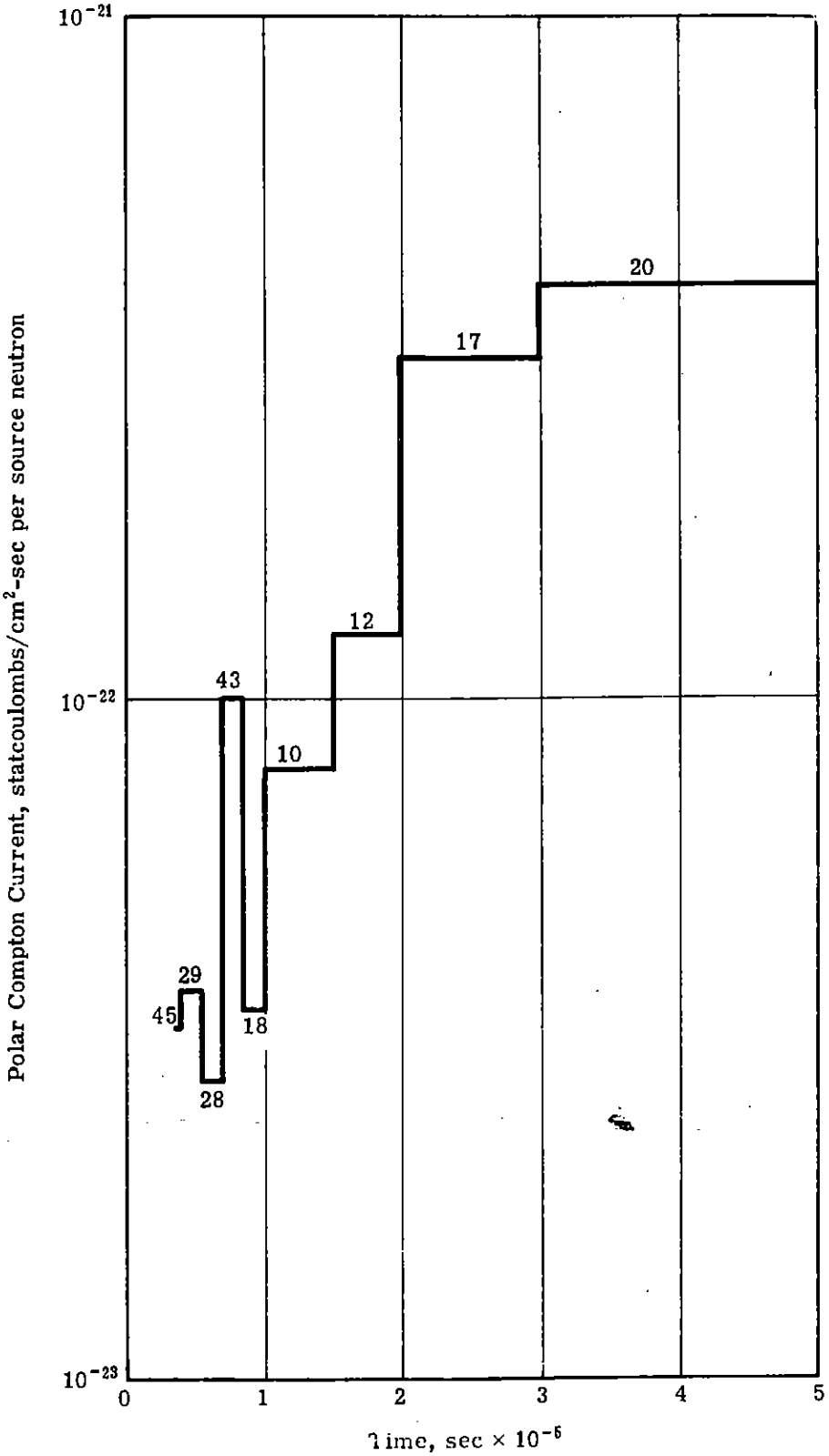

Fig. 58 — Polar Compton Current (Source: 5-Mev neutrons at 15,000 ft; Detector: 15,000 ft; Source to Detector: 1080 meters)

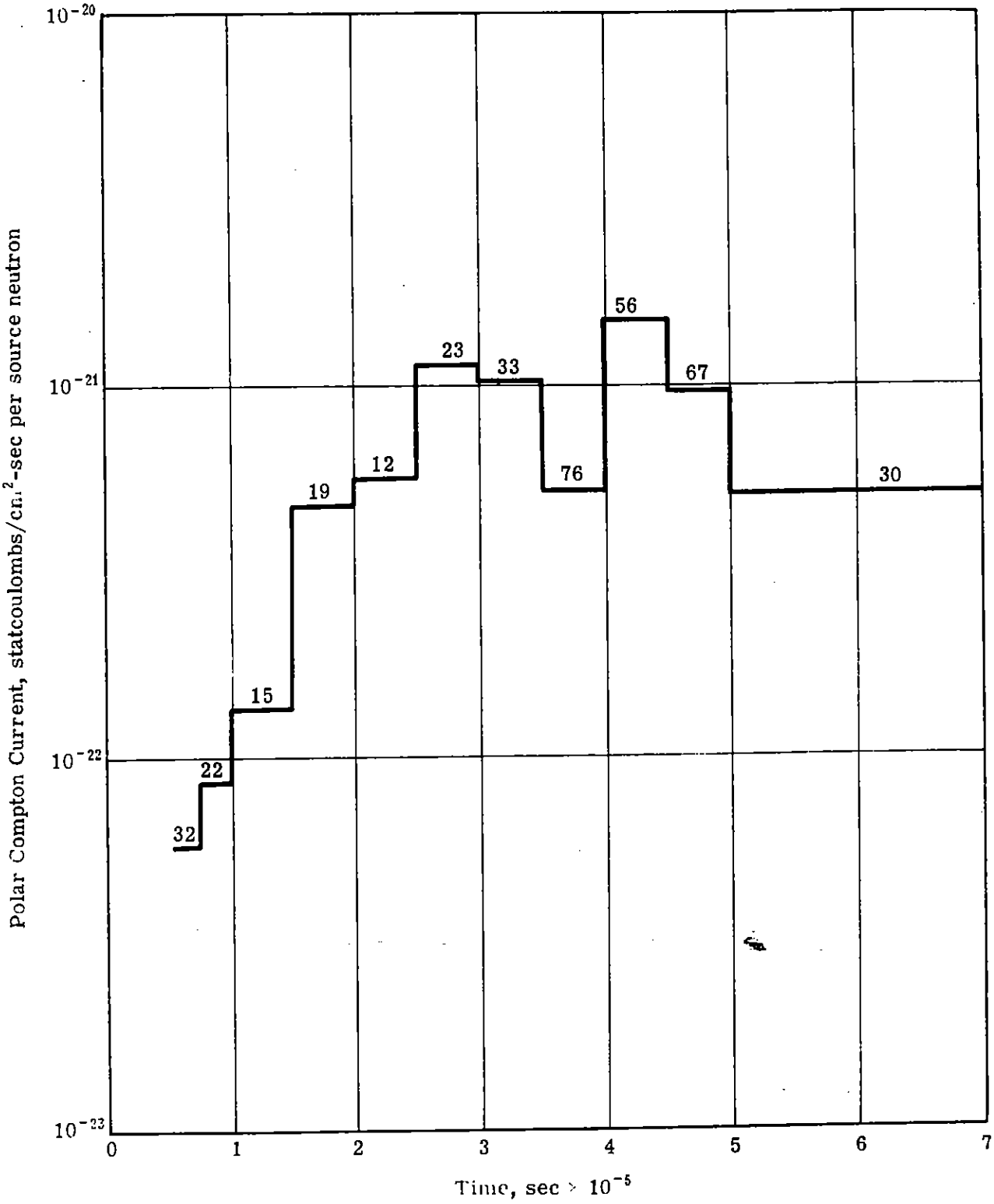

Fig. 59 — Polar Compton Current (Source: 10-Mev neutrons at 15,000 ft; Detector: 15,000 ft; Source to Detector: 1620 meters)

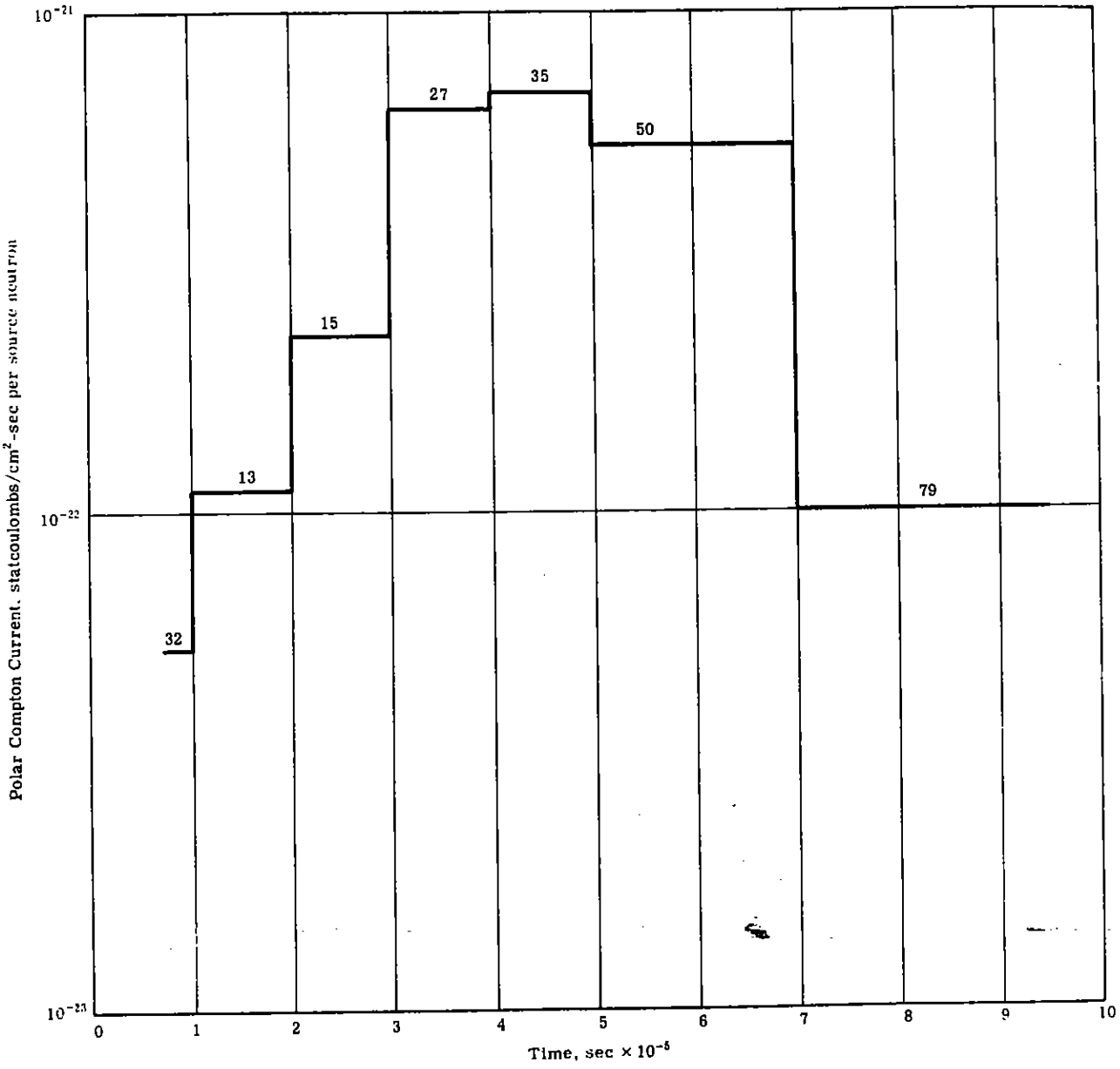

Fig. 60 — Polar Compton Current (Source: 14-Mev neutrons at 15,000 ft; Detector: 15,000 ft; Source to Detector: 2160 meters)

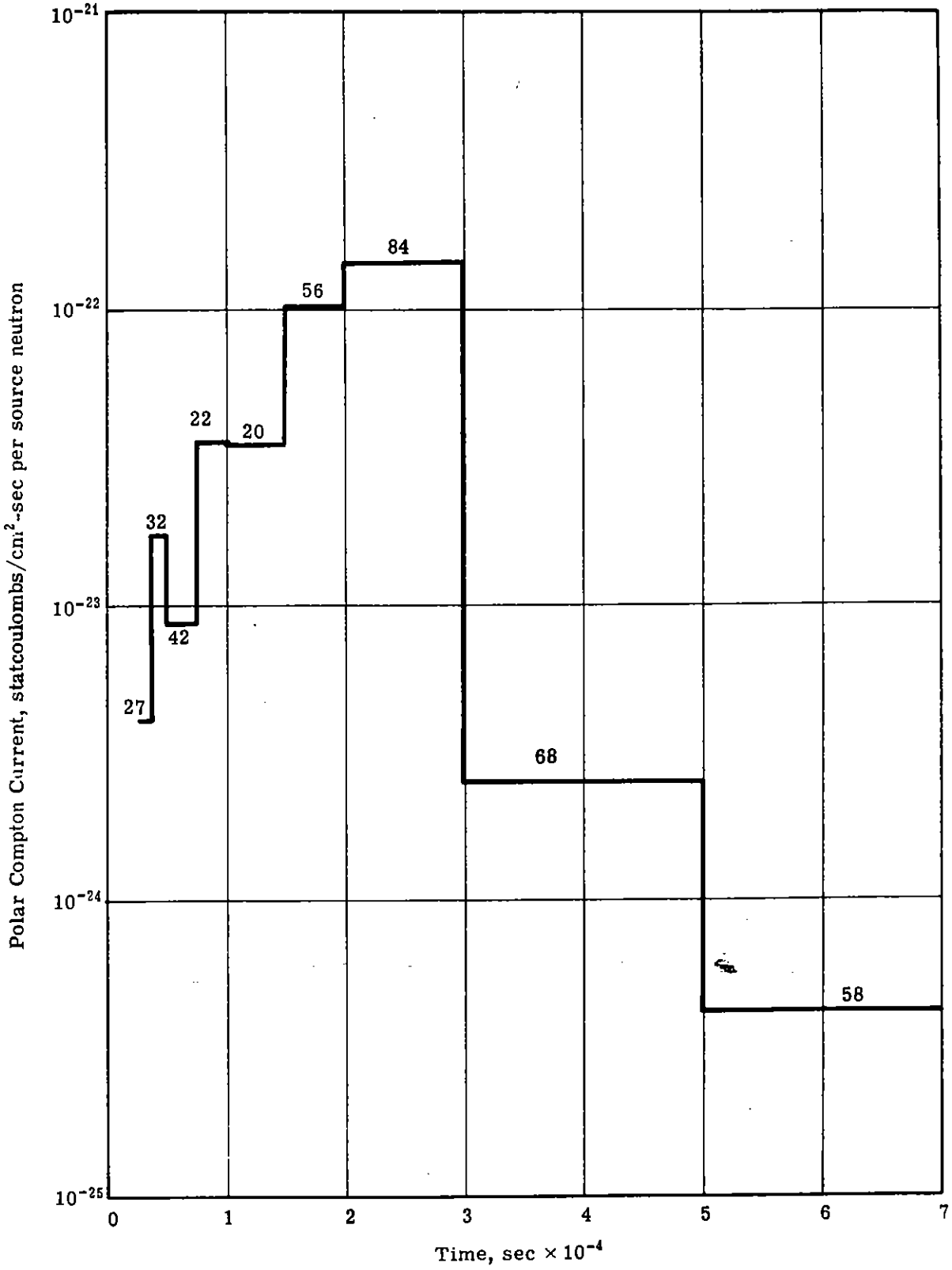

Fig. 61 — Polar Compton Current (Source: 14-Mev neutrons at 50,000 ft; Detector: 50,000 ft; Source to Detector: 7920 meters)

SECTION VI

RECOMMENDED FUTURE STUDIES

EXTENT OF APPLICABILITY

On the basis of the information obtained by this study, it is now possible to specify a program of supplemental calculations to be executed on a high-speed computer which will permit the determination of photon energy deposition and Compton current components for arbitrary source energies, altitudes, and detector positions within the following ranges of applicability:

Source altitude range	8000 to 50,000 ft
Primary gamma-ray source energy range	500 kev to 8 Mev
Primary neutron source energy range	5 Mev to 14 Mev
Source-detector range	Up to 10 mfp for primary gamma radiation or for the most significant secondary gamma radiation
Source-detector orientation	Arbitrary
Temporal range	From time of arrival of initial radiation until radiation is no longer significant, with greatly increased detail in the time description.

The appropriate information will be presented either in the form of accurate analytical expressions or in tabular form with interpolation schemes convenient as input to engineering codes.

The results of this proposed study will thus completely and conveniently describe energy deposition and Compton current components in the intermediate atmosphere for the entire range of radiation sources and detector locations which are of interest.

PROPOSED CODE MODIFICATIONS

The experience gained to date with CORSAIR shows that these proposed studies, described in detail on pages 92 through 103, can be executed most effectively if some modifications are made to the existing code. These proposed code modifications are discussed in this section.

Conversion of Code to a CDC-6600 System

An analysis of the time-dependent data of this report suggests that the average number of particle histories traced in a Monte Carlo calculation should be increased by a factor of at least 25 in order to reduce the typical variances of the output to acceptable levels. Clearly, it is impractical for such problems to be run on the United Nuclear CDC-1604-A computer, since the average running time per problem is, at present, about an hour.

It is recommended that CORSAIR be converted to the CDC-6600 computer to take advantage of its increased computation speed. For calculations of this type a reduction in computer time history of a factor of about 40 is anticipated.

The increase in machine speed, however, is not the sole reason for recommending conversion to a 6600 system. The additional fast memory available can be utilized to increase significantly the overall efficiency of the CORSAIR program by the elimination of much external magnetic tape reading and writing. This is included in the discussions which follow.

Internal Conversion of Photon Fluxes to Compton Currents

In the present version of CORSAIR the conversion of photon fluxes to Compton currents is performed, by necessity, rather inefficiently. Because of machine storage limitations, parameters describing all photon flux estimates first must be written on output magnetic tape. Subsequently, Program CORREDIT (see pages 7 and 8) reads in data from this tape and generates Compton currents. The computer time required by CORREDIT, for a given problem, is generally about 25% of the time required by CORSAIR.

With the increased memory available with a 6600 computer system, all conversions of photon flux to Compton current components will be performed internally.

Variable Time-Bin Structure

CORSAIR will be modified so that scores at each detector may be stored in time bins unique to that detector. Optimizing the time-bin structure for each detector in the time range important for that detector will reduce the machine storage requirements and simplify the data evaluation. In particular, it will be possible to examine results in adequate detail for very short temporal ranges.

This proposed modification already has been coded successfully into the related AIRTRANS code.[1]

Estimation of Uncollided Secondary Gamma-Ray Fluxes

The determination of uncollided photon fluxes from a distributed secondary gamma-ray source presents some difficulties. A direct

$$\frac{e^{-\lambda}}{4\pi R^2}$$

estimate from each source particle to each detector is not applicable, since this method leads to infinite variances in the results because of the $1/R^2$ term in the estimator.[14]

In the present version of CORSAIR, a test is made at each secondary gamma-ray source position to ascertain whether the source photon is within an (input data) specified "exclusion volume" surrounding a considered point detector. If it is not, the direct estimate is made. If it is located within the exclusion volume, an estimate, averaged to an assumed uniform source density within the volume, is made. It can be shown that this technique eliminates the infinite variance of the uncollided flux.[15]

This method is not entirely satisfactory since the exclusion volume must be large enough so that a sufficient number of source particles are within the volume, and at the same time must not be so large that the real source distribution within the volume is far from uniform.[14]

It is often difficult to meet both requirements simultaneously; even at its best, the method yields approximate scores of the uncollided flux regardless of the number of particle histories traced. It is felt that the use of this technique is partially responsible for the relatively large statistical fluctuations encountered to date in the secondary gamma radiation transport problems.

It is proposed to modify CORSAIR so that uncollided secondary gamma-ray fluxes are estimated by an improved method which already has been used successfully in the United Nuclear ATHENA Monte Carlo code.[16] With this method, uncollided secondary gamma-ray fluxes are estimated in the neutron transport problems. Each time a neutron goes into collision an estimate of the uncollided secondary flux is made, at each detector, by a technique similar to the once-more-collided calculation of the neutron fluxes.[2,3] In effect, the method biases the distribution of the sources of secondary radiation (with proper adjustment of photon "weight"), so that the infinite variance is removed from the uncollided flux estimator.[14,16]

This proposed estimation process requires that tables of gamma-ray production probabilities and gamma-ray cross sections be available to CORSAIR during the neutron transport problem. In the present CDC-1604-A version of the code, this is not possible because of storage restrictions. The additional required memory is available, however, for the proposed 6600 version.

Elimination of the Neutron Interaction Tape

In the present version of CORSAIR, parameters describing all neutron interactions which could possibly lead to the production of secondary gamma radiation are scored on an output "interaction" tape. Subsequently, Program ASP reads in the data from this tape, and, in conjunction with input tables of probability of gamma-ray production, generates a secondary gamma-ray source tape. With the increased memory available with a 6600 system, the production probability tables will be read in as input in the neutron CORSAIR problems and the secondary gamma-ray source tape will be generated directly. Hence it no longer will be necessary to run the intermediate ASP program.

PROPOSED ADDITIONAL CALCULATIONS

This section describes the additional Monte Carlo calculations which should be performed and analyzed in order to describe completely photon energy deposition and Compton currents in the intermediate altitude atmosphere from both primary neutron and primary gamma-ray sources.

To determine adequately the variation of all components as a function of altitude, the intermediate altitude range should be spanned by point sources of radiation positioned at altitudes of 8000, 15,000, 25,000, 35,000, and 50,000 ft. The primary gamma-ray source energies which should be evaluated to define the dependence on source energy are 0.5, 1, 2, 4, and 8 Mev. The source altitudes and primary gamma-ray source energies investigated in the preliminary study and presented in this document were limited to a 0.5-Mev source at altitudes of 15,000 and 50,000 ft, and a 5-Mev source at 15,000 ft. It is recommended that the primary neutron sources not be represented as monoenergetic sources, as was done in the preliminary studies reported herein, since the many large resonances in the nitrogen and oxygen interaction cross sections make the results sensitive to the exact energy chosen. Instead, sources having uniform distributions from $4\frac{1}{2}$ to $5\frac{1}{2}$, $6\frac{1}{2}$ to $7\frac{1}{2}$, and $9\frac{1}{2}$ to $10\frac{1}{2}$ Mev, and a narrow energy spectrum about 14 Mev will be used.

It is expected that calculations for coaltitude sources and detectors may be required for all combinations of these source altitudes and energies. However, it should be recognized that some of these calculations may not be required to obtain a general description of the desired quantities, and care should be exercised in the performance and evaluations of the calculations to insure that unnecessary problems are not treated.

The number of particle histories traced, per problem, should be of the order of 125,000 to 750,000. Source-detector penetrations of 1/2, 1, 2, 3, 5,

7, and 9 mfp are recommended. The analyses of the results will provide general descriptions of the desired quantities for penetration distances up to 10 mfp. (For the secondary gamma-ray problems, penetrations listed above represent mean free paths of the most significant secondary gamma radiation.)

The number of histories required for the proposed additional problems depends upon two factors: the source-detector penetration distance and the source-detector orientation.

More histories are required to obtain statistics at deep penetrations which are comparable to those at small penetrations because of the geometry factors involved.

For noncoaltitude sources and detectors, the flux-at-a-point technique must be used to obtain the required answers. For coaltitude sources and detectors, however, the more effecient flux-at-a-ring[4] technique can be employed to reduce the necessary number of histories by a factor of approximately two, for detectors within 3 mfp of a source, and by a factor of three for detectors at deeper penetrations.[5]

Based upon the statistical accuracy obtained in the calculations performed to date and the more detailed time interval description suggested for additional calculations, it is estimated that the required number of histories to be followed to permit 10 to 15% statistical accuracy in individual time bins is as in Table III. This table is applicable for both the primary and secondary gamma radiation problems. It is estimated that a secondary gamma-ray study will consume on the average approximately twice the amount of computer running time, per history, as will a primary gamma-ray problem.

The functional relationship between polar Compton current from primary gamma radiation and source-detector orientation appears, from the results of

TABLE III

REQUIRED NUMBER OF HISTORIES FOR PROPOSED ADDITIONAL PRIMARY AND SECONDARY GAMMA-RAY PROBLEMS*

	Source-Detector Penetration, λ†	
	λ ≤ 3	λ > 3
Coaltitude Source and Detector	125,000	250,000
Noncoaltitude Source and Detector	250,000	750,000

*In all cases, the number of histories represents the required number of primary radiation histories.

†For secondary gamma radiation problems, λ represents mean free paths of the most significant secondary radiation.

this report, to be not highly sensitive to source altitude or energy. Hence, computations at noncoaltitude detectors can be performed for selected photon sources only. It is suggested that the dependence of polar current with source-detector orientation be investigated systematically for those photon sources, mentioned above, which are either at an altitude of 15,000 or 35,000 ft, or which have an emission energy of 1 or 4 Mev. For these sources, Compton currents should be determined at coaltitude detectors, and in addition, at detectors located 30° and 45° both above and below the horizontal axis. The results obtained to date for the 0.5 and 5-Mev sources at 15,000 and 50,000 ft indicate that these suggested source-detector orientations are sufficient to determine the angular dependency. However, wherever initial results demonstrate that the functional relationship may be considered to be symmetric about the horizontal (particularly for the lower energy sources at the lower altitudes where the variations in atmospheric density encountered are not large), detailed studies at 15° and 60° above the horizontal axis may be substituted for those 30° and 45° below the horizontal, to establish, with increased accuracy, the dependence of polar current upon source-detector orientation. These additional angles also should be investigated for at least two of the high source energy-high source altitude configurations, e.g., the 2-Mev source at 50,000 ft and the 8-Mev source at 25,000 ft.

It is expected that the results obtained for the source-detector configurations specified above, analyzed in conjunction with the results given earlier in this report, will provide an accurate general description of polar currents, in the intermediate altitude, from the primary photon sources of interest.

The functional behavior of polar currents with source-detector orientation for secondary gamma radiation also is expected to be not highly sensitive to source altitude or energy and should be investigated for neutron sources at selected altitudes and energies only. Suggested are source altitudes of 15,000 and 35,000 ft. The source energy bands of $6\frac{1}{2}$ to $7\frac{1}{2}$ Mev and the band about 14 Mev

are suggested as representative of the source neutron energies. The results obtained to date do not give a clear indication as to how many source-detector orientations are required to determine the desired functional relationship. Hence, the proposed study initially specifies that the noncoaltitude detectors be located at 15°, 30°, 45°, and 60°, both above and below the horizontal axis. Based on the results which are obtained in the configurations investigated first, some of these locations may prove to be unnecessary, so that they can be deleted from later calculations.

The time-bin structure for all primary gamma radiation problems will be specified so that the decrease of intensity of the radial Compton current across any time bin will be limited to a factor of approximately $\sqrt{2}$.

To determine the input time-bin data for the Monte Carlo calculations, appropriate to intensity decreases of approximately $\sqrt{2}$, the radial current will be assumed to vary with time according to the model proposed by Schaefer[17] based upon early time behavior calculated by LeLevier:[12,17]

$$I(t) = I_0 \exp\left[-\sqrt{(t-t_u)}/K\right]$$

where K = constant with time; a function of source energy and source-detector distance

t = real time

t_u = time of arrival of uncollided photons.

The Schaefer fit, while not providing an accurate description of the time dependence after the early time intervals, does provide a smoothly varying dependence which is a reasonable "average" and is quite satisfactory for prescription of a suitable time-bin structure.

Numerical examples of the time-bin structure derived from the Schaefer model for the 5-Mev photon source, at an altitude of 15,000 ft, are presented in

Table IV. Times are in units of retarded time (real time minus uncollided arrival time). Comparison with the time-bin structure used in this report can be made by reference to Figs. 20 and 21.

TABLE IV

TIME-BIN STRUCTURE BASED ON SCHAEFER MODEL

Source: 5-Mev photons at an altitude of 15,000 ft
Detectors: Coaltitude to source
Time Bin Boundaries: In seconds*

At 1 mfp (Uncollided Arrival Time = 1.5637×10^{-6} sec)		At 5 mfp (Uncollided Arrival Time = 7.8183×10^{-6} sec)	
0		0	
3.33	(−9)†	4.34	(−9)
1.33	(−8)	1.74	(−8)
3.00	(−8)	3.91	(−8)
5.33	(−8)	6.95	(−8)
8.32	(−8)	1.09	(−7)
1.20	(−7)	1.56	(−7)
1.63	(−7)	2.13	(−7)
2.13	(−7)	2.78	(−7)
2.70	(−7)	3.52	(−7)
3.33	(−7)	4.34	(−7)
4.03	(−7)	5.26	(−7)
4.79	(−7)	6.25	(−7)
5.62	(−7)	7.34	(−7)
6.52	(−7)	8.51	(−7)
7.49	(−7)	9.77	(−7)
8.52	(−7)	1.11	(−6)
9.62	(−7)	1.26	(−6)
1.08	(−6)	1.41	(−6)
1.20	(−6)	1.57	(−6)
1.33	(−6)	1.74	(−6)
1.47	(−6)	1.92	(−6)
1.61	(−6)	2.10	(−6)
1.76	(−6)	2.30	(−6)

*Retarded time – to two significant figures.
†(−9) = $\times 10^{-9}$, etc.

TABLE IV — (CONCLUDED)

At 1 mfp (Uncollided Arrival Time = 1.5637×10^{-6} sec)	At 5 mfp (Uncollided Arrival Time = 7.8183×10^{-6} sec)
1.92 (-6)*	2.50 (-6)
2.08 (-6)	2.71 (-6)
2.25 (-6)	2.94 (-6)
2.43 (-6)	3.17 (-6)
2.61 (-6)	3.40 (-6)
2.80 (-6)	3.65 (-6)
3.00 (-6)	3.91 (-6)
3.20 (-6)	4.17 (-6)
3.41 (-6)	4.45 (-6)
3.62 (-6)	4.73 (-6)
3.85 (-6)	5.02 (-6)
4.08 (-6)	5.32 (-6)
4.31 (-6)	5.63 (-6)
4.56 (-6)	5.95 (-6)
4.81 (-6)	6.27 (-6)
5.06 (-6)	6.61 (-6)
	6.95 (-6)
	7.30 (-6)
	7.66 (-6)
	8.03 (-6)
	8.41 (-6)
	8.79 (-6)
	9.19 (-6)
	9.59 (-6)
	1.00 (-5)
	1.04 (-5)

*(-6) = $\times 10^{-6}$, etc.

From these and similar examples we have concluded that time-bin structures determined on the basis of the Schaefer model are appropriate and sufficiently detailed for radial currents over the entire temporal range, and also are appropriate for the energy deposition rates and polar currents as well.

Evidence obtained to date indicates that the temporal behavior of secondary gamma-ray energy deposition from primary neutron sources can be represented by a simplified model illustrated in Fig. 62.

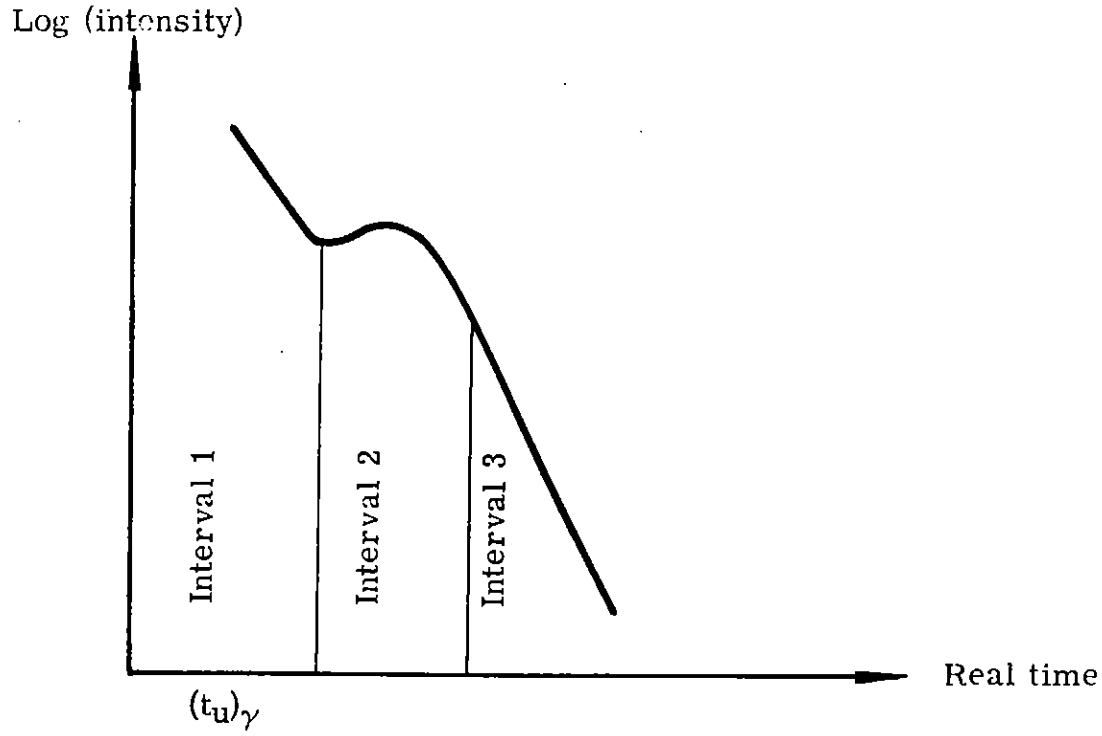

Fig. 62 — Temporal Behavior of Secondary Gamma-Ray Energy Deposition from a Primary Neutron Source

Photon energy deposition occurs initially at time $t = (t_u)_\gamma$, corresponding to the time of flight of photons which are generated by uncollided neutron interactions at the source at time $t = 0$, and which fly uninterrupted to the detector.

Initially (interval 1 of Fig. 62), the energy deposition rate decreases with time in a manner which can be approximated by a simple exponential. The decay constant, associated with the energy deposition vs time, is insensitive to source energy, source-detector orientation, and source-detector separation, except as noted below, for very small separations.

The 1/e decay period of the exponential is about twice the time flown by a source neutron before it suffers a nonelastic scattering collision. (This be-

havior is not unreasonable since neutron flight times dominate the temporal behavior of the deposition of energy by secondary gamma radiation, and since most secondary gamma radiation is produced by the first two nonelastic interactions of 5 to 14-Mev source neutrons.)

(For detectors positioned close to the neutron source most of the secondary gamma rays are born at penetration distances beyond the detector, and the most intense gamma radiation arrives at a detector later than the arrival of the uncollided neutron pulse. Hence, the initial exponential decay period, discussed above, will not be present.)

At some time following the arrival of the initial photons the uncollided neutron pulse passes through the detector. Commencing at some time preceding this event and terminating at some time afterwards (interval 2 of Fig. 62), the energy deposition rate falls away less sharply with time, and indeed, the energy deposition rate may increase while the pulse passes through the detector. (In the limiting case of a monoenergetic neutron source emitting all of its radiation instantaneously, the energy deposition rate actually becomes infinite at the time of arrival of uncollided neutrons at a detector.)

After the uncollided neutron pulse passes through the detector, the energy deposition rate continues to decay with time in a manner which resembles the initial exponential decay (interval 3 of Fig. 62), but which was not determined accurately enough in this study to describe with a decay constant.

It is proposed to set up the time-bin structure for the Monte Carlo secondary gamma radiation calculations to take into account the three temporal ranges which have been discussed.

For the shortest temporal range (i.e., interval 1 of Fig. 62), 10 equally spaced time bins will be specified.

The number of time bins will be increased for those distant detectors for which the exponential model, discussed above, predicts a decrease in intensity in this time range which exceeds a factor of 30.

In addition, the initial time bin will be further subdivided, for at least four representative initial problems, to determine whether any unsuspected temporal structure exists at the earliest times.

The temporal region which surrounds the time of arrival of the uncollided neutron pulse (interval 2 of Fig. 62) will be investigated by calculating a time-bin width equal to one-half the time spread in the arrival of uncollided neutrons at the detector. Five time bins of this width will be specified on each side of the average time of arrival of the uncollided neutron pulse.

The third and final temporal range will be described by time bins, each wider than its predecessor by a factor of $\sqrt{2}$, starting with an initial bin width equal to those in the "neutron pulse" temporal range and terminating at times when the intensity is too low to be measured accurately by these Monte Carlo calculations. A final "catch all" time interval will be included for each detector.

Based on the model and procedures described above, the time in structure for all combinations of sources and detectors should be adequate to determine, in sufficient detail, the temporal behavior of energy deposition from secondary gamma radiation.

A numerical example of the time-bin structure derived from this model, for a $6\frac{1}{2}$ to $7\frac{1}{2}$ Mev energy-distributed neutron source at an altitude of 15,000 ft, is presented in Table V. The detector is coaltitude to the source at a penetration of 1620 meters. Times represent the boundaries of the time intervals in which data are accumulated, in units of real time. A comparison with the time-bin structure used in this report can be made by reference to the "1620-meter" histogram of Fig. 51, for a primary 7-Mev neutron source.

TABLE V

TIME-BIN STRUCTURE BASED ON THREE-REGION MODEL

Source: $6\frac{1}{2}$ to $7\frac{1}{2}$-Mev neutrons at an altitude of 15,000 ft
Detector: Coaltitude to source at 1620 meters
Earliest Arrival Time of Photon Flux: 5.40×10^{-6} sec
Arrival Time of Average Energy Uncollided Neutron Flux: 4.43×10^{-5} sec

Time Bins, sec *	
5.40×10^{-6}	Exponential region (model predicts decrease in intensity by $\sqrt{2}$ every 1.0×10^{-5} sec)
8.52	
1.16×10^{-5}	
1.47	
1.79	
2.10	
2.41	
2.72	
3.03	
3.34	
3.65×10^{-5}	Uncollided neutron pulse region
3.81	
3.96	
4.12	
4.28	
4.43	
4.58	
4.74	
4.89	
5.05	
5.21×10^{-5}	Final decay region
5.36	
5.58	
5.89	
6.33	
6.93	
7.78	
8.98	
1.07×10^{-4}	
1.33	
1.67	

*To two significant figures.

The data presented in this report indicate that the general temporal behavior of radial currents from secondary gamma radiation resembles that of the energy deposition rates except that the peaking, corresponding to the time when the uncollided neutron pulse passes through the detector, is absent and the amplitude decreases very rapidly thereafter. Hence the time-bin structure discussed above is appropriate for radial Compton currents as well.

Polar Compton currents from secondary gamma radiation initially rise rapidly with time and then vary less rapidly with time than do the energy deposition rates or radial currents. The time-bin structures described above also should be sufficient for the determination of the polar Compton currents.

SECTION VII

REFERENCES

1. Cohen, M. O.: AIRTRANS – A Time-Dependent Monte Carlo System for Radiation Transport in a Variable Density Atmosphere and the Ground, UNC-5179 (June 1967).

2. Kalos, M. H.: On the Estimation of Flux at a Point by Monte Carlo, Nuclear Sci. and Eng., 16:1 (May 1963).

3. Ibid., Reference 1, pp. 46-48 and Appendix B.

4. Troubetzkoy, E. S.: Estimation of Flux-at-a-Point in Cylindrically Symmetric Problems, Internal UNC Memo, Phys/Math-4829 (Aug. 26, 1966).

5. Troubetzkoy, E. S. and Cohen, M. O.: Flux-at-a-Point Estimation for Cylindrically Symmetric Problems, Trans. Am. Nuclear Soc., Vol. X (June 1967).

6. Ibid., Reference 1, pp. 48-49.

7. Henderson, B. J.: Conversion of Neutron or Gamma-Ray Flux to Absorbed Dose Rate, XDC59-8-179 (Aug. 14, 1959).

8. "U. S. Standard Atmosphere – 1962," p. 9, U. S. Government Printing Office, Washington, D. C., Dec. 1962.

9. McMaster, W. H. et al.: Section II, Compilation of X-Ray Cross Sections, UCRL-50174 (Jan. 1967).

10. Davison, C. M.: "Gamma Ray Attenuation Coefficients," Appendix 1 of "Alpha-,Beta-, and Gamma-Ray Spectroscopy," Kai Seigbahn, Ed., North-Holland Publishing Co., Amsterdam, 1965.

11. Goldstein, H.: "Fundamental Aspects of Reactor Shielding," p. 368, Addison Wesley Publishing Co., Inc., Reading, Mass., 1959.

12. LeLevier, R. E.: The Compton Current and the Energy Deposition Rate from Gamma Quanta – A Monte Carlo Calculation, RM-4151-PR, p. 35 (June 1964).

13. Cohen, M. O.: Energy Deposition Rates and Radial and Polar Compton Currents from Gamma Ray and Neutron Sources in the Intermediate Altitude Range, Internal UNC Memo, Phys/Math-5076 (Aug. 16, 1967).

14. Kalos, M. H.: Secondary Gamma Ray Flux at a Point, Internal UNC Memo. Phys/Math 3241 (Nov. 22, 1963).

15. Ibid., Reference 1, pp. 43-44

16. Spielberg, D.: ATHENA – A System of FORTRAN Programs for Radiation Transport and Heating Calculations in Complex Reactor Geometries, NASA-CR-54905 and UNC-5148 (Mar. 1966).

17. Shaefer, R. R.: Curve Fits to the Electric Current and Ionization Rate Delta Function Responses, Dikewood Corporation EMP Theoretical Notes – Note XX (Sept. 10, 1966).

This page intentionally left blank.

APPENDIX A – ANTITHETIC CORRELATION OF FLUX ESTIMATORS IN THE ATMOSPHERE*

A.1 THE PROBLEM TO BE SOLVED

Given a point isotropic source at Σ, we wish to estimate the polar component of the flux at a detector point D. If we try to solve the problem using standard Monte Carlo methods, we expect to run into difficulty since particular histories will give either positive or negative contributions to the result. The

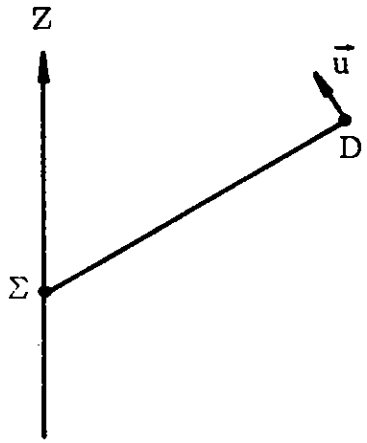

net result is expected to be a small difference between these large negative and positive contributions. We therefore use an antithetic correlation technique to obtain, as far as possible, a direct estimate of the difference between positive and negative contributions.

*Taken from UNC internal memo Phys/Math-5048, by E. S. Troubetzkoy (June 29, 1966).

A.2 A ONE-DIMENSIONAL EXAMPLE

Let us examine a one-dimensional analogue to the problem. Suppose we have to evaluate an integral

$$\overline{F} = \int_{-1}^{1} f(x)\, p(x)\, dx \qquad \text{(A-1)}$$

where $p(x)$ is a probability distribution function for $-1 \leq x \leq 1$ and $f(x)$ is an estimator.

Let us assume that

$$f(x) = -f(-x) \qquad \text{(A-2)}$$

and that $p(x)$ is almost symmetrical with respect to $x = 0$.

$$p(x) \approx p(-x) \qquad \text{(A-3)}$$

If Eq. A-3 was an exact equality, $\overline{F}$ would be identically zero. Let us consider the case where Eq. A-3 is only an approximate relationship.

If we were to evaluate the integral (Eq. A-1) by standard Monte Carlo methods, the variance would be given by

$$\sigma^2 = \overline{F^2} - (\overline{F})^2$$

where

$$\overline{F^2} = \int_{-1}^{1} [f(x)]^2\, p(x)\, dx \qquad \text{(A-4)}$$

Let us now introduce a specific form of antithetic correlation, and correlate a point x with the point $(-x)$.

The calculation of the mean correlated estimator $\overline{F}_c$ and of the mean square

correlated estimator $\overline{F_c^2}$ is as follows:

$$\overline{F}_c = \int_{-1}^{1} \left[\frac{f(x) + f(-x) \frac{p(-x)}{p(x)}}{2} \right] p(x)\, dx$$

$$\overline{F_c^2} = \int_{-1}^{1} \left[\frac{f(x) + f(-x) \frac{p(-x)}{p(x)}}{2} \right]^2 p(x)\, dx$$

where $\overline{F}_c$ obviously is equal to $\overline{F}$.

Taking Eq. A-2 into account, we can write:

$$\overline{F}_c = \int_{-1}^{1} f(x) \left[\frac{1 - \frac{p(-x)}{p(x)}}{2} \right] p(x)\, dx$$

$$\overline{F_c^2} = \int_{-1}^{1} [f(x)]^2 \left[\frac{1 - \frac{p(-x)}{p(x)}}{2} \right]^2 p(x)\, dx. \qquad \text{(A-5)}$$

With probability p(x) we estimate the quantity

$$f(x) \left[\frac{1 - \frac{p(-x)}{p(x)}}{2} \right]$$

It is seen from Eqs. A-4 and A-5 that $\sigma_c^2 << \sigma^2$ (that is that the technique is a great improvement), if

$$\left[1 - \frac{p(-x)}{p(x)} \right]^2 << 1$$

that is if relationship (Eq. A-3) is indeed approximately satisfied.

A.3 SOLUTION TO THE ACTUAL PROBLEM

Restating the problem of Section A.1, we have to evaluate the integral

$$\overline{F}(\vec{D},E) = \int (\vec{\Omega}\cdot\vec{u})\,\psi(\vec{D},\vec{\Omega},E)\,d\tau_{\Omega} \qquad (A\text{-}6)$$

where $\vec{u}$ is the polar direction at D, $\vec{\Omega}\cdot\vec{u}$ is the estimator of interest, and $\psi(\vec{D},\vec{\Omega},E)\,d\tau_{\Omega}$ is the probability of a unit vector $\vec{\Omega}$ to be within $d\tau_{\Omega}$ ($d\tau_{\Omega}$ is an infinitesimal element of solid angle around $\vec{\Omega}$).

ψ satisfies the Boltzman equation:

$$\psi(\vec{P},\vec{\Omega},E) = S(\vec{P},\vec{\Omega},E) + \int \psi(\vec{P}',\vec{\Omega}',E)\,T(\vec{P}'-\vec{P})\,|(E')\,C(\vec{\Omega}'-\vec{\Omega},E'-E)\,d\tau_{P'},d\tau_{\Omega'},dE' \qquad (A\text{-}7)$$

Let us now correlate each point $\vec{P}$, $\vec{\Omega}$, E to a point $\vec{P}_1$, $\vec{\Omega}_1$, E, where $\vec{P}_1$, $\vec{\Omega}_1$ are symmetrical of $\vec{P},\vec{\Omega}$ with respect to the line ΣD. As the line of reflection passes through D, we obviously have $D_1 = D$. We also have $\vec{\Omega}\cdot\vec{u} = -\vec{\Omega}_1\cdot\vec{u}$, and we achieve a correlation of the type described in the example of Section A.2.

$\psi(\vec{P}_1,\vec{\Omega}_1,E)$ satisfies an equation identical to Eq. A-7:

$$\psi(\vec{P}_1,\vec{\Omega}_1,E) = S(\vec{P}_1,\vec{\Omega}_1,E) +$$

$$+ \int \psi(\vec{P}_1',\vec{\Omega}_1',E)\,T(\vec{P}_1'-\vec{P}_1)\,|(E')\,C(\vec{\Omega}_1'-\vec{\Omega}_1,E'-E)\,d\tau_{P_2'}\,d\tau_{\Omega_1'}\,dE'$$

which we can rewrite in the form:

$$\psi(\vec{P}_1,\vec{\Omega}_1,E) = S(\vec{P},\vec{\Omega},E)\frac{S(\vec{P}_1,\vec{\Omega}_1,E)}{S(\vec{P},\vec{\Omega},E)} +$$

$$+ \int \psi(\vec{P}_1',\vec{\Omega}_1',E)\, T(\vec{P}'-\vec{P})\,|(E')\, \frac{T(\vec{P}_1'-\vec{P}_1)\,|(E')}{T(\vec{P}'-\vec{P})\,|(E')}\, C(\vec{\Omega}'-\vec{\Omega},E'-E)\frac{C(\vec{\Omega}_1'-\vec{\Omega}_1,E'-E)}{C(\vec{\Omega}'-\vec{\Omega},E'-E)}\, d\tau_{P'}\, d\tau_{\Omega'}\, dE'.$$

(A-8)

Eqs. A-7 and A-8 can be solved simultaneously and in a correlated way – Eq. A-7 being solved directly, and Eq. A-8 indirectly, with ratios of source densities, transport kernels, and collision kernels being interpreted as weights. Before we describe the method of solution, let us calculate these ratios.

As we deal with an isotropic source, the source density function does not depend on $\vec{\Omega}$. As we deal with a point source at Σ, and as the line of reflection passes through the point, the ratio

$$\frac{S(\vec{P}_1,\vec{\Omega}_1,E)}{S(\vec{P},\vec{\Omega},E)}$$

needs to be evaluated only for $\vec{P}_1 = \vec{P} = \Sigma$, and is therefore equal to unity.

The transport kernel is given by

$$T(\vec{P}'-\vec{P})\,|(E) = \mu(\vec{P},E')\exp\left[-\int_0^s \mu(s,E')ds\right]$$

where the line integral is along P P′.

The ratio of transport kernels is therefore given by

$$W_1(\vec{P}'\to\vec{P})\,|\,(E') = \frac{T(\vec{P}_1'\to\vec{P}_1)\,|\,(E')}{T(\vec{P}'\to\vec{P})\,|\,(E')} = \frac{\mu(\vec{P}_1,E')\, e^{-\int_0^{s_1}\mu(s_1,E')\,ds_1}}{\mu(\vec{P},E')\, e^{-\int_0^{s}\mu(s,E')\,ds}} \qquad \text{(A-9)}$$

The collision kernel does not depend on position (since all space contains the same material). The angular dependence is on $\vec{\Omega}'\cdot\vec{\Omega}$ and, as reflection preserves angles, $\vec{\Omega}_1'\cdot\vec{\Omega}_1 = \vec{\Omega}'\cdot\vec{\Omega}$. The ratio of collision kernels is therefore

$$\frac{C(\vec{\Omega}_1'\to\vec{\Omega}_1,E'\to E)}{C(\vec{\Omega}'\to\vec{\Omega},E'\to E)} = 1.$$

Let us introduce the notation

$$\psi_1(\vec{P},\vec{\Omega},E) = \psi(\vec{P}_1,\vec{\Omega}_1,E)$$

where $\vec{P}_1$, $\vec{\Omega}_1$ are mirror images of $\vec{P}, \vec{\Omega}$.

Using all the results obtained, we can rewrite Eq. A-8 as

$$\psi_1(\vec{P},\vec{\Omega},E) = S(\vec{P},\vec{\Omega},E) + \int \psi_1(\vec{P}',\vec{\Omega}',E')\, T(\vec{P}'\to\vec{P}\,|\,E')\, W_1(\vec{P}'\to\vec{P}\,|\,E')C(\vec{\Omega}'\to\vec{\Omega},E'\to E)\cdot$$

$$\cdot\, d\tau_{P'}\, d\tau_{\Omega'}\, dE' \qquad \text{(A-10)}$$

where W_1 is given by Eq. A-9.

Eq. A-6 can be rewritten in the form

$$\overline{F}(\vec{D},E) = \int \vec{\Omega}\cdot\vec{u}\, \left[\frac{\psi(\vec{D},\vec{\Omega},E) - \psi_1(\vec{D},\vec{\Omega},E)}{2}\right] d\tau_\Omega \qquad \text{(A-11)}$$

Eq. A-10 can be solved by using the kernels $T(\vec{P}'\to\vec{P}\,|\,E')$ and $C(\vec{\Omega}'\to\Omega,E'\to E)$, and by evaluating the cumulative product of weights $W_1(P'\to P\,|\,E')$ giving a total weight

$W(\vec{P},\vec{\Omega},E)$. In this sense we can redefine ψ_1 as

$$\psi_1(\vec{P},\vec{\Omega},E) = \psi(\vec{P},\vec{\Omega},E)\, W(\vec{P},\vec{\Omega},E) \tag{A-12}$$

and rewrite Eq. A-12 in the form

$$\overline{F}(\vec{D},E) = \int \vec{\Omega}\cdot\vec{u} \left[\frac{1-W(\vec{D},\vec{\Omega},E)}{2}\right] \psi(\vec{D},\vec{\Omega},E)\, d\tau_\Omega \tag{A-13}$$

A.4 LIMITATIONS OF THE METHOD

We have shown that the method of antithetic correlation reduces the variance of Eq. A-3 if the one-dimensional analogue is satisfied. In the actual problem, this corresponds to

$$W(\vec{D},\vec{\Omega},E) \approx 1.$$

This is actually only a sufficient condition. It corresponds to the case of a nearly homogeneous atmosphere. The complete condition is

$$\int (\vec{\Omega}\cdot\vec{u})^2 \left[\frac{1-W(\vec{D},\vec{\Omega},E)}{2}\right]^2 \psi(\vec{D},\vec{\Omega},E)\, d\tau_\Omega << \int (\vec{\Omega}\cdot\vec{u})^2\, \psi(\vec{D},\vec{\Omega},E)\, d\tau_\Omega.$$

We suspect, and we have shown by actual numerical calculations, that the method does indeed lead to improved statistics for rather highly varying atmospheric density. It is clear, however, that the method should fail for some large enough variation of the atmospheric density. Indeed, we can show that it can lead to an infinite variance, i. e., to

$$\int [W(\vec{D},\vec{\Omega},E)]^2\, \psi(\vec{D},\vec{\Omega},E)\, d\tau_\Omega$$

diverging. This is easiest to show on a simple one-dimensional analogue.

Let us consider the case

$$\psi = \mu e^{-\mu r}$$

$$W = \frac{\mu_1 e^{-\mu_1 r}}{\mu e^{-\mu r}}$$

and the integral

$$\int_0^\infty W^2 \psi \, d\tau = \int_0^\infty \frac{\mu_1^2 e^{-2\mu_1 r}}{\mu^2 e^{-2\mu r}} \mu e^{-\mu r} \, dr = \int_0^\infty \frac{\mu_1^2}{\mu} e^{-(2\mu_1 - \mu) r} \, dr$$

The integral clearly diverges for $2\mu_1 \leq \mu$.

In the actual problem, this indicates high variance in the case where the normal history traverses regions of density much higher than the mirror's history, or, in other words, in regions of high density gradient. It is comforting to realize that in these regions the direct Monte Carlo approach is expected to work at its best.

A.5 CONCLUSION

We have indicated the desirability of introducing antithetic correlation in estimating the polar component of flux of radiation in the atmosphere.

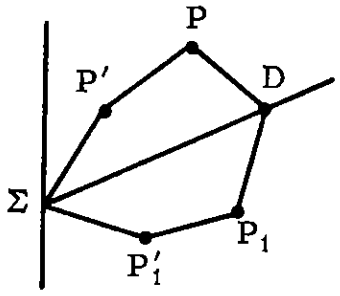

We have shown that a way of achieving this was to generate, by normal Monte Carlo methods, points coming out of collision, with density $\psi(\vec{P}, \vec{\Omega}, E)$, as

well as a set of corresponding weights $W(\vec{P},\vec{\Omega},E)$ generated by computing the cumulative product of factors W_1 given by Eq. A-9 for each flight path. The corresponding estimator is given by Eq. A-13.

This page intentionally left blank.

APPENDIX B – AVERAGE FORWARD ELECTRON RANGE IN AIR

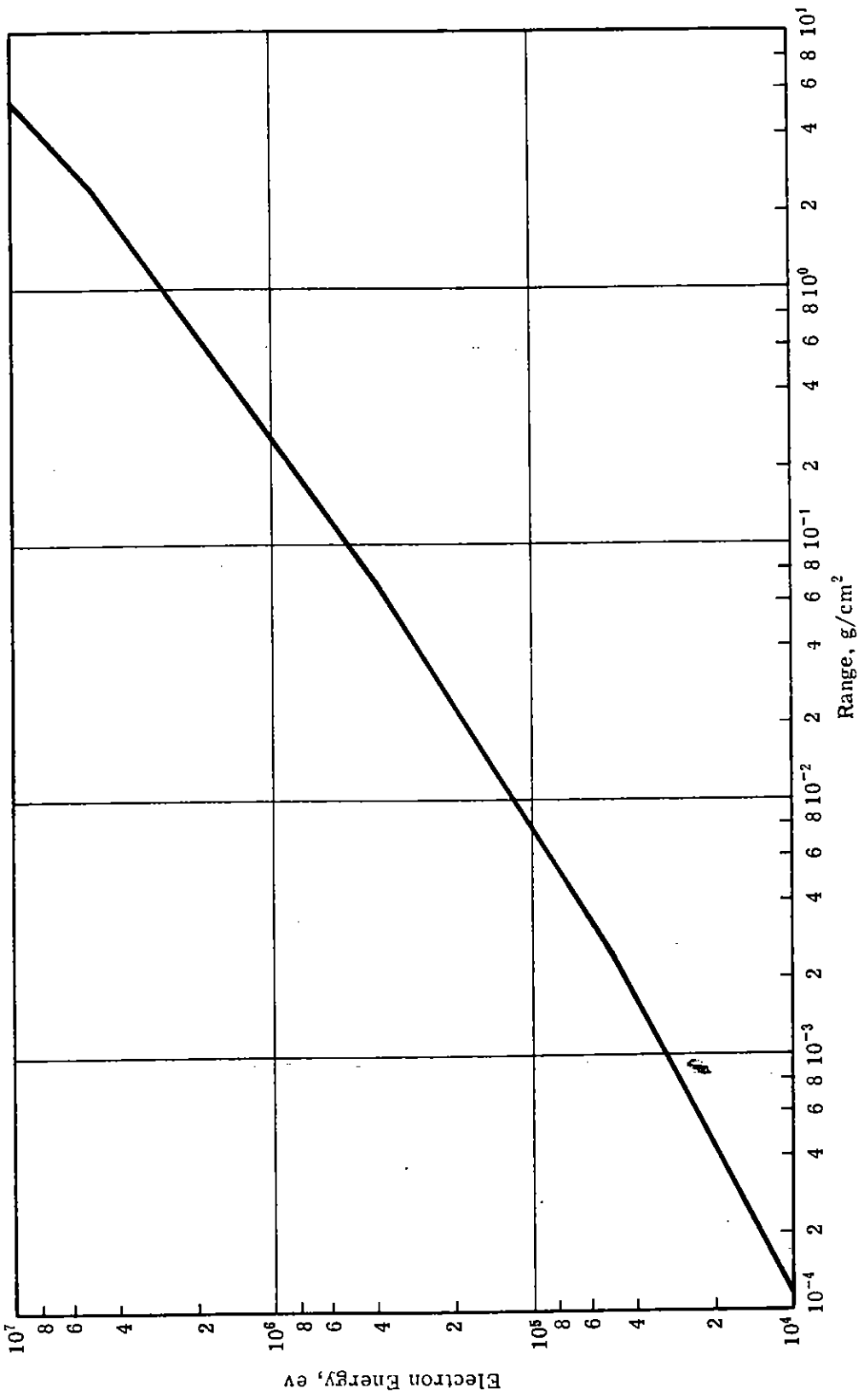

Fig. 63 — Average Forward Electron Range in Air (as Used by Program CORREDIT)

APPENDIX C – CORSAIR AIR DENSITY TABLE

CORSAIR AIR DENSITY TABLE

ALTITUDE (KM.)	AIR DENSITY (GM/CM3)
0	1.2250E-03
2	1.0066E-03
4	8.1935E-04
6	6.6011E-04
8	5.2579E-04
10	4.1351E-04
12	3.1194E-04
14	2.2786E-04
16	1.6647E-04
18	1.2165E-04
20	8.8915E-05
22	6.4515E-05
24	4.6978E-05
26	3.4257E-05
28	2.5076E-05
30	1.8410E-05
32	1.3555E-05
34	9.8874E-06
36	7.2579E-06
38	5.3666E-06
40	3.9957E-06
42	2.9948E-06
44	2.2589E-06
46	1.7141E-06
48	1.3167E-06
50	1.0269E-06
52	8.0097E-07
54	6.3137E-07
56	4.9762E-07
58	3.9086E-07
60	3.0592E-07
62	2.3931E-07
64	2.0013E-07
66	1.5663E-07
68	1.2160E-07
70	8.7535E-08
72	6.6593E-08
74	5.0151E-08
76	3.7360E-08
78	2.75 0E-08
80	1.0990E-08
82	1.3820E-08
84	9.5630E-09
86	6.4170E-09
88	4.5790E-09
90	3.17 0E-09
92	2.1370E-09
94	1.4590E-09
96	1.0280E-09
98	7.0440E-10
100	4.9740E-10

APPENDIX D – NEUTRON CROSS SECTIONS

NEUTRON CROSS SECTIONS (barns/atom)

	NITROGEN			OXYGEN		
ENERGY	TOTAL*	N,NPRIME	ABSORP.	TOTAL*	N,NPRIME	ABSORP.
3.841E-06	1.035E+01	0	3.675E-01	2.496E+00	0	8.561E-03
3.957E-06	1.049E+01	0	3.771E-01	2.422E+00	0	1.053E-02
3.974E-06	1.048E+01	0	3.956E-01	2.352E+00	0	1.308E-02
3.991E-06	1.057E+01	0	3.944E-01	2.287E+00	0	1.574E-02
3.908E-06	1.071E+01	0	4.019E-01	2.224E+00	0	1.927E-02
3.925E-06	1.089E+01	0	4.110E-01	2.214E+00	0	2.340E-02
3.942E-06	1.095E+01	0	4.174E-01	2.174E+00	0	2.878E-02
3.959E-06	1.091E+01	1.781E-04	4.253E-01	2.124E+00	0	3.475E-02
3.976E-06	1.077E+01	5.214E-04	4.214E-01	2.094E+00	0	4.241E-02
3.993E-06	1.060E+01	8.661E-04	4.412E-01	2.094E+00	0	5.153E-02
4.011E-06	2.020E+01	1.212E-03	4.532E-01	1.954E+00	0	6.270E-02
4.028E-06	2.054E+01	1.560E-03	4.734E-01	1.761E+00	0	7.076E-02
4.045E-06	2.088E+01	1.909E-03	4.823E-01	1.451E+00	0	7.347E-02
4.063E-06	2.132E+01	2.541E-03	4.976E-01	1.291E+00	0	7.572E-02
4.081E-06	2.102E+01	3.539E-03	5.198E-01	1.168E+00	0	7.813E-02
4.098E-06	2.129E+01	4.848E-03	5.210E-01	1.110E+00	0	8.062E-02
4.116E-06	2.142E+01	5.622E-03	5.153E-01	1.100E+00	0	8.322E-02
4.134E-06	2.157E+01	6.067E-03	5.122E-01	1.238E+00	0	8.596E-02
4.152E-06	2.174E+01	6.204E-03	4.937E-01	1.492E+00	0	8.883E-02
4.170E-06	2.192E+01	6.345E-03	4.924E-01	1.851E+00	0	9.185E-02
4.188E-06	2.188E+01	6.488E-03	4.856E-01	1.993E+00	0	9.448E-02
4.206E-06	2.182E+01	6.634E-03	4.817E-01	2.043E+00	0	9.753E-02
4.224E-06	2.171E+01	6.784E-03	4.809E-01	1.932E+00	0	9.936E-02
4.243E-06	2.099E+01	6.937E-03	4.717E-01	1.644E+00	0	9.371E-02
4.261E-06	2.015E+01	7.043E-03	4.658E-01	1.439E+00	0	8.615E-02
4.279E-06	1.976E+01	7.115E-03	4.565E-01	1.480E+00	0	7.923E-02
4.298E-06	1.876E+01	7.188E-03	4.485E-01	1.875E+00	0	7.277E-02
4.317E-06	1.821E+01	7.261E-03	4.417E-01	2.538E+00	0	6.685E-02
4.335E-06	1.749E+01	7.335E-03	4.311E-01	2.899E+00	0	6.140E-02
4.354E-06	1.700E+01	7.411E-03	4.230E-01	2.724E+00	0	5.642E-02
4.373E-06	1.691E+01	7.486E-03	4.161E-01	2.325E+00	0	5.184E-02
4.392E-06	1.674E+01	7.563E-03	4.079E-01	2.197E+00	0	4.764E-02
4.411E-06	1.654E+01	7.640E-03	3.983E-01	2.065E+00	0	4.377E-02
4.430E-06	1.653E+01	7.718E-03	3.927E-01	1.859E+00	0	4.022E-02
4.449E-06	1.646E+01	7.797E-03	3.909E-01	1.690E+00	0	3.696E-02
4.469E-06	1.627E+01	7.837E-03	3.978E-01	1.499E+00	0	3.394E-02
4.488E-06	1.612E+01	7.876E-03	4.091E-01	1.281E+00	0	3.984E-02
4.508E-06	1.604E+01	7.915E-03	4.203E-01	1.281E+00	0	4.062E-02
4.527E-06	1.625E+01	7.954E-03	4.350E-01	1.479E+00	0	4.149E-02
4.547E-06	1.601E+01	7.993E-03	4.461E-01	1.757E+00	0	4.234E-02
4.566E-06	1.534E+01	8.065E-03	4.514E-01	1.324E+00	0	4.322E-02
4.586E-06	1.513E+01	8.144E-03	4.610E-01	1.2[illegible]E+00	0	4.408E-02
4.606E-06	1.495E+01	8.224E-03	4.656E-01	1.4[illegible]E+00	0	4.494E-02
4.626E-06	1.456E+01	8.304E-03	4.693E-01	1.1[illegible]E+00	0	4.590E-02
4.646E-06	1.405E+01	8.468E-03	4.498E-01	1.464E+00	0	4.684E-02
4.666E-06	1.342E+01	8.565E-03	4.342E-01	1.102E+00	0	4.789E-02
4.686E-06	1.282E+01	8.646E-03	3.872E-01	1.027E+00	0	5.059E-02
4.707E-06	1.227E+01	8.749E-03	3.546E-01	9.828E-01	0	5.409E-02
4.727E-06	1.180E+01	8.862E-03	3.289E-01	9.394E-01	0	5.785E-02
4.748E-06	1.133E+01	8.986E-03	3.099E-01	9.045E-01	0	6.183E-02

*$\sigma_T = \sigma_{n,n'} + \sigma_a + \sigma_e$.

NEUTRON CROSS-SECTIONS

	NITROGEN			OXYGEN		
ENERGY	TOTAL	N,NPRIME	ABSORP.	TOTAL	N,NPRIME	ABSORP.
4.788E 6	1.[illegible]	9.354E-03	3.026E-01	8.464E-01	0	8.612E-02
4.789E 6	1.[illegible]	9.116E-03	3.003E-01	8.630E-01	0	7.867E-02
4.810E 6	9.925E-01	9.179E-03	2.941E-01	1.016E 00	0	7.553E-02
4.831E 6	9.882E-01	9.241E-03	2.940E-01	1.374E 00	0	8.176E-02
4.851E 6	9.870E-01	9.324E-03	2.928E-01	1.783E 00	0	8.635E-02
4.873E 6	9.915E-01	9.467E-03	2.961E-01	1.450E 00	0	9.236E-02
4.894E 6	1.[illegible]	1.002E-02	2.994E-01	1.244E 00	0	9.663E-02
4.915E 6	1.[illegible]	1.039E-02	3.041E-01	1.094E 00	0	1.014E-01
4.936E 6	1.[illegible]	1.078E-02	3.084E-01	9.692E-01	0	9.824E-02
4.956E 6	1.[illegible]	1.117E-02	3.143E-01	8.815E-01	0	9.371E-02
4.979E 6	1.[illegible]	1.159E-02	3.180E-01	8.431E-01	0	8.938E-02
5.001E 6	1.213E 00	1.202E-02	3.218E-01	8.910E-01	0	8.530E-02
5.022E 6	1.291E 00	1.290E-02	3.324E-01	9.818E-01	0	8.152E-02
5.044E 6	1.335E 00	1.383E-02	3.401E-01	1.196E 00	0	7.784E-02
5.066E 6	1.341E 00	1.413E-02	3.424E-01	1.457E 00	0	7.414E-02
5.086E 6	1.343E 00	1.418E-02	3.388E-01	1.740E 00	0	7.068E-02
5.110E 6	1.395E 00	1.491E-02	3.288E-01	2.475E 00	0	6.737E-02
5.132E 6	1.436E 00	1.661E-02	3.138E-01	2.960E 00	0	6.432E-02
5.154E 6	1.479E 00	1.851E-02	2.992E-01	2.041E 00	0	6.138E-02
5.177E 6	1.490E 00	2.062E-02	2.810E-01	1.499E 00	0	5.826E-02
5.199E 6	1.492E 00	2.298E-02	2.659E-01	1.236E 00	0	4.433E-02
5.222E 6	1.481E 00	2.560E-02	2.517E-01	1.174E 00	0	3.678E-02
5.244E 6	1.466E 00	2.852E-02	2.380E-01	1.138E 00	0	3.048E-02
5.267E 6	1.454E 00	2.976E-02	2.261E-01	1.089E 00	0	2.527E-02
5.290E 6	1.449E 00	3.037E-02	2.162E-01	1.025E 00	0	2.095E-02
5.313E 6	1.447E 00	3.101E-02	2.036E-01	9.517E-01	0	1.737E-02
5.336E 6	1.467E 00	3.165E-02	1.966E-01	1.000E 00	0	1.447E-02
5.359E 6	1.486E 00	3.231E-02	1.913E-01	1.282E 00	0	1.202E-02
5.382E 6	1.464E 00	3.298E-02	1.794E-01	1.040E 00	0	9.884E-03
5.406E 6	1.451E 00	3.370E-02	1.725E-01	8.734E-01	0	8.[illegible]E-03
5.429E 6	1.468E 00	3.457E-02	1.769E-01	8.890E-01	0	7.[illegible]E-03
5.453E 6	1.464E 00	3.545E-02	1.802E-01	9.251E-01	0	9.[illegible]E-03
5.476E 6	1.430E 00	3.636E-02	1.832E-01	9.723E-01	0	1.149E-02
5.500E 6	1.434E 00	3.730E-02	1.887E-01	1.020E 00	0	1.461E-02
5.524E 6	1.469E 00	3.730E-02	1.977E-01	1.073E 00	0	1.857E-02
5.548E 6	1.480E 00	3.730E-02	2.070E-01	1.232E 00	0	2.362E-02
5.572E 6	1.481E 00	3.730E-02	2.176E-01	1.514E 00	0	3.003E-02
5.596E 6	1.475E 00	3.730E-02	2.218E-01	1.677E 00	0	3.818E-02
5.620E 6	1.469E 00	3.782E-02	2.290E-01	1.754E 00	0	4.856E-02
5.645E 6	1.399E 00	3.846E-02	2.172E-01	1.744E 00	0	6.184E-02
5.669E 6	1.338E 00	4.056E-02	2.068E-01	1.610E 00	0	7.854E-02
5.694E 6	1.346E 00	4.323E-02	2.084E-01	1.489E 00	0	9.998E-02
5.719E 6	1.350E 00	4.604E-02	2.056E-01	1.381E 00	0	1.046E-01
5.743E 6	1.339E 00	4.912E-02	2.028E-01	1.293E 00	0	9.589E-02
5.768E 6	1.323E 00	5.314E-02	2.026E-01	1.192E 00	0	8.717E-02
5.793E 6	1.391E 00	5.782E-02	2.060E-01	1.125E 00	0	7.923E-02
5.818E 6	1.389E 00	6.291E-02	2.096E-01	1.103E 00	0	7.222E-02
5.843E 6	1.339E 00	6.845E-02	2.135E-01	1.119E 00	0	6.646E-02
5.869E 6	1.365E 00	6.690E-02	2.200E-01	1.179E 00	0	6.950E-02
5.894E 6	1.365E 00	6.291E-02	2.259E-01	1.757E 00	0	8.412E-02

NEUTRON CROSS-SECTIONS

	NITROGEN			OXYGEN		
ENERGY	TOTAL	N,NPRIME	ABSORP.	TOTAL	N,NPRIME	ABSORP.
5.220E 06	1.397E 00	6.644E-02	2.298E-01	1.819E 00	0	4.914E-02
5.345E 06	1.434E 00	7.267E-02	2.353E-01	1.847E 00	0	4.466E-02
5.471E 06	1.429E 00	7.949E-02	2.324E-01	8.588E-01	0	4.064E-02
5.597E 06	1.432E 00	8.695E-02	2.275E-01	1.248E 00	0	3.772E-02
6.023E 06	1.447E 00	9.073E-02	2.215E-01	1.018E 00	0	3.681E-02
6.149E 06	1.454E 00	9.484E-02	2.145E-01	9.750E-01	0	4.081E-02
6.275E 06	1.487E 00	9.756E-02	2.152E-01	1.162E 00	0	4.304E-02
6.402E 06	1.483E 00	1.000E-01	2.164E-01	1.092E 00	0	4.534E-02
6.528E 06	1.467E 00	1.022E-01	2.191E-01	1.015E 00	0	4.771E-02
6.655E 06	1.477E 00	1.045E-01	2.328E-01	9.567E-01	0	5.027E-02
6.781E 06	1.444E 00	1.069E-01	2.473E-01	9.005E-01	0	5.297E-02
6.908E 06	1.383E 00	1.092E-01	2.549E-01	8.622E-01	0	5.578E-02
7.035E 06	1.310E 00	1.112E-01	2.605E-01	8.582E-01	0	5.876E-02
7.162E 06	1.330E 00	1.133E-01	2.681E-01	8.753E-01	0	6.191E-02
7.289E 06	1.397E 00	1.154E-01	2.744E-01	8.609E-01	1.868E-06	6.521E-02
7.416E 06	1.406E 00	1.171E-01	2.402E-01	8.720E-01	2.065E-04	6.817E-02
7.544E 06	1.387E 00	1.198E-01	1.879E-01	9.987E-01	5.488E-04	7.073E-02
7.671E 06	1.360E 00	1.230E-01	1.697E-01	1.318E 00	8.926E-04	7.325E-02
7.799E 06	1.388E 00	1.254E-01	1.694E-01	1.418E 00	1.238E-03	7.629E-02
8.427E 06	1.275E 00	1.274E-01	1.723E-01	9.432E-01	1.585E-03	7.986E-02
8.555E 06	1.247E 00	1.295E-01	1.758E-01	7.300E-01	1.933E-03	8.151E-02
8.683E 06	1.253E 00	1.315E-01	1.798E-01	6.508E-01	2.283E-03	8.445E-02
8.811E 06	1.279E 00	1.335E-01	1.840E-01	6.417E-01	2.634E-03	8.748E-02
8.939E 06	1.285E 00	1.354E-01	1.864E-01	7.116E-01	3.082E-03	9.072E-02
9.067E 06	1.281E 00	1.373E-01	1.898E-01	8.837E-01	4.407E-03	9.392E-02
9.196E 06	1.248E 00	1.393E-01	1.955E-01	9.509E-01	6.451E-03	9.727E-02
9.324E 06	1.206E 00	1.404E-01	1.795E-01	9.804E-01	9.276E-03	9.992E-02
9.453E 06	1.216E 00	1.415E-01	1.802E-01	1.041E 00	1.170E-02	9.889E-02
9.582E 06	1.242E 00	1.427E-01	1.808E-01	1.012E 00	1.416E-02	9.621E-02
9.711E 06	1.254E 00	1.439E-01	1.719E-01	9.930E-01	1.713E-02	9.357E-02
9.840E 06	1.192E 00	1.445E-01	1.627E-01	1.069E 00	2.072E-02	9.104E-02
9.969E 06	1.199E 00	1.452E-01	1.579E-01	1.295E 00	2.507E-02	8.853E-02
1.010E 07	1.217E 00	1.375E-01	1.620E-01	1.458E 00	3.033E-02	8.619E-02
1.023E 07	1.234E 00	1.375E-01	1.627E-01	1.194E 00	3.641E-02	8.375E-02
1.036E 07	1.176E 00	1.375E-01	1.677E-01	9.320E-01	4.210E-02	8.156E-02
1.049E 07	1.166E 00	1.375E-01	1.752E-01	8.727E-01	4.823E-02	7.926E-02
1.062E 07	1.168E 00	1.375E-01	1.835E-01	8.612E-01	5.525E-02	7.709E-02
1.075E 07	1.179E 00	1.375E-01	1.883E-01	8.618E-01	6.329E-02	7.497E-02
1.088E 07	1.194E 00	1.375E-01	1.908E-01	8.932E-01	7.121E-02	7.432E-02
1.101E 07	1.232E 00	1.375E-01	1.938E-01	9.689E-01	7.705E-02	7.634E-02
1.114E 07	1.294E 00	1.375E-01	1.992E-01	1.051E 00	8.319E-02	7.853E-02
1.127E 07	1.345E 00	1.375E-01	2.060E-01	1.103E 00	8.982E-02	8.078E-02
1.140E 07	1.378E 00	1.375E-01	2.121E-01	1.108E 00	9.698E-02	8.310E-02
1.153E 07	1.389E 00	1.375E-01	2.165E-01	1.107E 00	1.047E-01	8.557E-02
1.166E 07	1.401E 00	1.292E-01	2.257E-01	1.444E 00	1.121E-01	8.827E-02
1.192E 07	1.421E 00	1.292E-01	2.300E-01	1.634E 00	1.185E-01	9.049E-02
1.223E 07	1.456E 00	1.292E-01	2.418E-01	1.481E 00	1.249E-01	9.389E-02
1.254E 07	1.487E 00	1.292E-01	2.529E-01	1.371E 00	1.318E-01	9.573E-02
1.286E 07	1.505E 00	1.292E-01	2.602E-01	1.300E 00	1.391E-01	9.847E-02
1.317E 07	1.522E 00	1.292E-01	2.629E-01	1.267E 00	1.469E-01	1.009E-01

NEUTRON CROSS-SECTIONS

	NITROGEN			OXYGEN		
ENERGY	TOTAL	N,nPRIME	ABSORP.	TOTAL	N,nPRIME	ABSORP.
7.140E 6	1.533E [illegible]	1.292E-01	2.511E-01	1.25AE 00	1.578E-01	9.736E-02
7.341E 6	1.540E [illegible]	1.292E-01	2.447E-01	1.265E 00	1.714E-01	9.155E-02
7.413E 6	1.529E [illegible]	1.292E-01	2.511E-01	1.247E 00	1.824E-01	8.814E-02
7.445E 6	1.518E [illegible]	1.292E-01	2.604E-01	1.154E 00	1.887E-01	8.099E-02
7.477E 6	1.479E [illegible]	1.292E-01	2.431E-01	1.09AE 00	1.951E-01	7.612E-02
7.510E 6	1.441E [illegible]	1.292E-01	2.266E-01	1.090E 00	2.018E-01	7.150E-02
7.542E 6	1.420E [illegible]	1.401E-01	2.136E-01	1.104E 00	2.057E-01	6.728E-02
7.575E 6	1.402E [illegible]	1.407E-01	2.049E-01	1.127E 00	2.158E-01	6.325E-02
7.608E 6	1.382E [illegible]	1.747E-01	2.008E-01	1.144E 00	2.262E-01	5.947E-02
7.641E 6	1.341E [illegible]	2.052E-01	2.034E-01	1.160E 00	2.308E-01	5.591E-02
7.674E 6	1.341E [illegible]	2.150E-01	2.119E-01	1.194E 00	2.387E-01	5.250E-02
7.707E 6	1.381E [illegible]	2.155E-01	2.153E-01	1.227E 00	2.436E-01	5.939E-02
7.741E 6	1.397E [illegible]	2.161E-01	2.201E-01	1.255E 00	2.400E-01	5.196E-02
7.774E 6	1.408E [illegible]	2.169E-01	2.261E-01	1.325E 00	2.360E-01	5.197E-02
7.808E 6	1.423E [illegible]	2.178E-01	2.309E-01	1.382E 00	2.321E-01	5.289E-02
7.842E 6	1.472E [illegible]	2.187E-01	2.412E-01	1.411E 00	2.282E-01	5.383E-02
7.876E 6	1.518E [illegible]	2.202E-01	2.622E-01	1.361E 00	2.245E-01	5.486E-02
7.910E 6	1.469E [illegible]	2.216E-01	2.630E-01	1.209E 00	2.214E-01	5.583E-02
7.944E 6	1.405E [illegible]	2.239E-01	2.699E-01	1.031E 00	2.183E-01	5.684E-02
7.979E 6	1.398E [illegible]	2.262E-01	2.745E-01	9.089E-01	2.153E-01	5.778E-02
8.013E 6	1.394E [illegible]	2.252E-01	2.763E-01	8.676E-01	2.123E-01	5.879E-02
8.048E 6	1.342E [illegible]	2.243E-01	2.668E-01	8.645E-01	2.093E-01	5.989E-02
8.083E 6	1.276E [illegible]	2.234E-01	2.592E-01	9.349E-01	2.064E-01	6.087E-02
8.118E 6	1.242E [illegible]	2.226E-01	2.538E-01	1.051E 00	2.095E-01	6.124E-02
8.153E 6	1.241E [illegible]	2.211E-01	2.487E-01	1.135E 00	2.184E-01	6.116E-02
8.188E 6	1.239E [illegible]	2.197E-01	2.450E-01	1.224E 00	2.277E-01	6.112E-02
8.224E 6	1.229E [illegible]	2.182E-01	2.429E-01	1.289E 00	2.374E-01	6.106E-02
8.260E 6	1.220E [illegible]	2.167E-01	2.422E-01	1.334E 00	2.476E-01	6.100E-02
8.295E 6	1.208E [illegible]	2.151E-01	2.427E-01	1.34AE 00	2.582E-01	6.094E-02
8.331E 6	1.195E [illegible]	2.126E-01	2.450E-01	1.341E 00	2.692E-01	6.[illegible]E-02
8.367E 6	1.202E [illegible]	2.095E-01	2.480E-01	1.303E 00	2.816E-01	6.[illegible]E-02
8.404E 6	1.226E [illegible]	2.065E-01	2.511E-01	1.242E 00	2.955E-01	6.077E-02
8.440E 6	1.244E [illegible]	2.049E-01	2.549E-01	1.172E 00	3.102E-01	6.070E-02
8.477E 6	1.233E [illegible]	2.034E-01	2.542E-01	1.109E 00	3.255E-01	6.064E-02
8.513E 6	1.223E [illegible]	2.018E-01	2.532E-01	1.066E 00	3.384E-01	6.059E-02
8.550E 6	1.234E [illegible]	2.002E-01	2.551E-01	1.04AE 00	3.383E-01	6.117E-02
8.587E 6	1.247E [illegible]	1.986E-01	2.541E-01	1.050E 00	3.367E-01	6.171E-02
8.625E 6	1.274E [illegible]	1.970E-01	2.559E-01	1.087E 00	3.351E-01	6.225E-02
8.662E 6	1.308E [illegible]	1.954E-01	2.586E-01	1.157E 00	3.336E-01	6.279E-02
8.700E 6	1.308E [illegible]	1.938E-01	2.611E-01	1.254E 00	3.320E-01	6.335E-02
8.737E 6	1.280E [illegible]	1.922E-01	2.638E-01	1.339E 00	3.307E-01	6.388E-02
8.775E 6	1.265E [illegible]	1.906E-01	2.665E-01	1.323E 00	3.293E-01	6.444E-02
8.813E 6	1.274E [illegible]	1.890E-01	2.700E-01	1.259E 00	3.279E-01	6.501E-02
8.851E 6	1.282E [illegible]	1.875E-01	2.762E-01	1.14AE 00	3.268E-01	6.561E-02
8.890E 6	1.265E [illegible]	1.859E-01	2.764E-01	1.07AE 00	3.261E-01	6.618E-02
8.928E 6	1.247E [illegible]	1.844E-01	2.796E-01	1.044E 00	3.254E-01	6.678E-02
8.967E 6	1.253E [illegible]	1.828E-01	2.829E-01	1.05AE 00	3.250E-01	6.741E-02
9.006E 6	1.273E [illegible]	1.810E-01	2.857E-01	1.09AE 00	3.250E-01	6.838E-02
9.045E 6	1.293E [illegible]	1.792E-01	2.885E-01	1.183E 00	3.250E-01	6.912E-02
9.084E 6	1.316E [illegible]	1.775E-01	2.915E-01	1.227E 00	3.250E-01	6.986E-02

NEUTRON CROSS-SECTIONS

ENERGY	NITROGEN TOTAL	NITROGEN N,NPRIME	NITROGEN ABSORP.	OXYGEN TOTAL	OXYGEN N,NPRIME	OXYGEN ABSORP.
9.124E 6	1.339E 00	1.758E-01	2.998E-01	1.173E 00	3.250E-01	7.980E-02
9.163E 6	1.329E 00	1.741E-01	2.977E-01	1.170E 00	3.250E-01	7.137E-02
9.203E 6	1.301E 00	1.724E-01	3.108E-01	1.023E 00	3.250E-01	7.191E-02
9.243E 6	1.300E 00	1.707E-01	3.047E-01	1.007E 00	3.250E-01	7.244E-02
9.283E 6	1.306E 00	1.690E-01	3.183E-01	1.059E 00	3.250E-01	7.274E-02
9.323E 6	1.316E 00	1.674E-01	3.127E-01	1.092E 00	3.250E-01	7.347E-02
9.364E 6	1.314E 00	1.658E-01	3.161E-01	1.094E 00	3.250E-01	7.455E-02
9.404E 6	1.312E 00	1.642E-01	3.205E-01	1.102E 00	3.251E-01	7.566E-02
9.445E 6	1.299E 00	1.654E-01	3.226E-01	1.113E 00	3.258E-01	7.657E-02
9.486E 6	1.280E 00	1.672E-01	3.254E-01	1.124E 00	3.267E-01	7.726E-02
9.527E 6	1.287E 00	1.689E-01	3.269E-01	1.138E 00	3.279E-01	7.773E-02
9.568E 6	1.349E 00	1.707E-01	3.292E-01	1.150E 00	3.294E-01	7.802E-02
9.610E 6	1.415E 00	1.725E-01	3.394E-01	1.167E 00	3.308E-01	7.851E-02
9.651E 6	1.415E 00	1.743E-01	3.372E-01	1.175E 00	3.325E-01	7.957E-02
9.693E 6	1.407E 00	1.762E-01	3.403E-01	1.188E 00	3.338E-01	8.063E-02
9.735E 6	1.399E 00	1.780E-01	3.435E-01	1.201E 00	3.354E-01	8.143E-02
9.777E 6	1.390E 00	1.799E-01	3.468E-01	1.213E 00	3.371E-01	8.213E-02
9.820E 6	1.381E 00	1.818E-01	3.476E-01	1.222E 00	3.384E-01	8.291E-02
9.862E 6	1.393E 00	1.837E-01	3.522E-01	1.226E 00	3.394E-01	8.378E-02
9.905E 6	1.405E 00	1.845E-01	3.555E-01	1.231E 00	3.411E-01	8.421E-02
9.948E 6	1.416E 00	1.831E-01	3.587E-01	1.236E 00	3.442E-01	8.466E-02
9.991E 6	1.427E 00	1.816E-01	3.608E-01	1.240E 00	3.473E-01	8.510E-02
1.003E 7	1.439E 00	1.802E-01	3.629E-01	1.254E 00	3.490E-01	8.377E-02
1.008E 7	1.449E 00	1.788E-01	3.650E-01	1.271E 00	3.503E-01	8.171E-02
1.012E 7	1.459E 00	1.774E-01	3.676E-01	1.291E 00	3.517E-01	8.046E-02
1.017E 7	1.459E 00	1.761E-01	3.694E-01	1.313E 00	3.530E-01	8.001E-02
1.021E 7	1.457E 00	1.747E-01	3.716E-01	1.326E 00	3.543E-01	7.998E-02
1.025E 7	1.455E 00	1.734E-01	3.738E-01	1.314E 00	3.556E-01	8.127E-02
1.030E 7	1.453E 00	1.720E-01	3.762E-01	1.29AE 00	3.570E-01	8.283E-02
1.034E 7	1.452E 00	1.707E-01	3.801E-01	1.269E 00	3.583E-01	8.421E-02
1.039E 7	1.427E 00	1.694E-01	3.802E-01	1.239E 00	3.596E-01	8.931E-02
1.043E 7	1.399E 00	1.682E-01	3.822E-01	1.217E 00	3.602E-01	9.108E-02
1.048E 7	1.383E 00	1.670E-01	3.839E-01	1.199E 00	3.609E-01	9.227E-02
1.052E 7	1.391E 00	1.659E-01	3.861E-01	1.183E 00	3.612E-01	9.325E-02
1.057E 7	1.399E 00	1.648E-01	3.876E-01	1.169E 00	3.622E-01	9.403E-02
1.062E 7	1.413E 00	1.637E-01	3.896E-01	1.158E 00	3.633E-01	9.490E-02
1.066E 7	1.428E 00	1.626E-01	3.914E-01	1.142E 00	3.644E-01	9.605E-02
1.071E 7	1.433E 00	1.615E-01	3.943E-01	1.131E 00	3.655E-01	9.714E-02
1.075E 7	1.418E 00	1.604E-01	3.949E-01	1.135E 00	3.666E-01	9.854E-02
1.080E 7	1.387E 00	1.593E-01	3.968E-01	1.161E 00	3.677E-01	1.002E-01
1.085E 7	1.373E 00	1.582E-01	3.969E-01	1.197E 00	3.688E-01	1.021E-01
1.089E 7	1.364E 00	1.571E-01	4.006E-01	1.234E 00	3.698E-01	1.040E-01
1.094E 7	1.356E 00	1.558E-01	4.005E-01	1.308E 00	3.702E-01	1.074E-01
1.099E 7	1.349E 00	1.544E-01	4.040E-01	1.382E 00	3.704E-01	1.099E-01
1.104E 7	1.382E 00	1.530E-01	4.054E-01	1.473E 00	3.711E-01	1.125E-01
1.108E 7	1.394E 00	1.516E-01	4.069E-01	1.567E 00	3.720E-01	1.155E-01
1.113E 7	1.405E 00	1.503E-01	4.083E-01	1.603E 00	3.730E-01	1.190E-01
1.118E 7	1.416E 00	1.489E-01	4.099E-01	1.604E 00	3.739E-01	1.229E-01
1.123E 7	1.426E 00	1.476E-01	4.114E-01	1.622E 00	3.748E-01	1.271E-01
1.128E 7	1.435E 00	1.463E-01	4.129E-01	1.613E 00	3.758E-01	1.320E-01

NEUTRON CROSS-SECTIONS

	NITROGEN			OXYGEN		
ENERGY	TOTAL	N,NPRIME	ABSORP.	TOTAL	N,NPRIME	ABSORP.
1.133E 7	1.443E 0	1.450E-01	4.151E-01	1.573E 00	3.767E-01	1.375E-01
1.138E 7	1.445E 00	1.437E-01	4.162E-01	1.550E 00	3.776E-01	1.437E-01
1.143E 7	1.447E 0	1.424E-01	4.179E-01	1.575E 00	3.786E-01	1.497E-01
1.147E 7	1.451E 00	1.411E-01	4.197E-01	1.635E 00	3.795E-01	1.557E-01
1.152E 7	1.456E 0	1.410E-01	4.205E-01	1.685E 00	3.804E-01	1.643E-01
1.157E 7	1.461E 00	1.421E-01	4.193E-01	1.680E 00	3.811E-01	1.668E-01
1.162E 7	1.476E 00	1.433E-01	4.198E-01	1.636E 00	3.818E-01	1.695E-01
1.167E 7	1.472E 0	1.444E-01	4.197E-01	1.615E 00	3.826E-01	1.723E-01
1.173E 7	1.596E 00	1.455E-01	4.202E-01	1.620E 00	3.833E-01	1.754E-01
1.178E 7	1.511E 00	1.466E-01	4.197E-01	1.623E 00	3.840E-01	1.787E-01
1.183E 7	1.516E 00	1.478E-01	4.197E-01	1.629E 00	3.848E-01	1.822E-01
1.188E 7	1.519E 00	1.490E-01	4.199E-01	1.592E 00	3.855E-01	1.868E-01
1.193E 7	1.522E 00	1.501E-01	4.201E-01	1.552E 00	3.863E-01	1.918E-01
1.198E 7	1.525E 00	1.513E-01	4.196E-01	1.513E 00	3.870E-01	1.969E-01
1.203E 7	1.534E 0	1.525E-01	4.209E-01	1.483E 00	3.882E-01	1.975E-01
1.208E 7	1.543E 00	1.537E-01	4.217E-01	1.457E 00	3.896E-01	2.013E-01
1.214E 7	1.551E 00	1.563E-01	4.218E-01	1.436E 00	3.903E-01	2.035E-01
1.219E 7	1.562E 00	1.594E-01	4.222E-01	1.438E 00	3.907E-01	2.054E-01
1.224E 7	1.554E 0	1.626E-01	4.228E-01	1.440E 00	3.911E-01	2.075E-01
1.230E 7	1.556E 00	1.659E-01	4.235E-01	1.450E 00	3.915E-01	2.096E-01
1.235E 7	1.560E 0	1.692E-01	4.242E-01	1.463E 00	3.919E-01	2.124E-01
1.240E 7	1.564E 00	1.727E-01	4.250E-01	1.468E 00	3.923E-01	2.154E-01
1.246E 7	1.560E 00	1.761E-01	4.257E-01	1.468E 00	3.927E-01	2.183E-01
1.251E 7	1.562E 00	1.797E-01	4.265E-01	1.471E 00	3.932E-01	2.213E-01
1.257E 7	1.543E 00	1.833E-01	4.271E-01	1.477E 00	3.940E-01	2.245E-01
1.262E 7	1.539E 00	1.870E-01	4.279E-01	1.484E 00	3.948E-01	2.279E-01
1.268E 7	1.536E 00	1.908E-01	4.284E-01	1.495E 00	3.956E-01	2.316E-01
1.273E 7	1.534E 00	1.936E-01	4.298E-01	1.503E 00	3.961E-01	2.364E-01
1.279E 7	1.529E 00	1.957E-01	4.305E-01	1.500E 00	3.963E-01	2.420E-01
1.284E 7	1.525E 00	1.979E-01	4.311E-01	1.521E 00	3.965E-01	2.479E-01
1.290E 7	1.521E 00	2.000E-01	4.316E-01	1.536E 00	3.967E-01	2.541E-01
1.295E 7	1.521E 00	2.022E-01	4.325E-01	1.543E 00	3.969E-01	2.604E-01
1.301E 7	1.520E 00	2.044E-01	4.332E-01	1.516E 00	3.971E-01	2.672E-01
1.306E 7	1.513E 00	2.064E-01	4.338E-01	1.487E 00	3.977E-01	2.740E-01
1.312E 7	1.499E 00	2.088E-01	4.345E-01	1.466E 00	3.982E-01	2.807E-01
1.318E 7	1.486E 00	2.111E-01	4.351E-01	1.454E 00	3.988E-01	2.879E-01
1.324E 7	1.476E 00	2.134E-01	4.355E-01	1.450E 00	3.994E-01	2.942E-01
1.329E 7	1.466E 00	2.157E-01	4.356E-01	1.450E 00	3.999E-01	3.000E-01
1.335E 7	1.457E 00	2.167E-01	4.352E-01	1.450E 00	4.000E-01	3.062E-01
1.341E 7	1.466E 00	2.176E-01	4.375E-01	1.451E 00	4.001E-01	3.119E-01
1.347E 7	1.477E 00	2.184E-01	4.378E-01	1.457E 00	4.001E-01	3.181E-01
1.352E 7	1.488E 00	2.192E-01	4.397E-01	1.465E 00	4.004E-01	3.241E-01
1.358E 7	1.485E 00	2.201E-01	4.385E-01	1.477E 00	4.010E-01	3.241E-01
1.364E 7	1.482E 00	2.209E-01	4.388E-01	1.488E 00	4.015E-01	3.281E-01
1.370E 7	1.488E 00	2.217E-01	4.352E-01	1.500E 00	4.021E-01	3.321E-01
1.376E 7	1.512E 00	2.226E-01	4.390E-01	1.500E 00	4.027E-01	3.360E-01
1.382E 7	1.544E 0	2.234E-01	4.393E-01	1.518E 00	4.033E-01	3.411E-01
1.388E 7	1.576E 00	2.243E-01	4.411E-01	1.527E 00	4.039E-01	3.457E-01
1.394E 7	1.598E 00	2.252E-01	4.393E-01	1.518E 00	4.044E-01	3.504E-01
1.400E 7	1.620E 0	2.260E-01	4.387E-01	1.500E 00	4.050E-01	3.553E-01

This page intentionally left blank.

APPENDIX E – GAMMA-RAY PRODUCTION PROBABILITIES FOR NITROGEN AND OXYGEN

GAMMA RAY PRODUCTION PROBABILITIES
FOR NITROGEN

GAMMA RAYS FROM NEUTRON CAPTURE AND CHARGED PARTICLE REACTIONS (NITROGEN)

NEUTRON ENERGY RANGE 2.5300E-02 TO 2.5400E 04 (EV)

GAMMA RAY ENERGY	PROBABILITY OF PRODUCTION
1.7500E 06	1.5700E-02
2.5000E 06	3.1900E-03
3.5000E 06	1.3940E-02
4.5000E 06	6.8000E-03
5.5000E 06	3.6100E-02
6.5000E 06	7.7000E-03
7.5000E 06	3.8000E-03
8.5000E 06	1.7000E-03
9.5000E 06	6.8000E-03
	9.5730E-02 TOTAL PRODUCTION PROBABILITY

NEUTRON ENERGY RANGE 2.5400E 04 TO 4.0000E 06 (EV)

GAMMA RAY ENERGY	PROBABILITY OF PRODUCTION
	0 TOTAL PRODUCTION PROBABILITY

NEUTRON ENERGY RANGE 4.0000E 06 TO 4.9100E 06 (EV)

GAMMA RAY ENERGY	PROBABILITY OF PRODUCTION
2.5000E 06	1.3800E-01
	1.3800E-01 TOTAL PRODUCTION PROBABILITY

NEUTRON ENERGY RANGE 4.9100E 06 TO 6.6300E 06 (EV)

GAMMA RAY ENERGY	PROBABILITY OF PRODUCTION
2.5000E 06	1.6800E-01
4.5000E 06	1.6800E-01
	3.3600E-01 TOTAL PRODUCTION PROBABILITY

NEUTRON ENERGY RANGE 6.6300E 06 TO 8.5100E 06 (EV)

GAMMA RAY EN	PROBABILITY OF PRODUCTION
3.5000E 06	9.6000E-02
4.5000E 06	1.6900E-01
5.5000E 06	2.5900E-01
6.5000E 06	9.0000E-02
	6.1400E-01 TOTAL PRODUCTION PROBABILITY

NEUTRON ENERGY RANGE 8.5100E 06 TO 1.0900E 07 (EV)

GAMMA RAY ENERGY	PROBABILITY OF PRODUCTION
2.5000E 06	4.8000E-02
3.5000E 06	8.5000E-02
4.5000E 06	1.2100E-01
5.5000E 06	1.3700E-01
6.5000E 06	1.1200E-01
	5.0300E-01 TOTAL PRODUCTION PROBABILITY

NEUTRON ENERGY RANGE 1.0900E 07 TO 1.4000E 07 (EV)

GAMMA RAY ENERGY	PROBABILITY OF PRODUCTION
2.5000E 06	2.9000E-02
3.5000E 06	1.6300E-01
4.5000E 06	1.1300E-01
5.5000E 06	4.3000E-02
6.5000E 06	1.5200E-01
	5.2000E-01 TOTAL PRODUCTION PROBABILITY

GAMMA RAYS FROM NEUTRON INELASTIC SCATTERING (NITROGEN)

NEUTRON ENERGY RANGE 1.0000E-04 TO 4.0000E 06 (EV)

GAMMA RAY ENERGY	PROBABILITY OF PRODUCTION
	0 TOTAL PRODUCTION PROBABILITY

NEUTRON ENERGY RANGE 4.0000E 06 TO 5.1600E 06 (EV)

GAMMA RAY ENERGY	PROBABILITY OF PRODUCTION
1.5000E 06	9.4000E-01
2.5000E 06	9.4000E-01
3.5000E 06	6.0000E-02
	1.9400E 00 TOTAL PRODUCTION PROBABILITY

NEUTRON ENERGY RANGE 5.1600E 06 TO 6.6300E 06 (EV)

GAMMA RAY ENERGY	PROBABILITY OF PRODUCTION
1.5000E 06	8.9300E-01
2.5000E 06	8.9300E-01
3.5000E 06	5.7000E-02
4.5000E 06	5.0000E-02
	1.8930E 00 TOTAL PRODUCTION PROBABILITY

NEUTRON ENERGY RANGE 6.6300E 06 TO 8.5100E 06 (EV)

GAMMA RAY ENERGY	PROBABILITY OF PRODUCTION
1.5000E 06	2.5000E-01
2.5000E 06	7.4600E-01
3.5000E 06	4.9600E-01
4.5000E 06	1.4000E-01
5.5000E 06	6.6000E-02
6.5000E 06	4.8000E-02
	1.7460E 00 TOTAL PRODUCTION PROBABILITY

NEUTRON ENERGY RANGE 8.5100E 06 TO 1.0900E 07 (EV)

GAMMA RAY ENERGY	PROBABILITY OF PRODUCTION
1.5000E 06	2.9600E-01
2.5000E 06	6.4700E-01
3.5000E 06	2.3900E-01
4.5000E 06	1.8500E-01
5.5000E 06	9.5000E-02
6.5000E 06	2.1000E-01
	1.6720E 00 TOTAL PRODUCTION PROBABILITY

NEUTRON ENERGY RANGE 1.0900E 07 TO 1.4000E 07 (EV)

GAMMA RAY ENERGY	PROBABILITY OF PRODUCTION
7.5000E 05	1.7200E-01
1.2500E 06	1.5400E-01
1.5000E 06	2.4000E-01
2.5000E 06	4.0300E-01
3.5000E 06	6.8000E-02
4.5000E 06	1.9900E-01
5.5000E 06	1.0500E-01
6.5000E 06	2.2500E-01
7.0000E 06	1.2500E-01
	1.6910E 00 TOTAL PRODUCTION PROBABILITY

GAMMA RAY PRODUCTION PROBABILITIES
FOR OXYGEN

GAMMA RAYS FROM NEUTRON CAPTURE AND CHARGED PARTICLE REACTIONS (OXYGEN)

NEUTRON ENERGY RANGE 1.0000E-04 TO 7.3300E 06 (EV)

GAMMA RAY ENERGY	PROBABILITY OF PRODUCTION
	0 TOTAL PRODUCTION PROBABILITY

NEUTRON ENERGY RANGE 7.3300E 06 TO 7.7000E 06 (EV)

GAMMA RAY ENERGY	PROBABILITY OF PRODUCTION
3.5000E 06	1.0000E-01
	1.0000E-01 TOTAL PRODUCTION PROBABILITY

NEUTRON ENERGY RANGE 7.7000E 06 TO 8.1000E 06 (EV)

GAMMA RAY ENERGY	PROBABILITY OF PRODUCTION
3.5000E 06	4.0000E-01
	4.0000E-01 TOTAL PRODUCTION PROBABILITY

NEUTRON ENERGY RANGE 8.1000E 06 TO 8.5100E 06 (EV)

GAMMA RAY ENERGY	PROBABILITY OF PRODUCTION
3.5000E 06	4.5000E-01
	4.5000E-01 TOTAL PRODUCTION PROBABILITY

NEUTRON ENERGY RANGE 8.5100E 06 TO 8.9500E 06 (EV)

GAMMA RAY ENERGY	PROBABILITY OF PRODUCTION
3.5000E 06	4.4800E-01
	4.4800E-01 TOTAL PRODUCTION PROBABILITY

NEUTRON ENERGY RANGE 8.9500E 06 TO 9.4100E 06 (EV)

GAMMA RAY ENERGY	PROBABILITY OF PRODUCTION
3.5000E 06	4.2800E-01
	4.2800E-01 TOTAL PRODUCTION PROBABILITY

NEUTRON ENERGY RANGE 9.4100E 06 TO 9.8900E 06 (EV)

GAMMA RAY ENERGY	PROBABILITY OF PRODUCTION
3.5000E 06	4.2900E-01
	4.2900E-01 TOTAL PRODUCTION PROBABILITY

NEUTRON ENERGY RANGE 9.8900E 06 TO 1.0400E 07 (EV)

GAMMA RAY ENERGY	PROBABILITY OF PRODUCTION
3.5000E 06	4.4400E-01
	4.4400E-01 TOTAL PRODUCTION PROBABILITY

NEUTRON ENERGY RANGE 1.0400E 07 TO 1.0900E 07 (EV)

GAMMA RAY ENERGY	PROBABILITY OF PRODUCTION
3.5000E 06	4.1600E-01
	4.1600E-01 TOTAL PRODUCTION PROBABILITY

NEUTRON ENERGY RANGE 1.0900E 07 TO 1.1500E 07 (EV)

GAMMA RAY ENERGY	PROBABILITY OF PRODUCTION	
3.5000E 06	3.4400E-01	
	3.4400E-01	TOTAL PRODUCTION PROBABILITY

NEUTRON ENERGY RANGE 1.1500E 07 TO 1.2700E 07 (EV)

GAMMA RAY ENERGY	PROBABILITY OF PRODUCTION	
3.5000E 06	3.3600E-01	
	3.3600E-01	TOTAL PRODUCTION PROBABILITY

NEUTRON ENERGY RANGE 1.2700E 07 TO 1.3300E 07 (EV)

GAMMA RAY ENERGY	PROBABILITY OF PRODUCTION	
3.5000E 06	3.1400E-01	
	3.1400E-01	TOTAL PRODUCTION PROBABILITY

NEUTRON ENERGY RANGE 1.3300E 07 TO 1.4000E 07 (EV)

GAMMA RAY ENERGY	PROBABILITY OF PRODUCTION	
3.5000E 06	3.3700E-01	
	3.3700E-01	TOTAL PRODUCTION PROBABILITY

GAMMA RAYS FROM NEUTRON INELASTIC SCATTERING (OXYGEN)

NEUTRON ENERGY RANGE 1.0000E-10 TO 6.1400E 06 (EV)

GAMMA RAY ENERGY	PROBABILITY OF PRODUCTION	
	0	TOTAL PRODUCTION PROBABILITY

NEUTRON ENERGY RANGE 6.1400E 06 TO 6.9700E 04 (EV)

GAMMA RAY ENERGY	PROBABILITY OF PRODUCTION	
6.1400E 06	1.0000E 00	
	1.0000E 00	TOTAL PRODUCTION PROBABILITY

NEUTRON ENERGY RANGE 6.9700E 04 TO 7.3300E 06 (EV)

GAMMA RAY ENERGY	PROBABILITY OF PRODUCTION	
6.1400E 06	9.8800E-01	
6.9200E 06	9.5000E-03	
7.1200E 06	2.2000E-03	
	9.9970E-01	TOTAL PRODUCTION PROBABILITY

NEUTRON ENERGY RANGE 7.3300E 06 TO 7.7000E 06 (EV)

GAMMA RAY ENERGY	PROBABILITY OF PRODUCTION	
6.1400E 06	9.1100E-01	
6.9200E 06	6.8600E-02	
7.1200E 06	2.0400E-02	
	1.0000E 00	TOTAL PRODUCTION PROBABILITY

NEUTRON ENERGY RANGE 7.7000E 06 TO 8.1000E 06 (EV)

GAMMA RAY ENERGY	PROBABILITY OF PRODUCTION	
6.1400E 06	8.4700E-01	
6.9200E 06	1.0170E-01	
7.1200E 06	3.1300E-02	
	1.0000E 00	TOTAL PRODUCTION PROBABILITY

NEUTRON ENERGY RANGE 8.1000E 06 TO 8.5100E 06 (EV)

GAMMA RAY ENERGY	PROBABILITY OF PRODUCTION
6.1400E 06	8.5670E-01
6.9200E 06	1.1100E-01
7.1200E 06	3.2300E-02
	1.0000E 00 TOTAL PRODUCTION PROBABILITY

NEUTRON ENERGY RANGE 8.5100E 06 TO 8.9500E 06 (EV)

GAMMA RAY ENERGY	PROBABILITY OF PRODUCTION
6.1400E 06	8.5570E-01
6.9200E 06	1.1200E-01
7.1200E 06	3.2500E-02
	1.0002E 00 TOTAL PRODUCTION PROBABILITY

NEUTRON ENERGY RANGE 8.9500E 06 TO 9.4100E 06 (EV)

GAMMA RAY ENERGY	PROBABILITY OF PRODUCTION
2.0000E 06	4.0000E-03
2.7400E 06	1.5000E-02
6.1400E 06	7.7400E-01
6.9200E 06	1.4100E-01
7.1200E 06	4.1000E-02
8.8800E 06	1.0000E-03
	9.7600E-01 TOTAL PRODUCTION PROBABILITY

NEUTRON ENERGY RANGE 9.4100E 06 TO 9.8900E 06 (EV)

GAMMA RAY ENERGY	PROBABILITY OF PRODUCTION
1.0000E 06	3.0000E-03
2.0000E 06	5.0000E-03
2.7400E 06	5.1000E-02
4.4300E 06	1.0000E-02
6.1400E 06	7.0400E-01
6.9200E 06	1.4300E-01
7.1200E 06	4.0000E-02
8.8800E 06	3.0000E-03
	9.5900E-01 TOTAL PRODUCTION PROBABILITY

NEUTRON ENERGY RANGE 9.8900E 06 TO 1.0400E 07 (EV)

GAMMA RAY ENERGY	PROBABILITY OF PRODUCTION
1.0000E 06	1.4000E-02
2.0000E 06	5.0000E-03
2.7400E 06	4.7000E-02
4.4300E 06	2.2000E-02
6.1400E 06	8.7200E-01
6.9200E 06	1.4300E-01
7.1200E 06	7.8000E-02
8.8800E 06	7.0000E-03
	1.0080E 00 TOTAL PRODUCTION PROBABILITY

NEUTRON ENERGY RANGE 1.0400E 07 TO 1.0900E 07 (EV)

GAMMA RAY ENERGY	PROBABILITY OF PRODUCTION
1.0000E 06	3.5000E-02
2.0000E 06	6.0000E-03
2.7400E 06	7.0000E-02
4.4300E 06	3.5000E-02
6.1400E 06	6.4500E-01
6.9200E 06	1.4300E-01
7.1200E 06	9.0000E-02
8.8800E 06	8.0000E-03
	1.0320E 00 TOTAL PRODUCTION PROBABILITY

NEUTRON ENERGY RANGE 1.0900E 07 TO 1.1500E 07 (EV)

GAMMA RAY ENERGY	PROBABILITY OF PRODUCTION
1.0000E 06	6.0000E-03
2.0000E 06	7.0000E-03
2.7400E 06	9.2000E-02
4.4300E 06	4.5000E-02
6.1400E 06	6.1600E-01
6.9200E 06	1.4600E-01
7.1200E 06	1.0600E-01
8.8800E 06	1.0000E-02
	1.0280E 00 TOTAL PRODUCTION PROBABILITY

NEUTRON ENERGY RANGE 1.1500E 07 TO 1.2100E 07 (EV)

GAMMA RAY ENERGY	PROBABILITY OF PRODUCTION
1.0000E 06	8.8000E-02
2.0000E 06	8.0000E-03
2.7400E 06	1.0800E-01
4.4300E 06	5.4000E-02
6.1400E 06	6.1000E-01
6.9200E 06	1.4700E-01
7.1200E 06	1.1900E-01
8.8800E 06	1.2000E-02
	1.1440E 00 TOTAL PRODUCTION PROBABILITY

NEUTRON ENERGY RANGE 1.2100E 07 TO 1.2700E 07 (EV)

GAMMA RAY ENERGY	PROBABILITY OF PRODUCTION
1.0000E 06	9.9000E-02
2.0000E 06	8.0000E-03
2.7400E 06	1.1600E-01
4.4300E 06	5.8000E-02
6.1400E 06	6.0200E-01
6.9200E 06	1.4900E-01
7.1200E 06	1.2100E-01
8.8800E 06	1.3000E-02
	1.1660E 00 TOTAL PRODUCTION PROBABILITY

NEUTRON ENERGY RANGE 1.2700E 07 TO 1.3300E 07 (EV)

GAMMA RAY ENERGY	PROBABILITY OF PRODUCTION
1.0000E 06	1.1300E-01
2.0000E 06	9.0000E-03
2.7400E 06	1.3000E-01
4.4300E 06	6.6000E-02
6.1400E 06	6.0000E-01
6.9200E 06	1.5300E-01
7.1200E 06	1.2800E-01
8.8800E 06	1.4000E-02
	1.2130E 00 TOTAL PRODUCTION PROBABILITY

NEUTRON ENERGY RANGE 1.3300E 07 TO 1.4000E 07 (EV)

GAMMA RAY ENERGY	PROBABILITY OF PRODUCTION
1.0000E 06	1.2400E-01
2.0000E 06	1.0000E-02
2.7400E 06	1.4000E-01
4.4300E 06	7.1000E-02
6.1400E 06	5.9100E-01
6.9200E 06	1.5500E-01
7.1200E 06	1.3300E-01
8.8800E 06	1.5000E-02
	1.2390E 00 TOTAL PRODUCTION PROBABILITY

This page intentionally left blank.

APPENDIX F — DESCRIPTION OF MONTE CARLO PROBLEMS

TABLE VI

DESCRIPTION OF PRIMARY GAMMA RADIATION STUDIES

Source Energy, Mev	Source Altitude, ft	Source-Detector Angle, θ,* degrees	Source-Detector Penetrations, mfp	Number of Histories	Spatial Importance Sampling?	Running Times,† minutes	
						CORSAIR	CORREDIT
0.5	15,000	90	1, 3, 5	3000	No	60	16
		90	7, 9	5700	Yes	83	8
		30	1, 3, 5	6000	No	61	17
		45	1, 2, 3	4350	No	51	13
		45	1, 2, 3	4750	No	52	11
		45	5, 7	12,000	Yes	66	7
		135	1, 2, 3	5000	No	57	14
0.5	50,000	90	$\frac{1}{8}$, $\frac{1}{4}$, $\frac{1}{2}$	3750	No	64	19
		90	1, 2, 3	2500	No	49	14
		90	5, 7, 9	3750	Yes	79	11
		45	1, 3, 5, 7	3500	Yes	87	19
		135	1, 3, 5, 7	3500	Yes	83	12
5.0	15,000	90	1, 2, 3	1700	No	22	9
		90	1, 2, 3	1700	No	21	9
		90	5, 7	4000	Yes	89	6
		90	7, 9	5550	Yes	94	7
		30	3, 5	4050	Yes	70	Data not available
		45	1, 2, 3	7000	No	61	10
		45	5	5000	Yes	90	10
		135	3, 5	5000	Yes		
		135	1, 2	7000	No	51	15

*Measured from θ = 0 for a detector directly above a source.

†Using a CDC-1604-A computer (does not include time charged for hanging and removing magnetic tapes).

TABLE VII

DESCRIPTION OF SECONDARY GAMMA RADIATION STUDIES

Neutron Source Energy, Mev	Neutron Source Altitude, ft	Source-Detector Angle, θ,* degrees	Source-Detector Penetrations,† mfp	Number of Initial Primary Neutron Histories	Spatial Importance Sampling in Secondary Problem?	Running Times,‡ minutes: Primary Neutron CORSAIR	Generation of Secondary Gamma Radiation Source Tape	Secondary Gamma Ray CORSAIR	CORREDIT
14	15,000	90	1/8, 1/4	4800	No	6	5	34	9
		90	1/2, 1 1/2, 3	3000	No			40	11
		90	4, 5, 7, 9	5000	Yes			37	8
		90	1/2, 1 1/2, 3	900§	No	5	3	32	9
		45	1/2, 1, 2, 3	5000	No	7	4	38	12
		45	3, 4, 5	5000	Yes			Data not available	
		45	3 1/2, 4 1/2, 5 1/2	5000	Yes			25	6
		65	1/2, 2, 3 1/2, 4 1/2, 5 1/2	3400	Yes	5	2	49	11
14	50,000	90	1/2, 1 1/2, 3	6600	No	9	4	56	10
10	15,000	90	1/2, 1 1/2, 3	7500	No	9	4	30	8
10	15,000	90	4, 5, 7	5300	Yes			34	4
7	15,000	90	1/2, 1 1/2, 3, 4 1/2, 6	3500	Yes	10	3	39	7
7	15,000	90	1/2, 1 1/2, 3, 4 1/2, 6	7150	Yes			79	14
5	15,000	90	1/2, 1, 2	9000	No	8	3	42	14
5	15,000	90	3, 4, 6	5000	Yes			39	9
5	15,000	45	1/2, 2, 4	7000	Yes	7	2	51	Not run

*Measured from θ = 0 for a detector directly above a primary neutron source.

†Based on 7-Mev photons.

‡Using a CDC-1604-A computer (does not include time charged for changing and removing magnetic tapes).

§With primary neutron importance sampling.